

# Smoldering combustion in mixtures with inert material.

Dissertation  
for the award of the degree

**Doktoringenieur**  
**(Dr.-Ing.)**

by M.Sc. Christoph Wanke

Date of birth: 08.07.1986 in Halle (Saale)

Accepted by the Faculty of Process and Systems Engineering of  
the Otto-von-Guericke-University Magdeburg

Reviewer:

JProf. Dr.-Ing. Alba Diéguez Alonso (Chairman)

Prof. Dr.-Ing. habil. Ulrich Krause (Reviewer)

Prof. Dr. scient Vidar Frette (Reviewer)

Dr.-Ing. Martin Schmidt (Reviewer)

Submitted on: 30.04.2021

Graduation Colloquium on: 29.10.2021

---

## Kurzfassung

In dieser Arbeit wurden zu brennbaren Komponenten Inertstoffe in Größenordnungen von 2,5 % bis 60 % beigemischt. Dabei wurde das Selbstentzündungs- und Schmelbrandverhalten, insbesondere der Effekte der Erhöhung der Reaktionstemperatur von ca.  $600^{\circ}\text{C}$  auf  $1200^{\circ}\text{C}$ , bei ca. 50 % Beimischung untersucht. Diese Effekte wurden maßgeblich mithilfe von isoperibolen und adiabaten Warmlagerungsversuchen und STA Untersuchungen durchgeführt. Zusätzlich wurden FTIR Untersuchungen durchgeführt. Das Ergebnis der experimentellen Untersuchungen ist, dass der Effekt der erhöhten Reaktionstemperaturen darauf zurückzuführen ist, dass die inerten Komponenten ein Stützkonstrukt bilden, welches beim Abbrand das Zusammenrutschen des Schüttgutes verhindert. Damit werden die Poren offengehalten und die Permeabilität vergrößert sich. Dadurch wird der Stoffaustausch vereinfacht. Des Weiteren wird durch die veränderte Strömung der Wärmetransport verändert und Wärmeverluste durch den Boden vermindert. Diese Effekte konnten auch durch Simulationen mit der Software COMSOL Multiphysics nachgewiesen werden.

## Abstract

For the research of the present dissertation inert materials at magnitudes of 2,5 % to 60 % were admixed to combustible components. Within this work, self-ignition and smoldering fire were analyzed. Thereby, it was primarily focused on the effect of increasing the maximum reaction temperature from approximately  $600^{\circ}\text{C}$  to  $1200^{\circ}\text{C}$  degree centigrade admixing approximately 50 % of inert materials. For gaining the requested effects, isoperibolic and adiabatic hot storage experiments, STA investigations as well as FTIR analyzes were conducted. As a result, inert components provide a stabilizing construct which avoids a collapse of the bulk material while burning down. The stabilization causes the previously mentioned increased reaction temperature. Consequently, the pores are kept open which leads to an increasing permeability. This facilitates the exchange of gasses. Furthermore, modified flows cause a change in heat transport and reduce thermal loss through the bottom. These effects were proven by simulations with the help of the software COMSOL Multiphysics.

---

## List of Symbols

### Latin

$c_i$	$[\frac{mol}{m^3}]$	concentration of species i
$c_p$	$[\frac{J}{kg \cdot K}]$	heat capacity
$\dot{j}_i$	$[\frac{kg}{m^2 \cdot s}]$	diffusion flux density of species i
$l$	$[m]$	length
$k_0$	$[\frac{1}{s}]$	pre-exponential factor
$k_{arrh}$	$[\frac{1}{s}]$	reaction rate coefficient according to Arrhenius
$k_D$	$[\frac{1}{s}]$	reaction rate coefficient limited by diffusion
$k$	$[\frac{1}{s}]$	reaction rate coefficient
$p$	$[Pa]$	pressure
$\dot{q}$	$[\frac{W}{m^2}]$	heat flux density
$\dot{q}_V$	$[\frac{W}{m^3}]$	volumetric heat flux density
$r$	$[m]$	radius
$t$	$[s]$	time
$u$	$[\frac{m}{s}]$	velocity / velocity field
$x_k$	$[-]$	mole fraction of species i
$A$	$[m^2]$	area
$C$	$[m^2]$	permeability constant
$D_0$	$[\frac{m^2}{s}]$	diffusion coefficient at 273.15 K
$D_{poros}$	$[\frac{m^2}{s}]$	porosity dependent diffusion coefficient
$D_{temp}$	$[\frac{m^2}{s}]$	temperature dependent diffusion coefficient
$D_i^m$	$[\frac{m^2}{s}]$	diffusion coefficient after Maxwell Stefan of species i
$D_{jk}$	$[\frac{m^2}{s}]$	diffusion coefficient of species j in species k

---

$E$	$[\frac{J}{mol}]$	activation energy
$\Delta H_h; HCV$	$[\frac{J}{kg}]; [\frac{J}{mol}]$	higher calorific value
$\Delta H_i; LCV$	$[\frac{J}{kg}]; [\frac{J}{mol}]$	lower calorific value
$\Delta H_f^\ominus$	$[\frac{J}{mol}]$	heat of formation
$\Delta H_r^\ominus$	$[\frac{J}{mol}]$	heat of reaction
$M_n$	$[\frac{mol}{m^3}]$	mass fraction averaged molar mass
$M_i$	$[\frac{mol}{m^3}]$	molar mass of species i
$Q$	$[\frac{J}{kg}]$	heat of combustion
$Q_{sc}$	$[W]$	heat source
$Q_{br}$	$[\frac{kg}{m^3 \cdot s}]$	mass source in Brinkmann equation
$R$	$[\frac{J}{mol \cdot K}]$	universal gas constant
$R_{species_i}$	$[\frac{kg}{m^3 \cdot s}]$	source term of species i
$T$	$[K]$	temperature
$\dot{V}$	$[\frac{m^3}{s}]$	flow rate
$Z$	$[-]$	temperature dependency factor for diffusion

### Greek

$\alpha$	$[\frac{W}{m^2}]$	heat transfer coefficient
$\epsilon_p$	$[-]$	porosity
$\zeta$	$[-]$	dimensionless length
$\theta$	$[-]$	dimensionless temperature
$\kappa$	$[m^2]$	permeability
$\lambda$	$[\frac{W}{m \cdot K}]$	heat conductivity
$\mu$	$[Pa \cdot s]$	dynamic viscosity
$\tau$	$[-]$	tortuosity factor
$\xi$	$[-]$	geometry factor
$\rho$	$[\frac{kg}{m^3}]$	density
$\sigma$	$[-]$	Frank-Kamenetzki Parameter
$\phi$	$[-]$	porosity
$\omega_i$	$[-]$	mass fraction of species i

---

### Sub- and Superscript

<i>a</i>	—	ambient
<i>A</i>	—	apparent
<i>bulk</i>	—	bulk material
<i>c</i>	—	critical
<i>eff</i>		effective
<i>fl, fluid</i>	—	fluid
<i>p</i>	—	particle
<i>solid</i>	—	solid, solid particle
<i>SI</i>		Self-ignition
<i>tt</i>		thermally treated

### Misc.

$\nabla$	[—]	Nabla operator
<i>Bi</i>	[—]	Biot number
<i>LC – L</i>	[—]	Lignite coal - Lausitz
<i>LC – P</i>	[—]	Lignite coal - Profen
<i>LC – P<sub>tt</sub></i>	[—]	Lignite coal - Profen thermally treated
<i>raw</i>	[—]	raw material
<i>waf</i>	[—]	water and ash free

# Contents

<b>1. Introduction and theoretical approach</b>	<b>1</b>
1.1. Background and motivation . . . . .	1
1.2. Objectives and strategy . . . . .	4
<b>2. Theory and experimental procedure</b>	<b>6</b>
2.1. Theory of self-ignition, spontaneous combustion and smoldering combustion . . . . .	6
2.2. Theory of thermal explosion . . . . .	9
2.3. Experimental procedure . . . . .	10
2.3.1. Isoperibolic hot storage . . . . .	10
2.3.2. Adiabatic hot storage . . . . .	13
<b>3. Materials and material properties</b>	<b>18</b>
3.1. Materials . . . . .	18
3.2. Material properties . . . . .	20
3.2.1. Particle size, shape and particle surface . . . . .	20
3.2.2. Porosity and particle density . . . . .	21
3.2.3. Permeability . . . . .	23
3.2.4. Heat conductivity . . . . .	25
3.2.5. Proximate analysis . . . . .	26
3.2.6. Elemental analysis . . . . .	27
3.2.7. Calorific value . . . . .	28
3.2.8. Heat capacity . . . . .	28
<b>4. Experimental setup</b>	<b>30</b>
4.1. Hot storage experiments . . . . .	31
4.2. Forced convection experiments . . . . .	35
4.3. Simultaneous thermal analysis, with coupled FTIR . . . . .	35
4.4. Fourier-transformed infrared spectroscopy-FTIR . . . . .	38

<b>5. Experimental results</b>	<b>41</b>
5.1. Isoperibolic hot storage . . . . .	41
5.1.1. Formal kinetic data . . . . .	41
5.1.2. Maximum temperatures . . . . .	43
5.2. Adiabatic hot storage . . . . .	50
5.3. Hot storage and FTIR . . . . .	52
5.4. Pipe experiments . . . . .	53
5.5. Simultaneous-thermal analysis (STA) . . . . .	55
5.6. Summary and discussion of calculated formal kinetic data . . . . .	59
<b>6. Simulation</b>	<b>61</b>
6.1. Finite Element Method (FEM) . . . . .	61
6.2. The developed COMSOL Model . . . . .	62
6.2.1. Objectives and strategy of the numerical investigation . . . . .	62
6.2.2. Previous work and developed model . . . . .	64
6.2.3. Mathematical description . . . . .	67
6.2.4. Geometry and Mesh . . . . .	70
6.3. Definitions and initial values . . . . .	75
6.3.1. Boundary conditions and initial values . . . . .	75
6.3.2. Material definitions . . . . .	76
6.4. Combustion modeling . . . . .	78
6.4.1. Reaction rate . . . . .	78
6.5. Combustion reactions and heat of combustion . . . . .	81
6.6. Used COMSOL solver . . . . .	83
6.7. Results . . . . .	84
<b>7. Calculation of uncertainties in isoperibolic hot storage experiments</b>	<b>97</b>
<b>8. Summary and Outlook</b>	<b>103</b>
<b>Bibliography</b>	<b>106</b>
<b>A. Appendix</b>	<b>i</b>
<b>B. Matlab Code for linear fitting</b>	<b>xiii</b>
<b>C. Matlab Code for Monte Carlo Simulation</b>	<b>xx</b>

## List of Figures

1.1.	Sample temperature (center) for different mixtures of diatomaceous earth with cellulose; sample volume 400 ml, storage temperature $272^{\circ}\text{C}$ . . . . .	3
1.2.	Influence of inert material on the $T_{ST}$ ; mixtures of diatomaceous earth with cellulose . . . . .	3
2.1.	Comparison of the models from Semenov, Thomas and Frank-Kamenetzki . . . . .	9
2.2.	Sample-temperature profiles at different oven temperatures . . .	12
2.3.	Temperature dependent induction time for different $V/A$ ratios, translated, redrawn . . . . .	13
2.4.	Adiabatic experiment, measured temperatures (left) and calculated signal (right) according to equation 2.7 . . . . .	15
3.1.	Particle size distribution and surface values (given in the key) .	21
3.2.	Typical values of Hydraulic Conductivity and Permability . . .	23
3.3.	Experimental setup used to measure permeability; FC: flow controller, PI; pressure indicator . . . . .	25
3.4.	Two-plate apparatus for measurement of heat conductivity . . .	25
3.5.	Heat capacity of LC-P and silica lignite mixtures calculated from a heating process using the Gröber solution . . . . .	29
4.1.	Design of oven types 1 - 6 . . . . .	33
4.2.	Experimental Setup SYSTAG TSC 511 SEDEX with FTIR sampling unit . . . . .	34
4.3.	Experimental setup; pipe experiments . . . . .	35
4.4.	Experimental setup of the used STA (LABSYS evo.) . . . . .	37
4.5.	Schematic view of a Michelson interferometer in an FTIR, an simple version of the Temet-carrousel . . . . .	39
4.6.	Experimental setup of the FTIR and sampling unit attached to the SEDEX oven . . . . .	40



5.1.	Arrhenius diagram for Lignite and Lignite Silica Mixtures . . . .	43
5.2.	Comparison of the maximum combustion temperatures of Lignite (LC-L) Silica Mixtures and LC-P Magnesium oxide Mixtures	44
5.3.	Basket temperature as function of time, with self-heating and self-ignition for mixtures of lignite coal and MO150 in a 100 $cm^3$ sample basket; $T_{oven} = 150^\circ C$ . . . . .	45
5.4.	Temperature and mass curves of 100 % lignite and 50 % admixed MO 150; mass is normalized to the mass of lignite . . . . .	46
5.5.	Maximum temperatures resulting from the self-ignition and combustion of lignite and mixtures containing lignite with 50 wt% of inert additives. Box: 25 % and 75 % quantile with median, whiskers: max. / min. values . . . . .	47
5.6.	Schematic view of the ash height of an finished hot storage experiment. $V_{basket} = 100cm^3$ . (Particle sizes not to scale) . . . . .	47
5.7.	Time-temperature curves of an isoperibolic hot-storage experiment with multiple thermocouples located at $\frac{r}{2}$ in the xy-plane and at $\frac{1}{4}$ , $\frac{1}{2}$ and $\frac{3}{4}$ height along the central z-axis (see insert bottom right); $V = 1600 cm^3$ at $T_{oven} = 130^\circ C$ . The lower parts show magnifications of the shaded areas in the plots of the upper line. . . . .	48
5.8.	Arrheniusplot of adiabatic hot storage experiments of different lignite-inert mixtures; fitted lines are shown bold. $T_{onset} = 103^\circ C$ , $V_{basket} = 100 cm^3$ . . . . .	51
5.9.	Adiabatic temperature-time curve of thermally treated LC-P <sub>tt</sub> , onset temperature $190^\circ C$ . . . . .	52
5.10.	Averaged temperature and concentration profiles of 5 isoperibolic hot-storage experiments for each substance in the Sedex oven coupled with FTIR, $T_{oven} = 150^\circ C$ , $V_{sample} = 100 cm^3$ , dashed line shows local minimum in $CO/CO_2$ ratio at 4.9 h . . . . .	54
5.11.	Propagation of reaction front in the pipe experiments for pure lignite (top) and lignite with 50 wt% S63 (bottom), at an oven temperature of $150^\circ C$ . . . . .	56
5.12.	FTIR coupled STA measurements of Lignite (LC-P) with different heating rates as given in the legend in $K/min$ . The sample mass was from 19.88 mg to 21.35 mg. . . . .	58

6.1. Cross-sectional view of a riverbank and the governing equations applied to each flow regime. . . . .	66
6.2. Geometry used for simulation with the generated and mesh quality	72
6.3. Examples of good cell arrangement and poor examples for skewness and growth rate . . . . .	73
6.4. Temperature and oxygen concentration for the used mesh (coarse) and a mesh twice as fine. . . . .	74
6.5. Calculated permeability-porosity relationship according to equation 6.8 . . . . .	77
6.6. Temperatures in the sample center for different diffusion-limiting factors $k_D$ without permeability adaption . . . . .	80
6.7. Evolution of temperature in experiments (see figure 5.3) compared to simulated temperature evolution. . . . .	85
6.8. Temperature profiles for no (left column), 50 % (center column) and 100 % (right column) permeability adaption according to equation 6.8 with no reaction adjustment. Attention: different color codes (see bar at the left). Rows: Temperature profiles at different time steps, Figures of more time steps are given in Appendix A.3 . . . . .	88
6.9. Temperature profiles for different permeability adaptations at $0.5 \cdot h_{sample}$ in central axis . . . . .	89
6.10. Flux of oxygen for the three permeability-adaption cases at $0.25 \cdot h_{sample}$ (first diagram) and $0.5 \cdot h_{sample}$ (second and third diagram) along central axis. The diagrams are made to correspond at 280 min, 310 min and 210 min, the times of $T_{max}$ . . . . .	91
6.11. Sum of convective and conductive heat flux through bottom over time for different permeability cases. Reaction front passed at 280 min (no adaption), 310 min (50% adaption) and 210 min (100% adaption) (dashed lines). . . . .	93
6.12. Heat flux in x and y direction (upwards positive) at heights $0.25 \cdot h_{sample}$ (first diagram) and $0.5 \cdot h_{sample}$ (second and third diagram) along the central axis. The dashes lines indicate the times when the reaction front passes the sampling point. . . . .	95
6.13. Simulated concentration of combustion products at outlet. . . . .	96

7.1. Probability-density function from the MC-Simulation of apparent activation energy $E$ [ $J/mol$ ], with fitted normal distribution ( $\mu = 109.94 J/mol$ ; $\sigma = 3.31 J/mol$ ) . . . . .	100
7.2. Probability-density function of y intercept [ $K^2/m^2$ ], with fitted normal distribution ( $\mu = 53.30 K^2/m^2$ $\sigma = 1.07 K^2/m^2$ ). . . . .	101
7.3. Probability-density function of pre-exponential [ $1/s$ ] factor for case 1 to 3, with fitted exponential distributions ( $\mu = 1.64 \cdot 10^9$ ; $1.67 \cdot 10^9$ ; $1.74 \cdot 10^9 1/s$ with a standard deviation that is equal). . . . .	101
7.4. Probability-density function of pre-exponential factor [ $1/s$ ] for case 4 . . . . .	102
A.1. SEM pictures of used substances . . . . .	vi
A.2. Correction of $CO_2$ concentrations in the FTIR measurements in the Sedex oven, exemplary shown for one curve. . . . .	vii
A.3. Temperature profiles for no (left column), 50 % (center column) and 100 % (right column) permeability adaption according to equation 6.8 with no reaction adjustment. Attention: different color codes (see bar at the left) Pictures per row at different time steps. Link back to page 85. . . . .	viii
A.4. Oxygen profiles for no (left column), 50 % (center column) and 100 % (right column) permeability adaption according to equation 6.8 with no reaction adjustment. Attention: different color codes (see bar at the left) Pictures per row at different time steps. . . . .	ix
A.5. Carbon dioxide profiles for no (left column), 50 % (center column) and 100 % (right column) permeability adaption according to equation 6.8 with no reaction adjustment. Attention: different color codes (see bar at the left) Pictures per row at different time steps. . . . .	x
A.6. Flux of all species and summed overall flux at $0.25 \cdot h_{sample}$ (first diagram) and $0.5 \cdot h_{sample}$ (second and third diagram) at central axis. Reaction front passed at 280 min, 310 min and 210 min (dashed lines). . . . .	xi
A.7. Comparison of $k_{arr}$ for $E_A$ and $k_0$ determined for LC-P from different experiments . . . . .	xii
A.8. Arrhenius diagram of Lignite and Lignite Magnesium Oxide Mixtures . . . . .	xii

## List of Tables

2.1. Values for $\sigma_c$ , valid for $Bi \rightarrow \infty$ . . . . .	10
3.1. Porosities and bulk densities of used materials . . . . .	22
3.2. Measured permeabilities of LC-P and silica at different flow rates [ $m^2$ ] . . . . .	24
3.3. Measured heat conductivities at given porosities . . . . .	26
3.4. Proximate analysis [wt%] for LC-L, LC-P and $LC - P_{tt}$ ; Values with index $d$ are based on dry substance . . . . .	27
3.5. Elemental analysis of the used coals [wt%] for raw material and a water and ash free (waf) substance . . . . .	28
3.6. Calorific values of LC-P and $LC - P_{tt}$ . . . . .	28
4.1. Overview over the laboratory ovens . . . . .	31
5.1. Self-ignition temperatures in $^{\circ}C$ and activation energies in $kJ/mol$ for Lignite and Lignite Silica mixtures . . . . .	42
5.2. Pre-exponential factor $k_0$ and apparent activation energy $E_a$ obtained from DSC experiments using the TG signal. . . . .	57
6.1. Composition of apparent fuel molecule $n_{ap}$ for $LC - P$ (fuel) and $LC - P_{tt}$ (char) based on the water and ash free results of the proximate analysis (see table 3.4) . . . . .	82
A.1. Ratio of main combustion products from FTIR experiments (see fig. 5.10). Area below curve calculated by numerical integration, normalized to smallest amount. . . . .	v
A.2. Heat of formation of the complete reaction products, heat of reaction (LCV) and heat of formation for fuel and char . . . . .	v
A.3. Heat of formation of the reaction products and heat of reaction for more and less oxidated incomplete fuel reaction . . . . .	vii
A.4. Heat of formation of the reaction products and heat of reaction for more and less oxidated incomplete char reaction . . . . .	vii

A.5. Increase of the self-ignition temperature due to inert admixtures  
for different sample sizes . . . . . **xii**

# **1. Introduction and theoretical approach**

## **1.1. Background and motivation**

Smoldering fires, caused by self-ignition, represent a potential danger for people and the environment. They cause considerable damage in industry. Due to the quite long induction period, smoldering combustion goes unnoticed for a long time until the fire reaches the upper layers and turns into glowing or open flame. Until then, smoldering combustion can be detected by the flue gasses only. Compared with flaming combustion the reaction temperature in a smoldering reaction front is lower due to the lower reaction rate. The consequences of smoldering combustion are manifold. On the one hand are gas emissions consisting of toxic but also greenhouse gasses, on the other a lot of dust particles are produced. These substances represent a considerable burden for man and environment.

The self-ignition of combustible dusts is a main source of fires wherever dusts are stored in large amounts over extended time periods. Since these fires are hard to detect and hard to fight, property and environmental damages are quite high [1]. Problems occur mainly in wood [2] and recycling industry [3] but also in coal seams [4] and peat layers [5]. Lohrer [6] summarized publications about self-ignition and smoldering combustion in coal seams. Inbetween 0.3 and 14 million tons of coal are lost due to combustion per year, with additional 100-200 million of tons that get unusable for mining.

Persson [7] gives an overview and practical guide on fire fighting in silos. It can be summarized that fighting a smoldering combustion in a silo is time and material consuming. Inertisation over a long period of time is often the only possibility. Hundreds of tons of inert gas must be supplied to the silo over several days until the smoldering combustion can be stopped. Additionally there is a high risk for dust and gas explosion due to the incomplete character of the combustion.

For all these reasons, that vary from human health, environmental damage, industrial losses and firefighting effort, it can be concluded that self-ignition is still an issue that needs to be better understood and researched.

In 2010 BAM Research Project 291 (Beurteilung und Verhinderung von Selbstentzündung und Brandgasemission bei der Lagerung von Massenschüttgütern und Deponiestoffen, translated: Assessment and prevention of self-ignition and combustion gas emissions during the storage of bulk and landfill materials) [3] was carried out. The result of the project was a scientific method of hazard assessment for self-ignition processes during the storage of bulk materials, landfill materials and recycled materials. The smoldering behavior of recycled materials especially from construction industry was investigated. Since these materials contain both combustible and inert material, a model substance consisting of diatomaceous earth, or kieselguhr, and cellulose was investigated. Isoperibolic tests showed an interesting effect. Inert material, that is usually supposed to be non-reactive and, therefore, safe, increased the maximum reaction temperature up to several hundred Kelvin. The results of the project, regarding this topic, can be summarized as follows:

- inert material increases the self-ignition-temperature (see figure 1.2)
- admixtures of inert material increases the maximum reaction temperature especially for 40/60 and 60/40 mixtures (see figure 1.1)
- reaction is possible down to 2.5% combustible material (see figures 1.1 and 1.2 )

Within Research Project 291 the reason for the higher reaction temperatures, in particular for mixtures with nearly equal amounts of combustible and inert components, could not be determined. The present work aim at closing this gap through a extensive series of experiments and associated numerical simulations.

This work focuses on influence of significant amounts of inert material (within the range of 2.5 wt.% to 60 wt.%) on the self-ignition as well on reaction behavior of combustible material. Contamination and impurities are not considered. For these conditions, only few research reports have been published. In a literature review three fields of interest could be identified:

- recycled material especially from construction industry

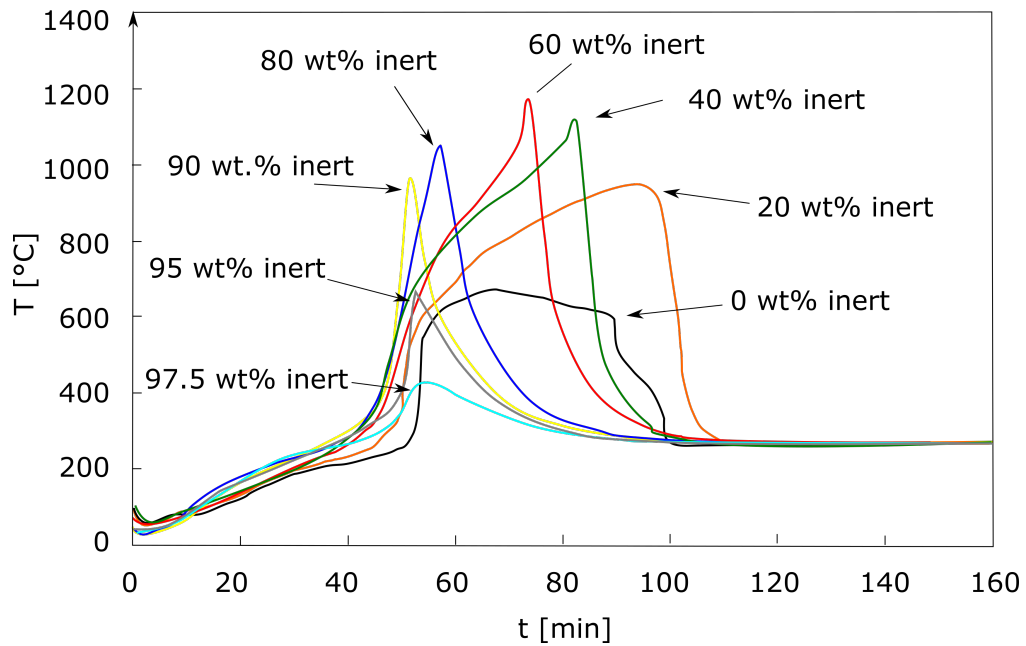


Figure 1.1.: Sample temperature (center) for different mixtures of diatomaceous earth with cellulose; sample volume 400 ml, storage temperature 272 °C [3] (redrawn, translated)

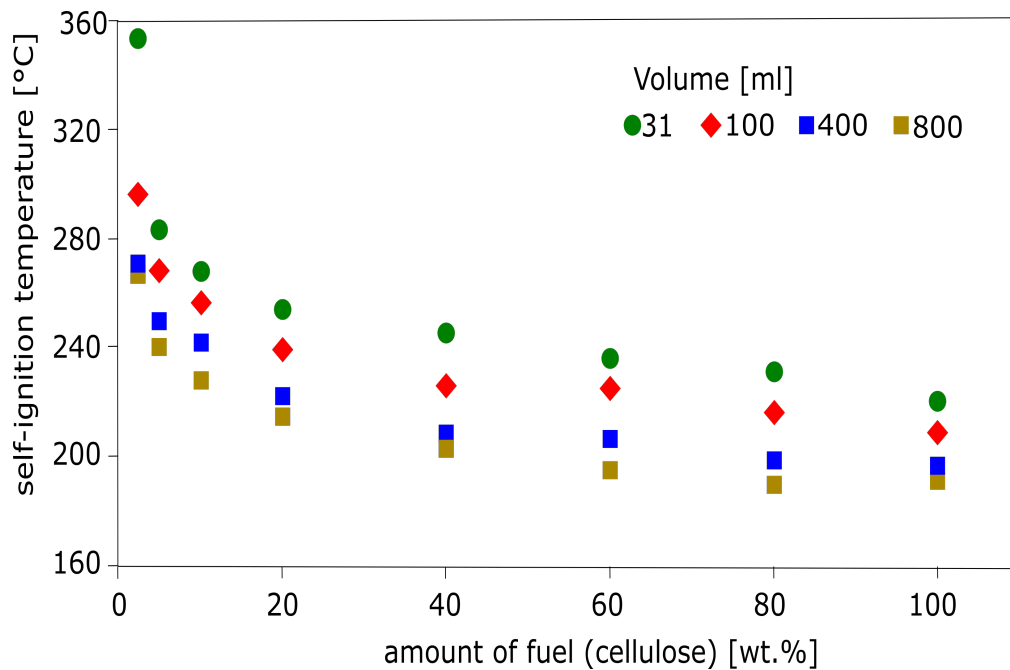


Figure 1.2.: Influence of inert material on the  $T_{SI}$ ; mixtures of diatomaceous earth with cellulose [3] (redrawn, translated)



- carbon-rich soil
- high-grade contaminated soil

Babrauskas [8] gives a short overview over the influence of antioxidants, contaminants and multiple-component-substances. It is assumed that contaminants are substances that increase combustibility like fatty acids or vegetable oils. Multiple component systems are defined as substances where both materials are combustible, but no inert-combustible mixtures have been treated.

The only study beside BAM Report 291, dealing with significant amounts of inert materials in the field of self-ignition and smoldering combustion is carried out by Restuccia [5]. This work is about self-ignition and smoldering in soil, especially peat layers. Beside the influence of moisture, the amount of inert material on the self-ignition temperature was reported. Inert material increases the self-ignition temperature but the activation energy remains unchanged. Maximum reaction temperatures were not considered within Restuccias work.

## 1.2. Objectives and strategy

Within this work the phenomenon of higher reaction temperatures should be solved. This is done through more detailed experimental studies combined with a numerical investigation. Furthermore, experiments were designed and conducted to determine material properties necessary for the numerical investigation.

Different substances were studied using adiabatic and isoperibolic hot storage. In addition, simultaneous-thermal analysis (STA) experiments were conducted, both coupled with Fourier transformed infrared spectroscopy (FTIR).

Higher temperatures can be ascribed to two general phenomena. A higher heat release on one hand, and on the other hand lower heat losses to surroundings.

A higher heat production can be caused by a higher reaction rate. Due to the temperature dependency of the Arrhenius law a positive feedback loop could be triggered that leads to a higher reaction rate and, therefore, a higher mass-loss rate. If a second-order reaction is assumed, the increase in oxygen concentration (due to higher inflow) may enhance the reaction rate and the

heat production. The higher oxygen concentration would also shift the reaction to a more complete combustion leading also to higher temperatures.

According to Trimms [9], who investigated gas reactions in porous media, the larger inner surfaces of porous media result in an increase in the reaction zone and an quasi-equilibrium heat transport between the gas phase and the solid material. This results in higher combustion velocities and, therefore, temperatures.

Lower heat losses can increase the maximum temperature as well. Heat conductivity is dominated by the amount of air within the bulk material.

The particle's heat conductivity can be neglected, thus, the amount of air influences it instead of the particle material. Due to the admixture or to the shrinking of the combustible parts of bulk material, the porosity may be changed during the combustion process. In general, an increase in porosity implies an increase in permeability and, therefore, an increased mass transfer. This leads to an increased oxygen supply and, as a consequence, to a higher reaction rate as well as to increased heat losses due to intensified outflow of hot gasses.

To investigate this problem, the behavior of different inert-combustible mixtures was studied using different experimental setups. Different inert materials might behave differently due to variations in particle-size distributions and specific surfaces. Using different experimental setups, different thermal boundary conditions could be established. Furthermore, experiments where it was possible to vary the type of convection (natural or forced) were carried out.

Numerical simulations supplement experimental investigations since they allow assumptions on internal processes to be tested. Temperature development and species concentration that cannot be measured easily, can be calculated. Moreover, one parameter like permeability can be changed with all other parameters are kept unchanged in order to investigate their influence on the behavior of the system, only. This is hardly possible in experiments. After the experiments were performed, the main reason for the higher reaction temperatures could be ascribed to porosity and permeability effects. Since the inert mixtures do not shrink, pores are kept open and permeability is therefore increased. Consequently, the main scope of the simulation is the adaption of the permeability.

## 2. Theory and experimental procedure

### 2.1. Theory of self-ignition, spontaneous combustion and smoldering combustion

This chapter gives an overview of self-ignition and the subsequent propagation of the reaction front. It includes the presentation of the theory used to evaluate the experiments. The theory that describes the numerical investigation is presented in chapter 6.

Porous media always contain a fluid in the voids. In the present study, only porous media containing gasses are considered. While, at the beginning, the voids are filled with ambient concentration. Due to the large surface area, significant exothermic reactions with oxygen start even at ambient temperatures, thus, heat is produced in the entire bed. If the heat production within the bed is smaller than the heat losses, the system stabilizes at a certain equilibrium temperature. If the heat production is larger, the temperature increases. Hence, heat accumulates, which increases the speed of the exothermic reaction. A positive feedback loop is triggered that results in an exponential temperature rise with subsequent self-ignition. If the reaction front reaches the surface of the porous medium, flaming is possible. [10] [11]

Within his Ignition Handbook, Babrauskas summarized the route from self-heating to spontaneous combustion as followed:

**Self-heating** an increase in temperature due to exothermicity of internal reactions

**Thermal Runaway** self-heating that rapidly accelerates to high temperatures

**Spontaneous combustion** visible smoldering or flaming caused by thermal runaway.

Thus, the process is called 'self-heating'. A critical intermediate outcome of 'thermal runaway' may or may not occur, while the final outcome (if thermal runaway does occur) may be 'spontaneous combustion'. There is no single, universally accepted definition of 'spontaneous combustion' but the definition above can be considered as the most reasonable one [8].

The main parameter characterizing the self-ignitability of a system is the self-ignition temperature  $T_{SI}$  [10]. This parameter is influenced by a large number of factors given below that are well described by Babrauskas [8], Krause [12], Lohrer [6], Drysdale [13], and Rein [14], as well as the European Standard DIN EN 15188 [15]. This work is based on DIN EN 15188 from 2007, there was a revision in 2019, but at this point the experiments within this work were already done.

- Influence of Material Properties
  - specific heat capacity
  - particle size distribution
  - heat conductivity
  - bulk density
- Influence of reaction kinetics
  - activation energy
  - pre-exponential factor
- Influence of Boundary Conditions
  - ambient temperature
  - oxygen volume fraction
  - air movement along the surface of the bulk material
  - humidity / rain / snow
- Influence of Geometry
  - volume to surface ratio
  - slope of the pile

Self-heating and, therefore, the thermal runaway starts in the center of the bulk material if the ambient temperature  $T_a$  is close to the critical temperature  $T_c$ . Therefore the reaction front has to move, which Ohlemiller called smoldering combustion. Smoldering combustion is defined by him as a self-sustaining, propagating exothermic reaction wave deriving its principal heat from heterogeneous oxidation of the fuel (direct attack of oxygen on the fuel surface) [16].

There are two one-dimensional ways to model smoldering combustion under the assumption that the flow is homogeneous and there is an adiabatic wall parallel to the flow direction. The models of forward and reverse smoldering are shown in figure ??.

**Forward Smoldering** The air flows through the charred region directly into the oxidation zone. The released heat is transported mainly by convection downstream, into the pyrolysis, drying and preheating zone. These zones are rendered inert due to the reaction products. Since the flue gas cools down in the downstream zone, condensation, mostly of water, takes place when the dew point is reached. Depending on the material, this can lead to swelling particles that clog. The heat transport into the unburned material is better than for reversed smoldering, so the reaction is faster and more complete.

**Reverse Smoldering** The air flows through the virgin fuel as well as through the preheating, drying and pyrolysis zone into the oxidation zone. The flue gas flows through char and ash. The heat from the combustion reaction is to a large extent hindered by airflow from reaching the preheating, drying and pyrolysis zone. Since less energy is supplied to the preheating zone, the reaction is less complete and much slower.

Usually, even under natural convection, there is a flow due to buoyancy. Reverse and forward smoldering occur in parallel if the point of ignition is near the center of the porous medium. Upstream (above) of the point of ignition forward smolder occurs while downstream (below) reverse smoldering takes place. This results in a pear-shaped temperature profile.

## 2.2. Theory of thermal explosion

Within this section, the theory of thermal explosion used for evaluating isoperibolic hot storage tests is described.

The three most frequently used theories of self-ignition were developed by Semenov [17] [18], Frank Kamenetzki [19] [20] and Thomas [21] [22]. All of them are based on the Fourier heat transfer equation for a closed, one phase, homogenous and non-adiabatic system (Eq. 2.1). The difference between the models is the different assumption for the Biot number (Eq. 2.2).

$$\rho c_p \left( \frac{\partial T}{\partial t} + \vec{u} \times \text{grad}T \right) = \text{div}(\lambda \cdot \text{grad}T) + \dot{q} \quad (2.1)$$

$$Bi = \frac{\alpha}{\lambda} \cdot l_{ch} \quad (2.2)$$

The model of Semenov is valid for well-mixed materials (gasses, fluids) but not for solids. Frank-Kamenetzki transferred this model to bulk materials. The temperature at the boundary is uniform and invariant. The heat transfer through the wall is assumed as ideal and is, therefore, unrestricted. Thomas enhanced the model of Frank-Kamenetzki for small samples where the sample surface temperature differs from the ambient temperature [23].

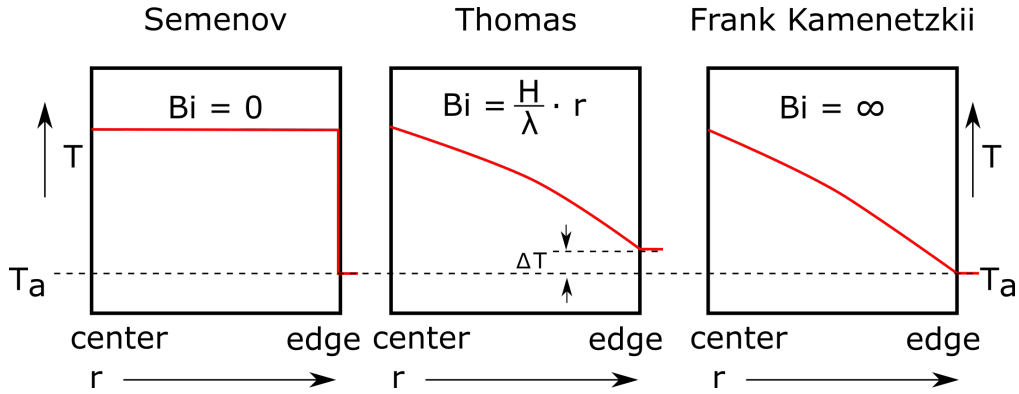


Figure 2.1.: Comparison of the models from Semenov, Thomas and Frank-Kamenetzki [23]

The model of Frank-Kamenetzki has been discussed and successfully compared with experimental data earlier [24] [8] [23]. Therefore, a detailed derivation

and discussion will not be given here. Frank-Kamenetzki defines the Frank-Kamenetzki parameter  $\sigma$  as shown in equation 2.3. He solved equation 2.3 for simple geometries and found that the solution depends on a critical value  $\sigma_c$  (table 2.1) only. At this value, the equilibrium condition is fulfilled and higher ambient temperatures will lead to an ignition of the sample. Equation 2.4 shows the remodeled form of Eq. 2.3, where the linear character of the equation is obvious. Plotting  $\ln(\sigma_c \cdot \frac{T_{SI}^2}{r^2})$  vs.  $\frac{1}{T_{SI}}$  (Arrhenius diagram) the slope of the emerging line equals  $-\frac{E}{R}$ . The pre-exponential factor can be calculated from the y-intercept [24] [8] [23].

Table 2.1.: Values for  $\sigma_c$ , valid for  $Bi \rightarrow \infty$ , adapted from [23]

Geometry	$\sigma_c$
sphere	3.32
cylinder $d=h$	2.84
cylinder $h \rightarrow \infty$	2.00
cube	2.52
layer $d \rightarrow \infty$	0.88

$$\delta = \frac{E \cdot r^2 \cdot \rho \cdot Q \cdot k_0}{\lambda \cdot R \cdot T_a^2} \cdot \exp\left(1 - \frac{E}{R \cdot T_a}\right) \quad (2.3)$$

$$\ln\left(\sigma_c \cdot \frac{T_{SI}^2}{r^2}\right) = -\frac{E_A}{R} \cdot \frac{1}{T_{SI}} + \ln\left(\frac{E_A \cdot Q \cdot \rho \cdot k_0}{R \cdot \lambda}\right) \quad (2.4)$$

$$y = m \cdot x + n$$

## 2.3. Experimental procedure

### 2.3.1. Isoperibolic hot storage

A practical guide on how to perform and evaluate hot storage experiments is given in the European Standard DIN EN 15188 [15]. The conducted experiments as well as the test evaluation are based on this standard. The following paragraphs describe the approach (previously published by the author in [25], [26]).

The samples have to be placed in a preheated oven with a constant temperature. If the sample ignites, the oven temperature is reduced, if not it is raised. This procedure will be repeated, always with new sample material, until both an ignition and a non-ignition case can be observed within an oven temperature range of 2 K. The temperature of the non-ignition case with the highest temperature is called the self-ignition temperature  $T_{SI}$ , which is determined for at least three or better four different basket sizes. To extrapolate the laboratory-scale experiments to technical scale and to calculate the activation energy, the theory of thermal explosion by Frank Kamenetzki is used.

There are three cases to distinguish (see figure 2.2). In case A the oven temperature is not high enough to lead to self-heating since the sample temperature did not increase above  $\vartheta_A$ . At a higher oven temperature  $\vartheta_B$ , self-heating took place since the sample temperature was above  $\vartheta_B$ . However, since the sample temperature only was marginally higher than  $\vartheta_B$ , one has to conclude that no combustion occurred. If the sample-temperature is more than 60 K larger than the oven temperature, is considered as a case with an ignition, according to DIN EN 15188 [15]. In case C an ignition takes place, as reflected in a sample temperature significantly higher than the oven temperature.

The induction time is described in DIN EN 15188 [15]. In the version of 2007, it is the time from the sample reaches oven temperature until the maximum temperature rise  $dT/dt$ , above the oven temperature. The figure within the standard (see figure 2.2) describes it as the time from putting the sample into the preheated oven until the maximum temperature rise. With the revision of the DIN EN 15188 in 2019 the figure was changed and the induction time is now clearly defined as the time from sample is heated up to oven temperature to the maximum temperature rise. Using this definition, factors like humidity, the initial temperature of the sample and the cooling of the oven during the placement of the sample are excluded. Therefore, this method would be better. Within this work, the induction time was calculated according to figure 2.2. Since the determination of induction times are not a central part of this work, the difference is not important. The criterion of the maximal temperature rise was used to determine the maximal reaction rate. As an improvement, the induction time can be calculated for every individual combustion process instead of using a fixed value (e.g. time to reach 400 °C).



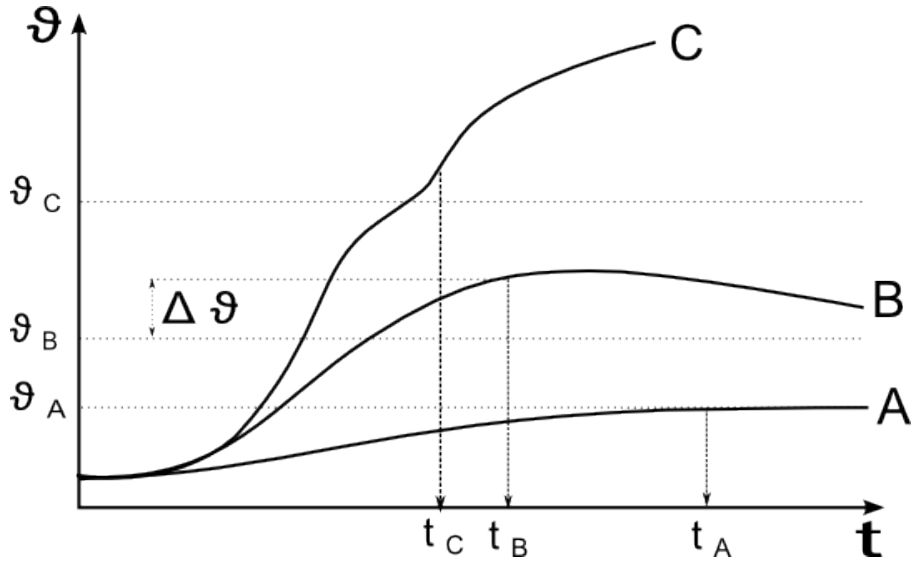


Figure 2.2.: Sample-temperature profiles at different oven temperatures [15]

Hensel, Löffler and Krause [10] calculated the temperature field in dependency on time, while the models discussed above are independent of time. Figure 2.3 shows the induction time as a function of ambient temperature and in dependency on different volume-to-surface ratios  $V/A$ . The volume-to-surface ratio is a measure for the size of the sample, given an equidistant cylinder  $V/A = d/6$ . The induction time decreases with increasing temperature and tends asymptotically towards zero. At lower ambient temperature, the induction time increases and tends towards infinity. The temperature where the induction time becomes infinite is called the self-ignition temperature  $T_{SI}$ . It is the temperature at which heat production and heat loss are equal. Higher temperatures will lead to runaway reactions. Within the diagram, three different regions can be identified that are shown using  $V/A = 6.67cm$  as an example. To the left of the self-ignition temperature  $T_{SI}$ , marked with a dashed line, the bulk material can be stored safely, since heat production is smaller than heat loss. In the upper right part the bulk material will ignite, since the temperature is high enough and the bulk material is stored for a period longer than the induction time. In the area below the curve, the resident time above the self-ignition temperature is not long enough to get an ignition. This behavior can be observed for waste piles. The self-ignition temperature might be exceeded for some days during summer, but with duration shorter than the induction time. The waste pile will not ignite, even though this condition cannot be treated as safe in general.

A similar behavior as displayed in Figure 2.3, where self-ignition depends on the volume-to-surface ratio in combination with a critical temperature. It applies for many situations. If a certain volume, with a corresponding  $V/A$  ratio, is stored below the critical temperature, it will not ignite. If it is stored above its critical temperature, it will ignite if the induction time is exceeded. This critical temperature is called  $T_{SI}$ . At this temperature, heat release by reaction and heat loss at the boundaries are equal.

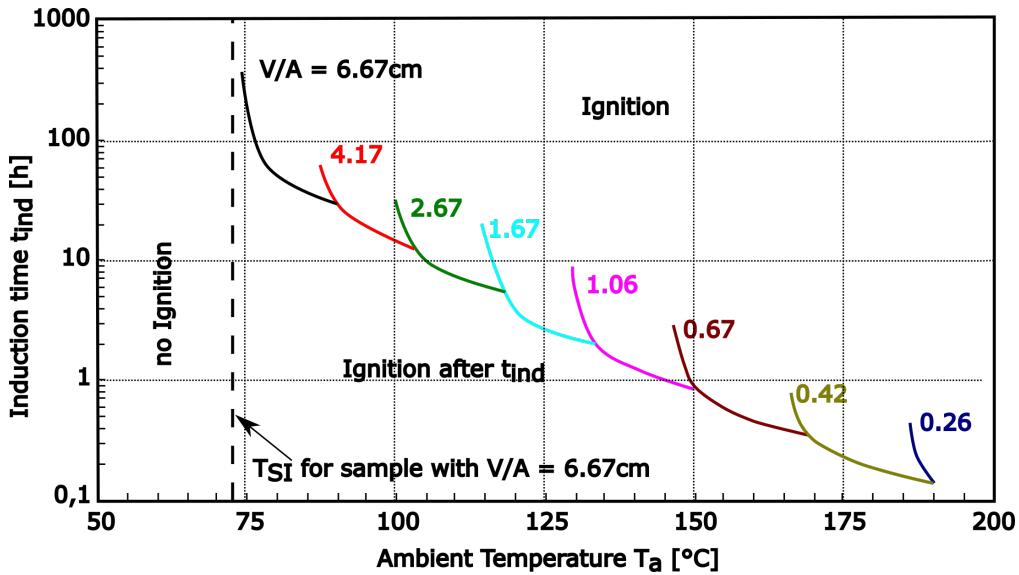


Figure 2.3.: Temperature dependent induction time for different  $V/A$  ratios, [10], translated, redrawn

### 2.3.2. Adiabatic hot storage

The theory of adiabatic hot storage below is mainly based on the work of Hensel et al. [10] and Schossig et al. [27].

Adiabatic tests have not been part of a standard or norm when the main part of this work was done, but were already well known in science. Meanwhile with the revision of DIN EN 15188 in 2019, adiabatic testing is part of this standard. The experimental setup is the same as for an isoperibolic hot storage experiment. The difference between isoperibolic and adiabatic tests is in the test execution. The oven is preheated to a constant start temperature that is below the self-ignition temperature. When the sample is placed in the oven, it will heat up to oven temperature. Whenever the sample heats up above oven temperature, due to an exothermic reaction, the oven temperature will

be increased to the same level. Thus, sample and oven will always have the same temperature. Consequently there is no heat flow between sample and oven and the boundary of the sample can be assumed as adiabatic.

If the oven temperature can not be increased anymore, the sample will burn away under non-adiabatic conditions. For fast-reacting materials, the power of the oven will not be sufficient to heat as fast as the sample, especially at high temperatures. If the temperature difference between oven and sample exceeds 5 K the boundary conditions will be classified as non-adiabatic.

Under the assumption of adiabatic boundary conditions, the heat conduction term can be neglected, since no energy is transported across the system boundaries. Thus, the energy balance for a static, homogeneous and isentropic system is simplified to equation 2.5.

$$c_p \cdot \rho \cdot \frac{dT}{dt} = \dot{q}_V \quad (2.5)$$

If a zero-order reaction is used to calculate the reaction rate and the reactant consumption is neglected, the heat source can be described by the following equation:

$$\dot{q}_V = \Delta H_h \cdot \rho \cdot k_0 \cdot \exp\left(-\frac{E_A}{R \cdot T}\right) \quad (2.6)$$

If equation 2.6 is inserted into equation 2.5 and the result written in logarithmic notation one obtains equation 2.7, a linear equation with slope  $E_A/R$ .

$$\ln\left(\frac{dT}{dt}\right) = \frac{E_A}{R} \cdot \frac{-1}{T} + \ln\left(\frac{\Delta H_h \cdot k_0}{c_p}\right) \quad (2.7)$$

$$y = m \cdot x + n$$

Figure 2.4 (left) shows the temperature curves resulting from an adiabatic experiment. The heating lasted for approximately four hours, with an subsequent adiabatic part, where the oven followed the sample temperature. After approximately seven hours, the oven reached its maximum temperature and remains constant. The adiabatic boundary conditions were not fulfilled before the indicated adiabatic period (since oven and sample temperatures were different)

due to a limited heating power. Whenever the difference was larger than 5 K, the conditions were not considered as adiabatic.

Plotting  $\ln dT/dt$  versus  $-1/T$  (figure 2.4 (right)), the data graph can be separated into the heating process, the adiabatic conditions and the burn off. The first third of the adiabatic parts appears linear. This behavior could be expected from equation 2.7. The slope of the line equals  $E/R$ . In the data analysis, the steepest slope will be determined because it reflects the highest reaction rate. Calculations were carried out using an Matlab algorithm, as is described in the next section.

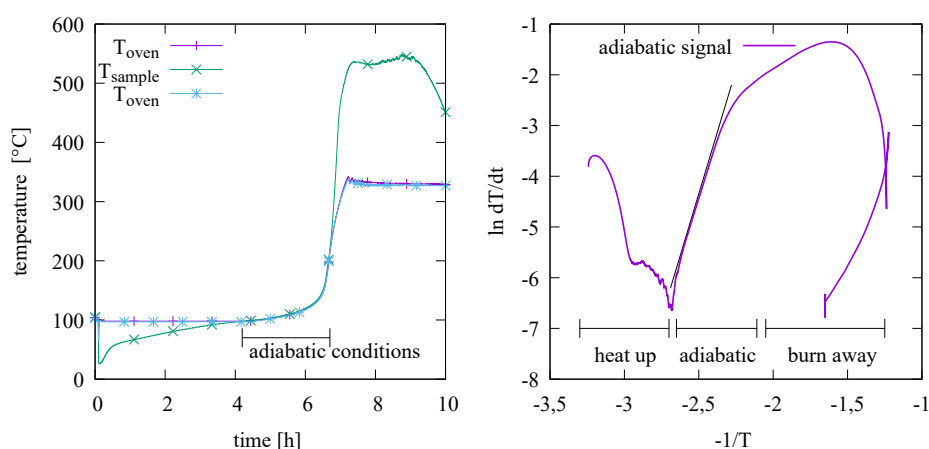


Figure 2.4.: Adiabatic experiment, measured temperatures (left) and calculated signal (right) according to equation 2.7

### Matlab code for test evaluation

In order to evaluate the experimental data, a Matlab code was developed that searches for the steepest slope within the adiabatic part as shown in the right part of figure 2.4 using equation 2.7. The code includes the steps given in the bullet list below.

For calculating the formal kinetic parameters the steepest slope of the adiabatic part in the  $\ln dT/dt$  versus  $1/T$  signal (figure 2.4 (right)) has to be found. This line could be drawn manually. An automated algorithm has to be developed to reduce human error and dependency on operator. Moreover, the input data should not contain temperature drops which occur when the sample is put into the oven and when the maximum temperature is reached (burn off), so that errors due to incorrectly chosen data are reduced.

Since the steepest slope is always between two consecutive data points only, a minimum length of the section of the differentiated temperature-time curve has to be chosen. Different materials, basket sizes and onset temperatures lead to different experimental durations. Therefore, the minimum length of the fitted line has to be variable. Several test runs have shown that lines that contain 10 % to 20 % of the adiabatic part of the data set deliver the best results. For smaller values the line could be within a noisy region, for larger values peaks are flattened out. This is the main weakness of the algorithm. The fact that this parameter can or must be adjusted means that a certain dependence on the operator remains.

To explain the algorithm, a data set of 100 values is chosen. The first line is fitted from data point 1 to 10, the second from 2 to 11, and the last is fitted from 90 to 100. After determining these lines, which each covers 10 % of the data set, the algorithm starts from the first data point and fits lines that each covers 11 % of the data set. The algorithm stops after fitting the last line of the 20 % length the line from data point 80 to 100.

In order to decide if a line was fitted in a noisy dataset or not, the coefficient of determination is used. This coefficient gives the goodness of fit between 0 (bad) and 1 (perfect). It measures how well a dependent variable can be predicted by an independent one.

The set of fitted lines typically contains both good lines and lines within noisy regions. Due to peaks and outliers, steep lines can occur within noisy regions. To eliminate the lines from noisy regions, the best 0.1% of the lines, according to their coefficient of determination, were taken into account. From these lines the steepest one was chosen.

The Matlab Code contains the following operations

- input of temperature and time data
- determining the adiabatic part that fulfills  $|T_{sample} - T_{oven}| < 5 K$
- calculation of  $\ln dT/dt$  and  $-1/T$
- smoothing the data, using moving average with a width of 1 % of all data tuples
- defining a minimum and a maximum length of the lines to be fitted (usually 10 %- 20 % of all data tuples)
- fitting lines in all points with all lengths using Matlab curve fitting toolbox
- calculation goodness of fit of all lines B (coefficient of determination)
- deleting all lines with an B value below 99.9 % of the best one
- choosing the line with the steepest slope
- output of slope, goodness of fit and temperature range where line is fitted

The MATLAB code is attached in Appendix [B](#).

## 3. Materials and material properties

The influence of material properties on the self-ignition behavior and the spread of a reaction front have been reported in many publications for example in [5], [6], [24], [28]. Due to the fact that changing one material property will always change a number of others, it is almost impossible to examine the influence on only one parameter on self-ignition properties. The particle-size distribution, for example, among others, influence the porosity, heat conductivity, permeability and bulk density.

A huge influence on the fluid flow is due to different pore structure parameters, which can be divided into macroscopic and microscopic parameters. The average behavior of the flow through the sample is determined by the macroscopic parameters. These are quite easily measured in a precise way. Microscopic pore structure parameters is a difficult subject because of the significant irregularity of the pore geometry. Pore diameter and pore size are intuitive simplifications of the reality [29]. Using these simplifications, average values can be determined. Moreover, the actual pore shape is quite often far from the tube models that are often used. Therefore, within this work, macroscopic parameters are used, as are defined in this chapter.

### 3.1. Materials

Within this section, a short overview of the used materials is given. Lignite was used as the combustible material because it is used in industry worldwide to produce electricity and heat. Researchers readily admit that global coal fire emission estimates, 40 tons of mercury spewing into the atmosphere annually, and 3 % of the world's annual CO<sub>2</sub> emissions - are imprecise. But the negative implications for human health and global warming, they say, are clear [30].

Silica was chosen as an admixture material because it is quite cheap and easily available in different particle sizes. Magnesium oxide was used since it has a much higher specific surface than the other substances.

## Lignite coal (LC)

Lignite coal is a brownish-black, mostly loose sedimentary rock that was created millions of years ago by the carbonation of organic substances. It is a fossil fuel mainly used for the production of electrical energy. Two types of lignite were used in this work. LC-P was mined in central Germany (Profen) and LC-L was mined in the Lausitz region in Eastern Germany. Both samples were refined by the manufacturer. LC-L was already ground, LC-P was pre-ground only ( $d < 4mm$ ). To ensure a homogenous material for testing, LC-P was ground and mixed again (see section 3.2.1). Since more of LC-P was available for testing, the simulations are based on this coal. Therefore, most of the data were determined for this coal.

To get information about the charification during the combustion, some LC-P was treated thermally. The sample was heated in a thin layer up to 200 °C. Since a direct temperature step from ambient to 200°C results in an ignition, the sample first heated to 100 °C, followed by 10K steps with a hold time of several hours in between. The mass loss was 37 wt.%. This material is referred to as LC-P<sub>tt</sub>, for thermally treated. Since this process was very time-consuming and a lot of samples ignited unintentionally, only one adiabatic test was run with LC-P<sub>tt</sub>. There was not sufficient material for an isoperibolic investigation.

## Sand - silica (S)

The sand used in the tests was quartz sand (silica). Quartz is the trivial name for silicon dioxide ( $SiO_2$ ). Sand is defined as silica if the  $SiO_2$  content is above 85 wt%. A quartz sand with more than 98 wt.%  $SiO_2$  is defined as "industrial sand" [31].



The silica used in this work was manufactured by "Sand-Schulz Spezialsande" and contains more than 96 wt% of  $SiO_2$ . Silica with three different particle-size distributions was used within this work (section 3.2.1).

## **Magnesium oxide (MO)**

Magnesium oxide (MgO) was used as an inert additive. Two fractions with different specific surfaces were used. The MgO dusts have very high specific surface areas compared with the silica (section 3.2.1).

## **3.2. Material properties**

Within this section, the main material properties are given and the measurement methods are explained. Most of the values are used as input parameters for simulation.

### **3.2.1. Particle size, shape and particle surface**

The particle-size distribution was determined for all substances. The coarse sand was measured with the Camsizer (Retsch Technology) by digital image processing, the other substances by the Camsizer XT that is better suited for smaller grain sizes due to the fact that agglomerations of the sample are prevented using pressurized air. Figure 3.1 shows the cumulative particle size distribution of the materials. The x-axis is scaled logarithmic, to show all curves within one diagram. The diameter was found by measuring the volume of the particle and calculating the diameter of a sphere with the same volume.

The specific surface of the particles was measured with helium pycnometry and is given in the key of figure 3.1. The particles were imaged with scanning electron microscope SEM (see Appendix figure A.1). These pictures show that magnesium oxide particles are small with a very irregular surface. The lignite particles are coarser, with a rough surface, while the surface of the sand particles is very smooth.

In case of the silica, the number in the abbreviation is assigned for the largest particle size according to the manufacturer. The number in the abbreviation of the MO gives the specific surface according to the manufacturer.

The materials chosen can be grouped into fine with a high specific surface (MO 130 and MO 150), fine with a low specific surface (S063) and coarse with a low specific surface (S 200 and S 700).

The particle size distribution of the coarse sands shows a quite narrow particle size distribution (steep slope in figure 3.2.1 while the other materials have a wider particle-size distribution that is characterized by a flatter rise.

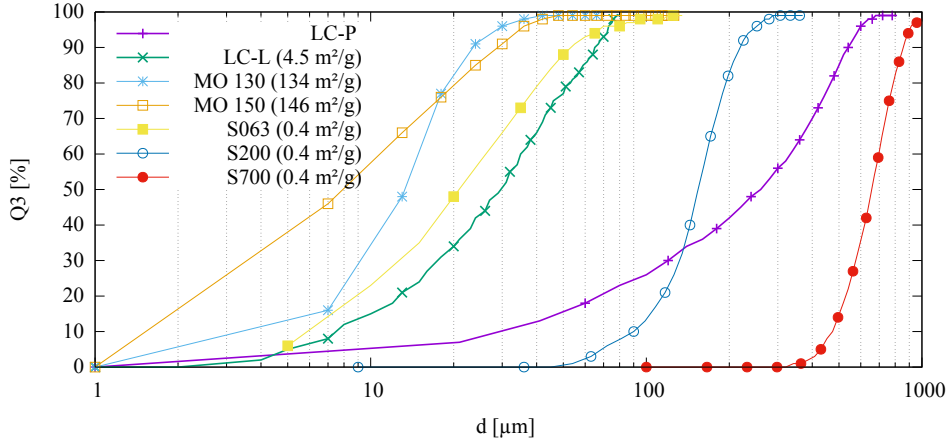


Figure 3.1.: Particle size distribution and surface values (given in the key)

### 3.2.2. Porosity and particle density

The porosity (referred to as voidage)  $\phi$  is the fraction of the bulk volume that is occupied by pores. The porosity is calculated by equation 3.1, which can be simplified to equation 3.2, if  $\rho_{fluid} \ll \rho_{solid}$ . The values with the subscript *bulk* represent the values for the whole bulk material combining fluid and solid material.

$$\phi = \frac{\rho_{solid} - \rho_{bulk}}{\rho_{solid} - \rho_{fluid}} \quad (3.1)$$

$$\phi = 1 - \frac{V_{solid}}{V_{bulk}} = 1 - \frac{\rho_{bulk}}{\rho_{solid}} \quad (3.2)$$

According to Dullien [29], three types of void spaces have to be distinguished:

**interconnected pores** form a path from the inlet to the outlet and contribute to the fluid transport

**dead end pores** are connected to the flow path at one end, but contribute only marginally to the fluid flow

**inner pores** are not connected to the flow path and do not contribute to the fluid flow

The particle density  $\rho_{solid}$  was measured with the helium pycnometry in the department for mechanical process engineering at Otto-von-Guericke-Universität Magdeburg. This method determines the density of the solid within the bulk material by measuring the amount of helium that is needed to replace all the air in the sample. This method does not take inner pores into account. A particle with an inner pore appears less dense than a particle with an open one. The porosity is shifted to smaller values.

The porosities of the mixtures  $\phi$  shown in table 3.1, are based on the solid density of the pure materials, and the bulk density  $\rho_{bulk}$ . The bulk density for the combustibles and mixtures was determined during the experiments shown in figure 5.5 by weighting the sample and measuring the volume of the basket. The values for the pure inert materials was determined using the same methodology. All values of the bulk density are based on at least 10 measurements with new material to exclude inhomogeneities.

Table 3.1.: Porosities and bulk densities of used materials

	$\rho_{solid}$	$\rho_{bulk}$	$\phi$
LC-P	1.46	0.60	0.58
MO150	3.58	0.76	0.79
MO130		0.56	0.84
S063		1.05	0.60
S200	2.65	1.42	0.47
S700		1.51	0.43
LC-P 50 S06350		0.76	0.59
LC-P 50 S03250		0.74	0.60
LC-P 50 MO130 50		0.70	0.72
LC-P 50 MO150 50		0.66	0.63

### 3.2.3. Permeability

Permeability is the conductivity of a porous medium with respect to flow of a Newtonian fluid. This value is of limited use because it may vary within the same porous sample with the properties of the permeating fluid and the transport mechanisms [29].

The more scientific value "specific permeability"  $\kappa$ , which is usually shortened to "permeability", is defined by Darcy's law (see equation 3.3). A much-used unit of permeability is the darcy, which is defined as the permeability of a cube with 1cm side length that will produce a pressure difference of 1atm at a flow rate of  $1\text{cm}^3/\text{s}$  of a fluid with 1cP viscosity. One darcy equals  $0.987\mu\text{m}^2$ .

$$\dot{V} = \frac{\kappa \cdot A}{\mu} \cdot \frac{\Delta p}{l} \quad (3.3)$$

**Typical Values of Hydraulic Conductivity and Permeability**

$-\log_{10} \cdot K(\text{cm/s})$	-2	-1	0	1	2	3	4	5	6	7	8	9	10	11	
<b>Permeability</b>	Pervious			Semipervious					Impervious						
<b>Aquifer</b>	Good					Poor					None				
<b>Soils</b>	Clean gravel		Clean sand or sand and gravel			Very fine sand, silt, loess, loam, solonetz									
						Peat		Stratified clay			Unweathered clay				
<b>Rocks</b>						Oil rocks			Sandstone		Good limestone, dolomite		Breccia, granite		
$-\log_{10} \cdot h(\text{cm}^2)$	3	4	5	6	7	8	9	10	11	12	13	14	15	16	
$\log_{10} k(\text{md})$	8	7	6	5	4	3	2	1	0	-1	-2	-3	-4	-5	

Figure 3.2.: Typical values of Hydraulic Conductivity and Permeability [32]

In geosciences, a usual way to determine the permeability of sand or soil is by saturating it with water and measuring the flow rate at constant pressure [29] [32] (figure 3.2). In order to measure the permeability of the used dusts with air as a fluid, the following experimental setup (figure 3.3) was developed and built. Since it was easier to control flow rate and measure the pressure difference, the setup differs from the standard experimental setup. For controlling the mass flow of air, the red-y mass flow controller GSC by Vögtlin Instruments was used. It was calibrated up to  $10\text{ l}/\text{min}$  air. The error was maximum  $\pm 2\%$  of the end of value. The minimum flow rate, that could be controlled, was  $0.25\text{ l}/\text{min}$ .

Table 3.2.: Measured permeabilities of LC-P and silica at different flow rates [ $m^2$ ]

	0.25l/min	0.5l/min
LC-P	6.8E-10	1.7E-09
S063	4.8E-10	1.0E-09
S200	1.7E-9	1.9E-09
S700	1.6E-8	1.3E-08

Since this value is quite small compared to the error, the flow rate was proven using a pneumatic through. A beaker was filled with water and put upside down into a water filled trough. Air was introduced into the beaker using a tube connected to the flow meter. For different time intervals the amount of air was measured and the flow rate determined. The flow rates were proven several times when the experimental setup was constructed as well as before ev-rate set point of the controller did not show significant differences. A pressure meter, with measurement range up to 50 mbar, was installed downstream of the flow controller.

To ensure an even dust surface at the bottom and to prevent dust from falling into the tube at the bottom, a ceramic filter plate was glued into the pipe. The filter plate has pore diameters of  $10 \mu m$  to  $16 \mu m$  (filter porosity class 4).

At the beginning of an experiment, the pressure loss of the empty apparatus was measured. Afterwards, dust was filled in and the pressure loss of the bulk material only was measured. For the calculation, the pressure difference between the dust and the atmospheric pressure was taken into account. The atmospheric pressure was obtained from the University's weather station located on campus.

Measuring the height of the empty part of the pipe and the mass of the dust, the porosity was calculated. Similar bulk densities ( $\pm 10 \%$ ) as in the hot storage experiments were used. The measurement was repeated three times for each material. In order to reduce the influence of inhomogeneities, the material was not reused.

Equation 3.3 was used to calculate the values shown in table 3.2. Comparing the measured to the literature values in figure 3.2, the used materials can be classified as pervious. Note, that the permeabilities in figure 3.2 are given in  $cm^2$  while the calculated values are given in the SI unit  $m^2$ .

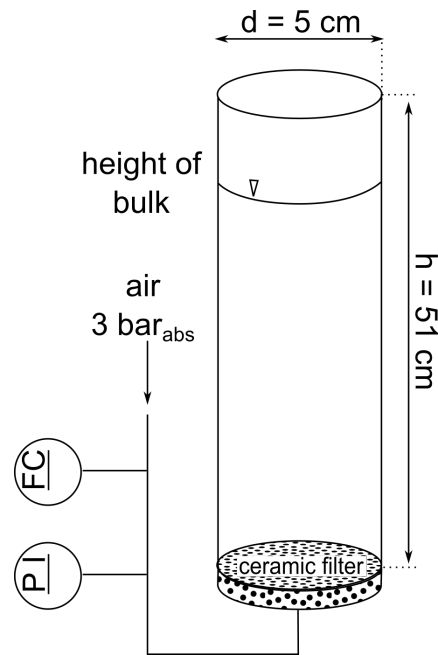


Figure 3.3.: Experimental setup used to measure permeability; FC: flow controller, PI; pressure indicator

### 3.2.4. Heat conductivity

The apparatus used to determine the heat conductivity of the dusts, was developed and patented at BAM by Krause et al. [33]. Due to a heater and a cooler, a stationary heat flow was generated within the apparatus. The temperature was measured within two polyethersulfone (PES) plates with a known heat conductivity. Therefore, the heat conductivity of the sample could be measured contact-freely. The heater and cooler temperatures were set to  $5^{\circ}\text{C}$  respectively  $120^{\circ}\text{C}$  to prevent freezing on the cold side, and ignition of the dust on the hot one.

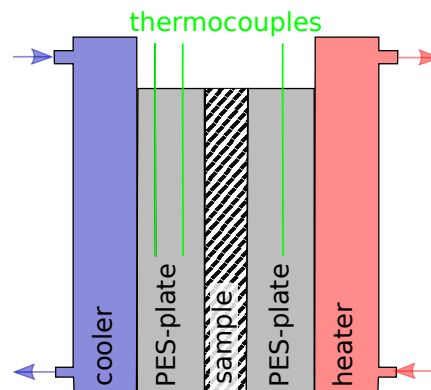


Figure 3.4.: Two-plate apparatus for measurement of heat conductivity

The values measured are shown in table 3.3. Most of the experimental data was part of the Bachelor thesis by Seeger [34]. Furthermore, the porosity was calculated by measuring volume and mass. During the measurement it was made sure that the porosity was kept as close as possible to the values measured during hot storage experiments. The heat conductivity for pure lignite is the smallest compared with that of the pure silica. This can be ascribed to the higher particle conductivity, compare LC-P and S063, and to the changed porosity, compare LC-P and S200. Different particle shapes and, therefore, different contact areas between the particles can also change the results.

Table 3.3.: Measured heat conductivities at given porosities

	$\phi$ [-]	$\lambda$ [W/m·K]
LC-P	0.61	0.09
S063	0.66	0.12
LC-P 50 wt% S063	0.61	0.10
S200	0.51	0.20
LC-P 50 wt% S200	0.58	0.12

### 3.2.5. Proximate analysis

The water (W), ash (A) and volatile (V) amounts were measured using the thermogravimetric analysis TGA 701 LECO. The indices t and d indicate if the value is based on the total amount of the material or on the dry substance. The mass of the sample was measured during a heating-up process from which the composition was calculated. Each step lasted until the weight was constant. The steps were executed as followed:

1. Water content (W): open cup, temperature ramp (6 K/min) to 106 °C flushed with inert gas
2. Volatiles(V): closed cup, temperature ramp (51 K/min) from 106 °C to 950 °C, flushed with inert gas
3. Cooling down to 600 °C (to open the apparatus and remove the lid from the cup)
4. Ash (A): open cup, temperature ramp (26 K/min) from 600 °C to 815 °C, flushed with oxygen

The temperature program follows the ash program according to DIN 51718, 51719 and 51720.

Table 3.4.: Proximate analysis [wt%] for LC-L, LC-P and  $LC - P_{tt}$ ; Values with index  $_d$  are based on dry substance

$LC - L$				$LC - P$				$LC - P_{tt}$			
$W$	9.42			$W$	8.82			$W$	6.34		
$A$	5.44	$A_d$	6.01	$A$	12.78	$A_d$	14.02	$A$	19.73	$A_d$	21.09
$V$	50.44	$V_d$	55.69	$V$	50.26	$V_d$	55.12	$V$	52.07	$V_d$	55.65

LC-L and LC-P contain comparable amounts of water. This is not very surprising since both were stored at ambient conditions. The amount of volatiles is also comparable, but not the amount of ash, which is more than twice as high for LC-P. The thermally treated coal contains much more ash. The remaining amount, that sums up to 100%, is fixed carbon. The name 'fixed carbon' is kind of misleading, since it is defined as everything that was left, after volatiles were evaporated. Beside carbon it contains minor quantities of hydrogen, oxygen, nitrogen and sulfur.

### 3.2.6. Elemental analysis

To specify the composition of the lignite, an elementary analysis was performed. The determination of carbon (C), hydrogen (H) and nitrogen (N) was performed with CHN 1000 (LECO), while for sulfur content (S) CS230 (LECO) was used. It is assumed, that the part that is not C, H, N, O or S is oxygen. The value of oxygen is calculated to sum up to 100% (table 3.5).

Comparing  $LC - P$  and  $LC - P_{tt}$ , it seems, that the amount of oxygen increases during thermal treatment. Considering the raw material, the percentage increases, but the taking the mass loss of 37 wt.% into account the mass of oxygen remains constant ( $LC - P$ : 14.61 g;  $LC - P_{tt}$  : 14.38 g). It can be concluded that the temperature was not sufficient to break the bonds of the oxygen in the coal molecule, or that carbonates and oxides have already formed. Also a physisorption of oxygen at the coal surface is not excluded [35]. Considering at the water and ash free (waf) substance, it seems that oxygen is accumulated. This can be explained by an inaccurate measurement and calculation only, either during subtracting the mass of water and ash from the raw material or when measuring the mass loss.



Table 3.5.: Elemental analysis of the used coals [wt%] for raw material and a water and ash free (waf) substance

$LC - L$			$LC - P$			$LC - P_{tt}$		
	raw	waf		raw	waf		raw	waf
$C$	56.94	66.88	$C$	55.33	70.57	$C$	44.14	59.78
$H$	4.47	5.25	$H$	4.70	6.00	$H$	1.65	2.23
$N$	0.72	0.85	$N$	0.38	0.48	$N$	0.59	0.80
$O$	21.46	25.20	$O$	14.61	18.36	$O$	22.83	30.92
$S$	1.55	1.82	$S$	3.38	4.31	$S$	4.63	6.27

### 3.2.7. Calorific value

The higher calorific value (HCV) was measured using a bomb calorimeter. To calculate the lower calorific value (LCV), the water content measured in the TGA was used (see table 3.4). The calorific values were measured for LC-P and  $LC - P_{tt}$  only. With the molar mass of the apparent fuel molecule (see section 6.5) the values can be recalculated into  $\text{kJ/mol}$  as shown.

Table 3.6.: Calorific values of LC-P and  $LC - P_{tt}$

$LC - P$			
$HCV$	22,817 $\text{kJ/Kg}$	$LCV$	21,580 $\text{kJ/Kg}$
$HCV$	3737 $\text{kJ/mol}$	$LCV$	3,543 $\text{kJ/mol}$
$LC - P_{tt}$			
$HCV$	13,974 $\text{kJ/Kg}$	$LCV$	13463 $\text{kJ/Kg}$
$HCV$	670 $\text{kJ/mol}$	$LCV$	647 $\text{kJ/mol}$

### 3.2.8. Heat capacity

Gröber solved the instationary heat transfer equation for simple geometries like infinite plates, spheres and infinite cylinders using a Bessel function. Applying these equations, the heat capacity of a substance can be derived from a heating-up process [36].

Honza [37] developed in his Master's Thesis an experimental setup and evaluation method based on Gröber' work for gaining a  $c_p$  value from an heating up process in a hot-storage oven. As a result of his work, the heat capacity could be determined and is shown in figure 3.5 as a function of the temperature during heating. Since heat generation from combustion or consumption

from evaporation would modify the results, dried samples had to be used and the experiments had to be conducted at temperatures below  $T_{SI}$  to prevent ignition. For  $LC - P$  a heat capacity of  $1200 \frac{J}{kg \cdot K}$  was determined and used within this work. The silica sample was chosen to validate the measurements as the heat capacity of silica as pure  $SiO_2$  is well known [38]. The curve for the 50/50 mixture is in between the pure substances.

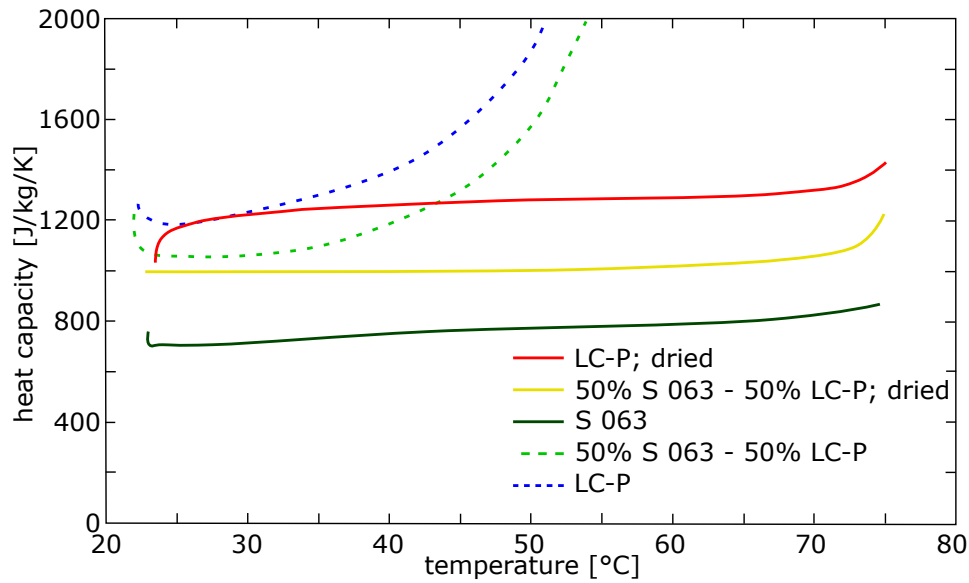


Figure 3.5.: Heat capacity of LC-P and silica lignite mixtures calculated from a heating process using the Gröber solution [37]

## 4. Experimental setup

This chapter gives an overview over the experimental setups.

Within the chapter 4.1, hot-storage experiments are discussed. A sample size between 0.1 l to 25.8 l is stored under isoperibolic or adiabatic conditions. The outcome of these experiments are time-dependent temperature curves. From them, maximum reaction temperatures, self-ignition temperatures, induction times and formal kinetic data can be derived.

The typical sample container for hot storage experiments is made from wired mesh, while the gas transportation occurs through natural convection and diffusion. To explore other conditions, additional measurements in a pipe were conducted as described in section 4.2. This pipe was flushed with air (forced convection). After self-ignition occurred at the top, a reaction front propagated downwards that can be tracked with thermocouples along the central axis. The outcome of this experiment are temperature-time curves that allow determining maximum reaction temperatures and speeds of reaction fronts.

Furthermore, experiments with an STA (simultaneous thermal analysis) were conducted (see section 4.3). The sample mass was much smaller than in the experiments described in sections 4.1 and 4.2, typically a few milligram. These experiments deliver mass and heat-flow curves as functions of temperature. The total mass loss of a sample that occurred until a certain temperature, can be measured. Additionally, the heat that is released or consumed by the sample is measured. These data give an idea of the reaction course and thermal tint (exothermic or endothermic). Furthermore, formal kinetic data can be extracted.

Since the heat that is released by combustion, depends on the completeness of the reaction, gaseous products were measured by FTIR (see section 4.4). An FTIR coupled to the SEDEX oven and one coupled to the STA were used. With these concentration- time and concentration-temperature curves, the the

occurrence of gasses in general, especially the reaction course as well as the completeness of the reaction can be determined.

The data obtained from the setups described above was used to establish a complete image of the reaction phenomena, on one hand. On the other hand, it also constituted input data for the simulation.

## 4.1. Hot storage experiments

Self-ignition temperatures, induction times and activation energies can be determined by isoperibolic and/or adiabatic hot storage experiments. Adiabatic and isoperibolic tests differ in their way of heating (see 2.3.2 and 2.2). The tests executed within this thesis were based on the experimental setup in the European Standard DIN EN 15188 [15]. Seven different ovens were part of the laboratory equipment (see Table 4.1). The only difference compared with the European standard was that no inner chamber was used. The inner chamber consists of a thin metal sheet to ensure a homogenous temperature profile. The sample was placed directly in the oven. Since the heaters in oven 1 and 2 are behind walls and in oven 3 - 6 top, bottom and the side walls are heated, this difference can be neglected. Measurements of the temperature profiles in the ovens suggests that, therefore a comparison with an without inner chamber have not been conducted.

Table 4.1.: Overview over the laboratory ovens

Nr.	Name	V [l]	$l \times w \times d$ [cm]	mechanical ventilation
1	Heraeus T6060	57	$37 \times 40 \times 38$	no
2	Heraeus T6060	57	$37 \times 40 \times 38$	no
3	Memmert UFEP500	108	$56 \times 48 \times 40$	possible
4	Memmert UFP800	749	$104 \times 120 \times 60$	possible
5	Memmert UFE500	108	$56 \times 48 \times 40$	possible
6	Memmert UFE500	108	$56 \times 48 \times 40$	possible
S	SYSTAG TSC 511 SEDEX	10	$20 \times 20 \times 25$	yes

The heating elements in oven 1 and 2 are placed behind panels in the side walls. The air in the oven is convected due to buoyancy behind these panels. The scavenging air enters the oven at the bottom behind the heating panels and

is heated up before it enters the oven at the top. Additionally, gas is looped around within the oven since cold gasses are sucked in at the bottom. The outlet is at the center of in the upper part of the back wall of the oven. The outlet is 4 cm in diameter (see figure 4.1 (a)).

Temperature control in oven 1 and 2 as well as temperature measurement, in general, were realized using a self-written LabVIEW program.

Temperatures were measured with type-K sheath thermocouples 1 mm in diameter. One thermocouple was placed in the center of the sample. Two thermocouples were placed in the oven halfway between the sample and the oven wall to determine the oven temperature. The temperature data were logged with a National Instruments Compact RIO System equipped with three NI 9213 16 channel thermologger modules with cold-junction compensation. The logging interval was set to 30 s.

The relays for the heaters in ovens 1 and 2 were replaced by semiconductor relays that were actuated by a National Instruments Compact RIO relais card. The temperature control was performed using by a P-Controller. The average temperature of the two thermocouples that measure oven temperature at central sample height, is used for controlling the temperature. There was no difference between the appointed temperature and the imposed temperature. The setpoint of the controller can be a fixed preset value (isoperibolic hot storage) or the sample temperature (adiabatic hot storage).

In ovens 3 - 6, the heating elements are placed directly at the top, bottom and side walls of the oven. The scavenging air enters at the bottom of the oven and is preheated in an separate chamber. The temperature in the oven is controlled by two PT 100 resistance thermometer directly below the ceiling. This results in a difference between the oven temperature and the temperature at sample height. These ovens are equipped with a ventilator for forced convection to allow other applications like drying a sample. The ventilator was switched off for all experiments, since forced convection was not desired. Ovens 3, 5 and 6 are identical in their structures, the only difference is an exhaust flap operated manually or electrically (see figure 4.1 (b)).

The SYSTAG TSC 511 SEDEX (see figure 4.2 for the SEDEX setup, figure 4.6 shows the coupled FTIR) was used for the gas measurements since the FTIR sampling unit could easily be attached. The oven was controlled via

#### 4. Experimental setup

two 1.5 mm PT 100 that were located at sample height in the oven and within the sample. Additionally, two 1 mm type-K thermocouples were attached since PT 100 can measure temperatures up to  $500^{\circ}\text{C}$  only. Usually, maximum reaction temperatures are significantly higher. The oven is heated by a hot air fan only, located at the back wall. The gas/air is circulated inside the oven. There are no openings that allow natural air exchange with the surroundings, but the oven is flushed with  $1\frac{1}{\text{min}}$  air. This value is justified by the sampling rate of the FTIR, that is as well  $1\frac{1}{\text{min}}$ , and by the work of Bauszus [39] who compared maximum reaction temperatures in the hot storage ovens with maximum temperatures in the Sedex. Bauszus found out, that the maximum reaction temperature is much lower if the Sedex oven is not flushed with air due to lack of oxygen. If the Sedex is flushed with  $1\frac{1}{\text{min}}$ , maximum reaction temperatures equal the values determined in the other ovens.

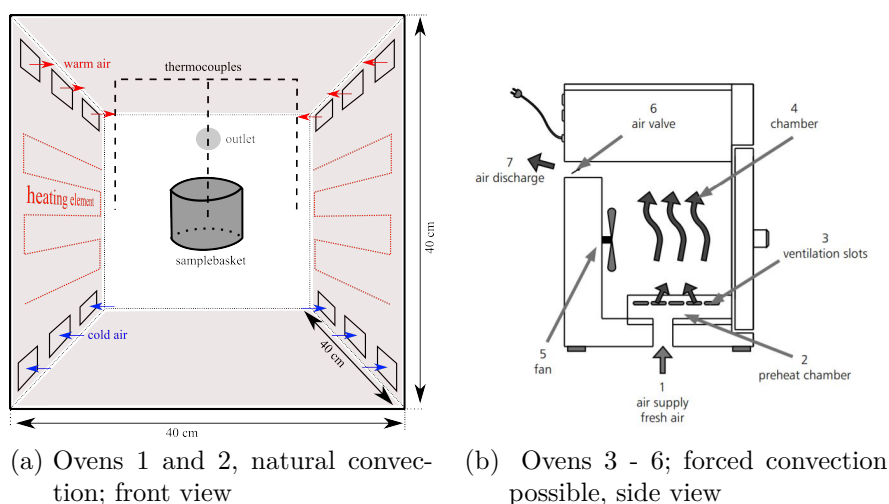
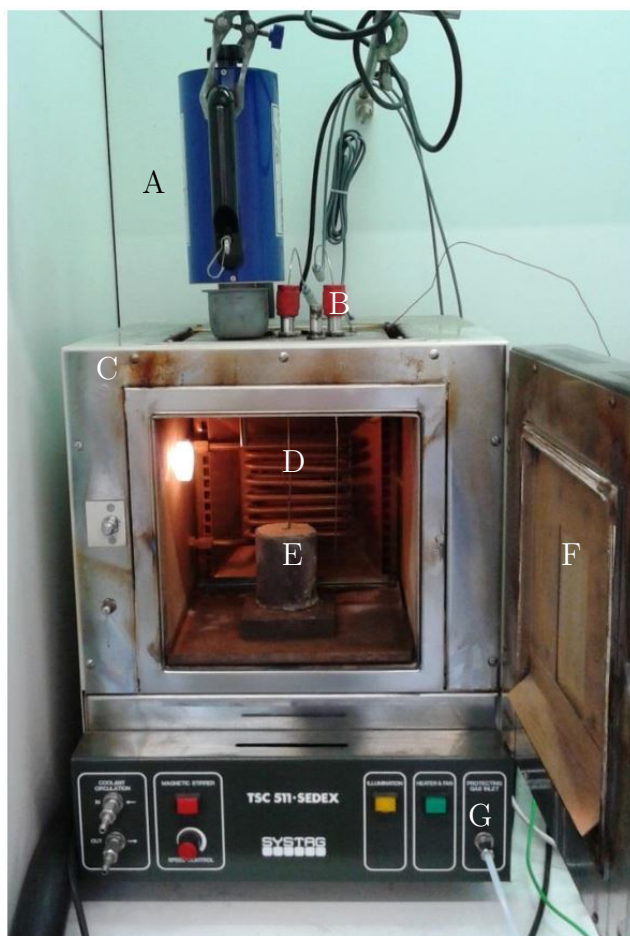


Figure 4.1.: Design of oven types 1 - 6

The samples were put into wired mesh cylinders to ensure sufficient oxygen access to the sample. The mesh opening was 0.4 mm, the wire was 0.25 mm in diameter. The mesh was made from stainless steel. There is a difference between the nominal volume and the actual volume of the basket due to manufacturing errors. The volumes used within the text of this work are the nominal volumes, whereas the actual volume of the basket were used in the calculations. The basket volumes were measured using a bulk material with known density.

#### 4. Experimental setup

---



- (A) FTIR sampling unit
- (B) thermocouples
- (C) oven casing
- (D) ventilator (behind wall)
- (E) sample
- (F) door with window
- (G) purge gas inlet

Figure 4.2.: Experimental Setup SYSTAG TSC 511 SEDEX with FTIR sampling unit

## 4.2. Forced convection experiments

In order to investigate the influence of oxygen supply on the ignition and propagation of the smoldering front, experiments with a closed boundary and a forced air flow from the top to the bottom were performed. A pipe ( $d = 50\text{ mm}$ ,  $h = 330\text{ mm}$ ) was installed in laboratory oven 4 (Memmert UNP 800) with an internal volume of 749l heated to a constant temperature. To ensure that the temperature of the scavenging air was equal to the oven temperature, a copper coil was installed at the top of the oven to heat it. An empty chamber at the top of the pipe ensured that the flow settles before it enters the sample. The temperature was measured along the vertical axis of the pipe with type-K sheath thermocouples 50 mm apart at the center of the pipe (see figure 4.3). Ignition was induced by self-ignition at the top of the pipe due to the high oxygen concentration at the inlet. The smoldering front moved in the same direction as the air flow (forward smoldering, figure ??). [26]

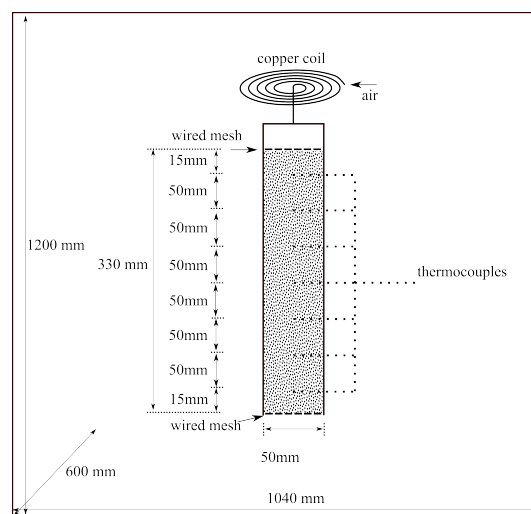


Figure 4.3.: Experimental setup; pipe experiments

## 4.3. Simultaneous thermal analysis, with coupled FTIR

The samples were also examined by simultaneous thermal analysis (STA), see figure 4.4, coupled with a Fourier-transformed infrared spectrometer (FTIR) for analyzing the composition of gaseous reaction products (Setaram Labsys



evo with Thermofischer Nicolet iZ10). STA is a combination of thermogravimetric analysis (TG) and differential scanning calorimetry (DSC). The initial sample mass was approx. 20 mg [26].

### Thermogravimetric analysis - TG

A thermogravimetric analysis measures the mass of a sample treated with a prescribed temperature-time program. A mass change occurs when a solid or fluid reacts to gaseous products. A mass loss may be due to evaporation, decomposition and oxidation, or dehydration. The sample was placed within an oven. A scale measures the mass of the sample, while the oven was heated in a specified way, usually a temperature ramp. Oxidizing or inert atmospheres can be realized by changing the purge gas.

### Differential-scanning calorimetry - DSC

The differential-scanning calorimetry measures the difference in heat release or heat absorption of a substance-filled crucible compared to an empty reference crucible. Both crucibles are placed on a disk with a high heat conductivity. The temperature of the disk is measured close to each crucible. The heat flow can be calculated, as it is dependent on the temperature difference. If no reaction takes place, the temperature difference between the crucibles is zero and, therefore, the heat flow is zero. If due to a thermal change within the sample (melting, evaporation or oxidation for example) a temperature difference occurs, the heat flow can be calculated.

The tests were carried out using a LABSYS evo (see figure 4.4). The DSC was coupled to an Nicolet iZ10 FTIR that was calibrated for  $CO$  and  $CO_2$ . The samples were investigated under synthetic air ( $N_2$  with 20.9% vol.  $O_2$ ). Open  $Al_2O_3$  crucibles were used. Before every experiment the baseline of the corresponding crucible was determined.

The activation energy can be calculated using the DSC or the TG signal. Methods like Ozawa-Flynn-Wall (see equation 4.1) use a coherence between heat rate  $\varphi$  and maximum peak temperature  $T_{peak}$  (equation 4.1). This method requires determining a temperature of a given peak, which is not easy, since the

#### 4. Experimental setup

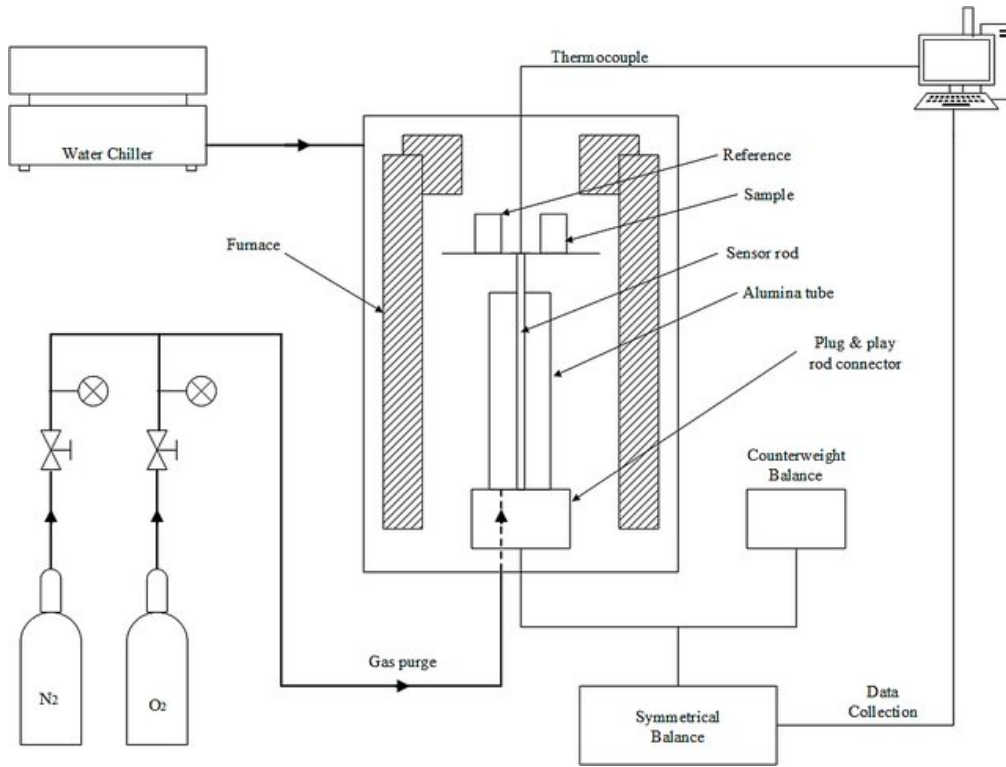


Figure 4.4.: Experimental setup of the used STA (LABSYS evo.) [40]

measured curves show very wide, plateau like peaks or two peaks (see figure. 5.12). For that reason this method was not used.

$$\varphi = konst - 0.4567 \frac{E}{R \cdot T_{peak}} \quad (4.1)$$

Another method for calculating the activation energy is provided by Torrent and Querol [41] and was used in a previous study [25]. The formal kinetic data were calculated using equation 4.2, or its logarithmized form in equation 4.3.

$$\frac{dm}{dt} = -m \cdot k_0 \cdot \exp\left(\frac{E}{R \cdot T}\right) \quad (4.2)$$

$$\ln\left(\frac{dm}{dt}\right) = \ln(-m \cdot k_0) \cdot \frac{E}{R} \cdot \frac{1}{T} \quad (4.3)$$

Drawing a  $\ln(-1/m \cdot dm/dt)$  vs.  $1/T$  diagram results in a line with the slope that equals the activation energy. Therefore, the algorithm, provided in section 2.3.2 was used, applied to equation 4.2. The results are summarized in table 5.2.

## 4.4. Fourier-transformed infrared spectroscopy-FTIR

The FTIR-spectroscopy is a method to examine the interactions of electromagnetic radiation and molecules. Information on the oscillation of molecules and functional groups can be obtained. An infrared spectrum is determined by sending infrared radiation through the sample and measuring the adsorbed part of the energy as a function of the wave number. The peaks of the adsorbed parts are characteristic like a fingerprint for each molecule.

Infrared (IR) radiation has enough energy to cause transitions in the levels for vibrations and rotations in the molecule. IR radiation interacts with molecules in the gas phase. This changes the dipole moment of the compound. In the case of similar diatomic gases such as  $N_2$ ,  $O_2$  and  $H_2$  as well as noble gases, the dipole moment does not change. Thus, these gases are not detectable by FTIR.

Different molecules adsorb at different wavelengths. Two spectra are never identical. An IR spectrum contains both qualitative and quantitative information on the sample. Further details can be found in [42].

As seen in figure 4.5 the mirrors are arranged in the system in such a way that they form an interferometer. The beam is split into two individual beams. One of them is directed towards a fixed mirror, the other onto a movable mirror. Then the two beams are recombined so that they interfere, depending on the frequencies contained in the beam and the mirror path. This results in an interferogram with a large center burst when the mirrors were equidistant from the beam splitter and thus all frequencies interfere additively, and relatively flat wings. The interferogram is then converted into a spectrum via a Fourier transformation [43].

The main parts of the FTIR are:

**radiation source** In FTIR, black (gray) bodies are used to produce infrared radiation. The source used in this FTIR was made of SiC and was heated to 1500 K.

**optical path** The radiation produced by the source is focused and aligned by mirrors, apertures and lenses.

**interferometer** The interferometer used is a so called Temet-carrousel interferometer. This interferometer is more exact than the simpler Michelson interferometer, that was widely used formerly, but the principle is the same. The infrared beam is splitted. One part is reflected on a fixed mirror the other part on a moving mirror. The two beams are combined and interfere depending on the position of the moving mirror (see figure 4.5).

**sample chamber** The interfering infrared radiation enters the chamber that contains the sample. The walls of the chamber are coated with a noble metal to prevent corrosion. The beam is reflected within the chamber to 'scan' as many gas molecules as possible.

**detector** There are two categories of detectors: thermal detectors (DTGS) and quantum detectors (MCT). In the used FTIR a peltier cooled MCT is installed.

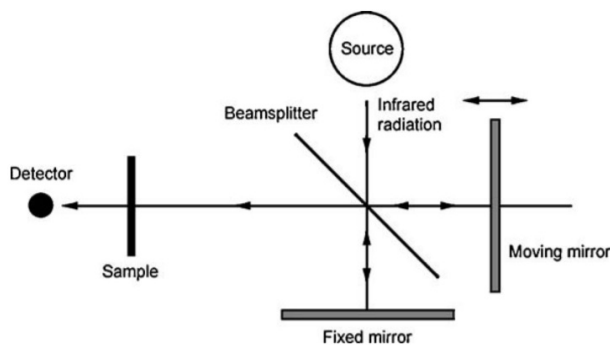
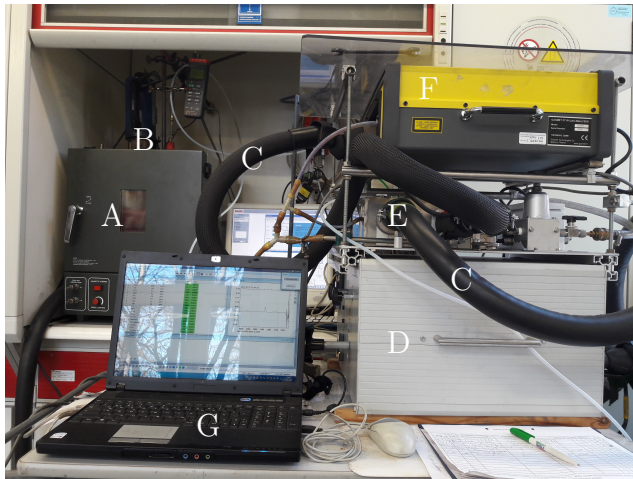


Figure 4.5.: Schematic view of a Michelson inferometer in an FTIR, an simple version of the Temet-carrousel [44]

The FTIR (ANSYCO Gasmeter Dx-4000) was coupled to the SEDEX oven used to evaluate the resulting gases (see figure 4.6). A pump (Ansyco SYCOS P-Hot) allowed the extraction of a gas sample from the oven. The sampling unit, the pump and all hoses were heated up to 180 °C to minimize condensation of the sampled gasses in the experimental system. For further protection of the

#### 4. Experimental setup

---



- (A) Sedex Oven
- (B) Sampling unit
- (C) Hose
- (D) Pump with filter
- (E) Dilution unit
- (F) FTIR
- (G) Computer / Software

Figure 4.6.: Experimental setup of the FTIR and sampling unit attached to the SEDEX oven

experimental apparatus and to dilute high-concentrated gasses, the gas sample was diluted with compressed air to 10 % of the initial concentration. This took place separately in an additional device via a critical nozzle. The FTIR was calibrated by the manufacturer with  $H_2O$ ,  $CO_2$  and  $CO$  using sample gas. Additionally, the calibration spectra of  $CH_4$ ,  $N_2O$ ,  $NO$ ,  $NO_2$ ,  $SO_2$ ,  $HCl$ ,  $NH_3$ ,  $HCN$ ,  $CH_3OH$ , *Benzol*, *Formaldehyd* and *Acrolein* from an identical constructed device were used. These calibration points are less accurate than the directly calibrated ones. The calibration points are shown in the appendix page [iv](#).

## 5. Experimental results

Within this chapter, the results, measured or calculated from the experiments described in chapter 4 and using the theory in chapter 2, are given.

### 5.1. Isoperibolic hot storage

This chapter reports the results from isoperibolic and adiabatic hot-storage tests. The formal kinetic data has been calculated, and the influence of inert admixtures on the maximum reaction temperature is given.

#### 5.1.1. Formal kinetic data

The results from the isoperibolic hot-storage tests are shown in table 5.1, the corresponding Arrhenius diagram is shown in figure 5.1. These coals have slightly different self-ignition temperatures due to their different chemical composition (see table 3.5).

The mixtures with silica were made with lignite coal from the Lausitz region (LC-L). As silica did not participate in reactions, it acts as a heat sink only. Therefore, the self-ignition temperature  $T_{SI}$  increases with an increasing amount of inert material. This effect was also seen in [3] on the materials used there. However, since other materials were used in [3], the data are not directly comparable.

Comparing the  $T_{SI}$  of the different mixtures, consisting of different silica with the same admixture fraction, no increase of  $T_{SI}$  is evident within measurement uncertainties, which can be estimated to be 2 K (see chapter 7). A dependency of the self-ignition temperature on the inert particle size was not found. The slope in the Arrhenius diagram and, therefore, the activation energy is almost

the same for both coals as well as the lignite-silica mixtures. This indicates that the inert material does not change the average overall formal kinetic properties. For further testing and simulation LC-P was used. An activation energy of  $110 \text{ kJ/mol} \pm 1.63\%$ ; y-intercept  $n = 53 \text{ K}^2/\text{m}^2 \pm 1.1\%$  was measured.

Table 5.1.: Self-ignition temperatures [ $^{\circ}\text{C}$ ] and activation energies [ $\text{kJ/mol}$ ] for Lignite and Lignite Silica mixtures (mixtures were made with LC-L); LC-P [45]; LC-L and mixtures [26]

V [l]	LC-P	LC-L	20% S063	40% S063	20% S200	40% S200	20% S700	40% S700
0.1	123	118	122	126	123	128	124	128
0.2	117	114	116	121	116	122	118	123
0.8	105	101	104	109	105	110		
1.6	101	96	99	103			100	104
3.4	95	91	94	98	94	100		
6.4	91							
13.2	85							
25.8	82							
E [ $\text{kJ/mol}$ ]	110	105	105	99	104	108	107	101

For simulation the pre-exponential factor was calculated using equation 5.1, which can be obtained from equation 2.4. As material properties  $\rho = 710 \text{ kg/m}^3$ ,  $\lambda = 0.082 \text{ W/mK}$  and  $E = 110 \text{ kJ/mol}$  were used.

For the mass-related heat of combustion  $Q$ , the value measured with the STA ( $Q = 1320 \text{ J/g}$ ) was used to ensure realistic conditions. The value measured in the bomb calorimeter would have been much too high, since it assumes a non-realistic complete combustion. The pre-exponential factor can be determined as  $k_0 = 1.1 \cdot 10^9 \text{ 1/s}$  for LC-P using equation 5.1.

$$n = \ln \left( \frac{E_A \cdot Q \cdot \rho \cdot k_0}{R \cdot \lambda} \right) \quad (5.1)$$

Table A.5 shows the increase of the  $T_{SI}$  for silica and magnesium-oxide mixtures compared with the pure combustible. The absolute values are not comparable: Some of the experiments with sand and magnesium oxide were carried in different ovens, with a different set of thermocouples, while other experiments took place later, with aged material. Some experiments had different particle size due to an defective grinding machine. These effects influence the whole test series and, therefore, increases in  $T_{SI}$  are comparable. It can be shown,

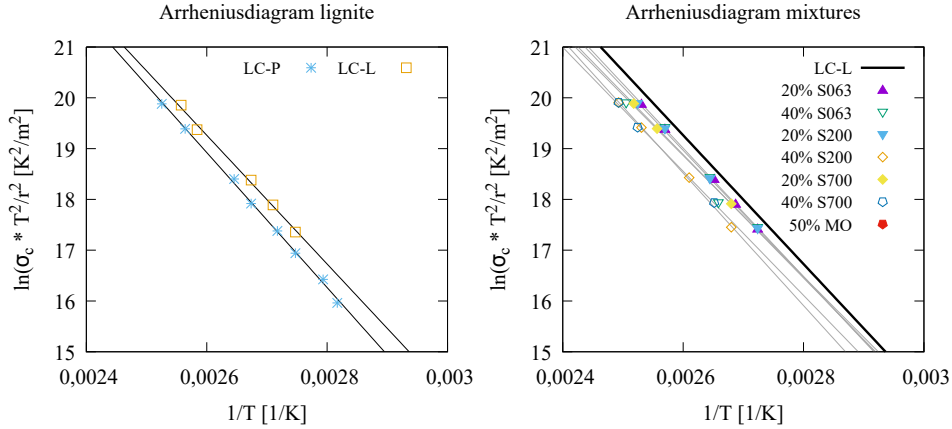


Figure 5.1.: Arrhenius diagram for Lignite and Lignite Silica Mixtures

that the increase in  $T_{SI}$  is independent of the inert material, the particle size, and the specific surface and only depends on the mass fraction of the inert material within the measurement uncertainty. The corresponding Arrhenius plot is shown in figure A.8.

### 5.1.2. Maximum temperatures

The data presented within this section has in part been published in [46].

During the hot-storage experiments, the maximum reaction temperatures were determined. The data is part of the Bachelor thesis by Arsand [47] and was partly published in [26]. Figure 5.2 shows the maximum reaction temperatures of all experiments that ignited during the determination of the formal kinetic data. Therefore, the amount of data available for each sample size respectively mixture differ. For clarity, mixtures with magnesium oxide are shifted slightly to the right of the corresponding volume.

The reaction temperature of mixtures with the coarse silica S200 and S700 is similar to or below the average maximum reaction temperature of the pure lignite. Furthermore, the maximum reaction temperatures of mixtures with the coarse sands did not sort by admixture fraction.

In contrast, almost all maximum reaction temperatures of the mixtures with fine sand are significantly above the maximum reaction temperature of the



pure lignite. The highest maximum temperatures were obtained by admixing magnesium oxide that is slightly finer than S063.

With the fine silica, all maximum reaction temperatures sort by the admixture fraction of inert material. The higher the amount of fine silica, the higher the maximum reaction temperature. This statement is not valid for magnesium oxide, since not enough data points are present.

It can be concluded that coarse sands did not have an influence on the reaction temperature, or might have a temperature reducing effect, while fine inert material increased the reaction temperature. An amount of more than 60% inert material leads to a reduced temperature, probably since the amount of combustible material will be too low (see figure 5.3).

Outliers can be explained by the fact that the line shows the average temperature of lignite only. On the other hand, a shifted thermocouple, that is no longer within the center of the sample, can lead to significant errors.

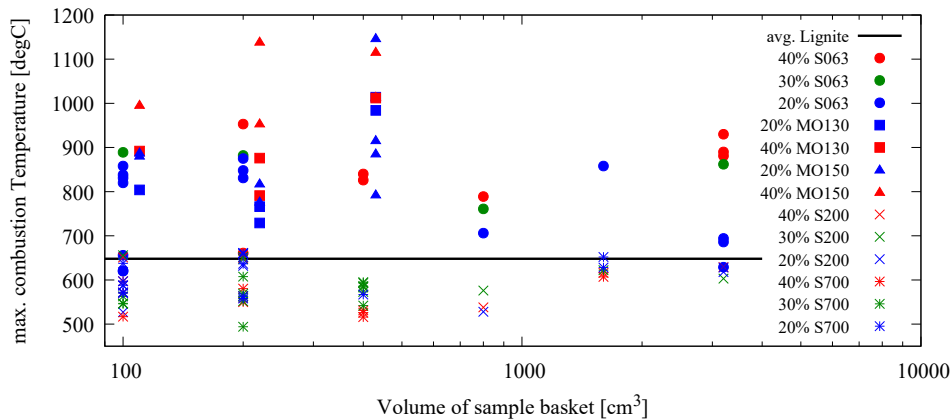


Figure 5.2.: Comparison of the maximum combustion temperatures of Lignite (LC-L) Silica Mixtures and LC-P Magnesium oxide Mixtures. In part taken from [47] [26]

To gather more information about the influence of the mixing fracture on the maximum reaction temperature, a test series with different LC-P MO150 mixtures was performed (see figure 5.3). All experiments were carried out at 150 °C. Mixtures containing more than 60% inert material did not ignite due to the increase of the SIT. The maximum reaction temperature of pure lignite was 715 °C. An admixture of 2.5 wt.% of MO150 increased this temperature by 51 K. The maximum temperature 1232 °C was measured at a mixture fraction

of 50 % inert material, an increase of 42%. The maximum reaction temperature of the 60 % mixture is lower, probably due to the decreasing amount of combustible material. Note that the increase of the reaction temperature is at the end of the combustion process.

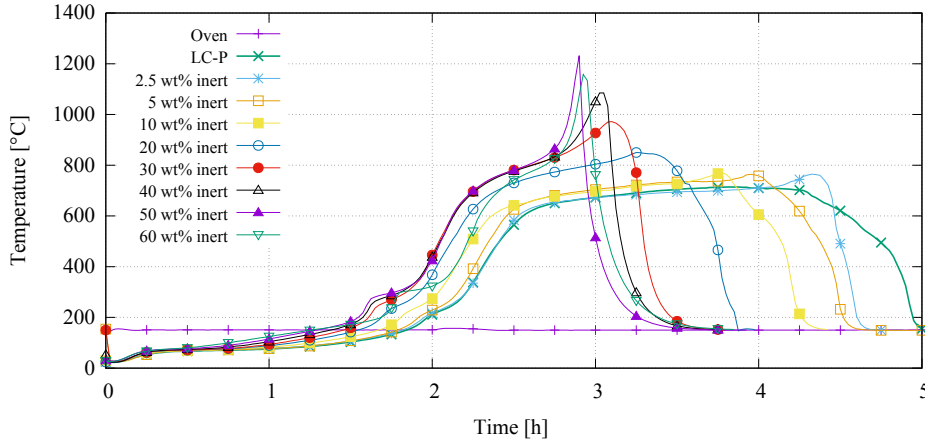


Figure 5.3.: Evolution of temperature in basket showing self-heating and self-ignition, for mixtures of lignite coal and MO150 in a  $100 \text{ cm}^3$  sample basket;  $T_{oven} = 150 \text{ }^\circ\text{C}$  [46]

One reason for higher temperatures can be a higher reaction rate, which should be reflected in a higher mass loss. Therefore, mass was measured during two hot-storage experiments. Figure 5.4 shows the experimental data. The normalized mass of lignite is given with the amount of inert material subtracted. The noise in the mass signal has several causes.

Firstly, the material sticks to the thermocouple and falls down as the sample shrinks during combustion.

Secondly, the thermocouple undergoes thermal expansion when heated up. As it is fixed at the ceiling, it pushes down (sample seems to be heavier). This can be seen in figure 5.4 at 4.5 h in the 50 % MO 150 signal. At the moment, the run-away reaction started, temperature rise was high and therefore thermal expansion as well, the sample seemed to gain mass for a short period of time. This was caused by the thermocouple drilling into the sample and applying a downward force.

Thirdly, the leverage of the scale sticks to the oven casing due to tar condensating at the cold gap. Nevertheless, it is clear that there is no mass loss matching

the increase of the temperature. A higher reaction rate is not a possible cause for the higher reaction temperatures.

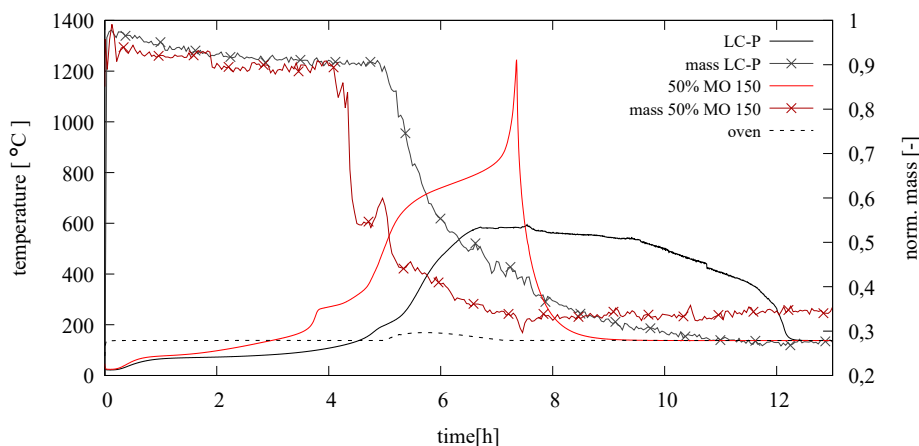


Figure 5.4.: Temperature and mass curves of 100 % lignite and 50 % admixed MO 150; mass is normalized to the mass of lignite

Figure 5.5 shows a box plot of the peak temperatures occurring for mixtures of 50 %wt lignite with different inert additives. Each box plot is based on ten experiments, except S032, which is based on three due to the demanding sieving process. During the MO130 experiments, the thermocouple tip broke as a result of the high temperature and the reducing atmosphere, causing the higher variance observed for this series. The thermocouple finally broke during the last-but-one test, but misleading temperatures probably have been recorded even during the previous experiments. Every additive leads to a reaction temperature at least 275 K above pure lignite. The peak temperatures of mixtures with S063, S032 and MO130 are within the same range. All three substances have similar particle-size distributions. MO150 leads to significantly higher temperatures than MO130. They have similar specific surfaces, but MO150 contains much more fine material. It can be concluded that the resulting higher reaction temperatures depends mainly on the particle size of the inert material [46].

After each of the experiments shown in figure 5.5, the height of the residue in the sample basket was measured. Pure lignite shrank to 58 % of its original height. As a consequence, the center thermocouple was no longer in the middle of the sample, but rather at the top layer, with embers, at the end of the combustion process. This leads to an underestimation of the ember temperature since the thermocouple was cooled by the surroundings. This effect is shown

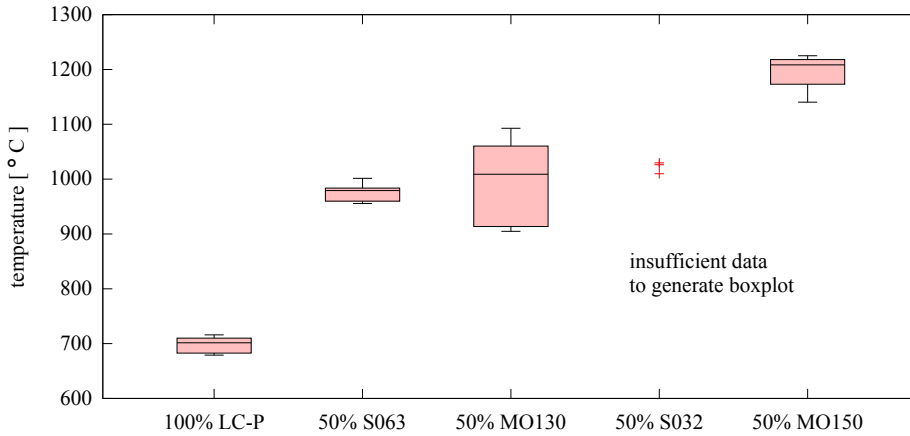


Figure 5.5.: Maximum temperatures resulting from the self-ignition and combustion of lignite and mixtures containing lignite with 50 %wt. of inert additives. Box: 25 % and 75 % quantile with median, whiskers: max. / min. values [46]

in figure 5.6. By contrast, the average residue height of the silica mixtures was about 83 %, and of the magnesium oxide mixtures 96 % of the basket height. Between the experiments with the different silica, as well as within the experiments with the different magnesium oxides, was difference in residue height was measurable. This could be ascribed to unintended vibrations during the detachment from the oven on the one hand, on the other to a non-planar residue surface, which makes determination of the exact height difficult.

Nevertheless, these values are values over of all experiments and show a significant difference in residue height in between pure lignite and the admixtures. The inert materials have nearly no loss in mass and volume. It is conceivable, that the inert particles form a supporting structure that keeps the lignite particles in place during the shrinking process, see figure 5.6.

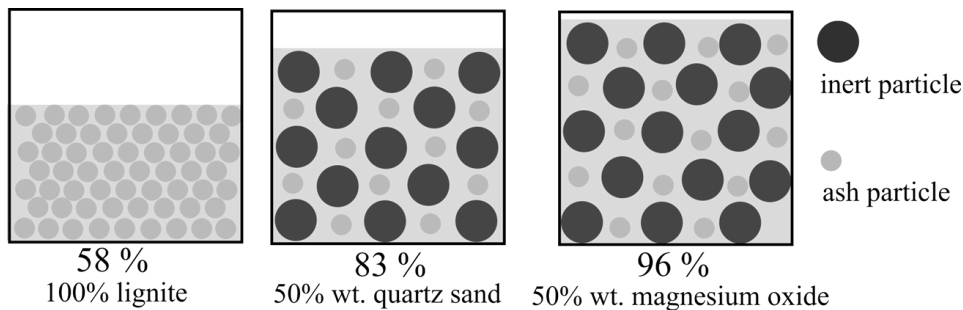


Figure 5.6.: Schematic view of the ash height of an finished hot storage experiment.  $V_{basket} = 100cm^3$ . (Particle sizes not to scale)

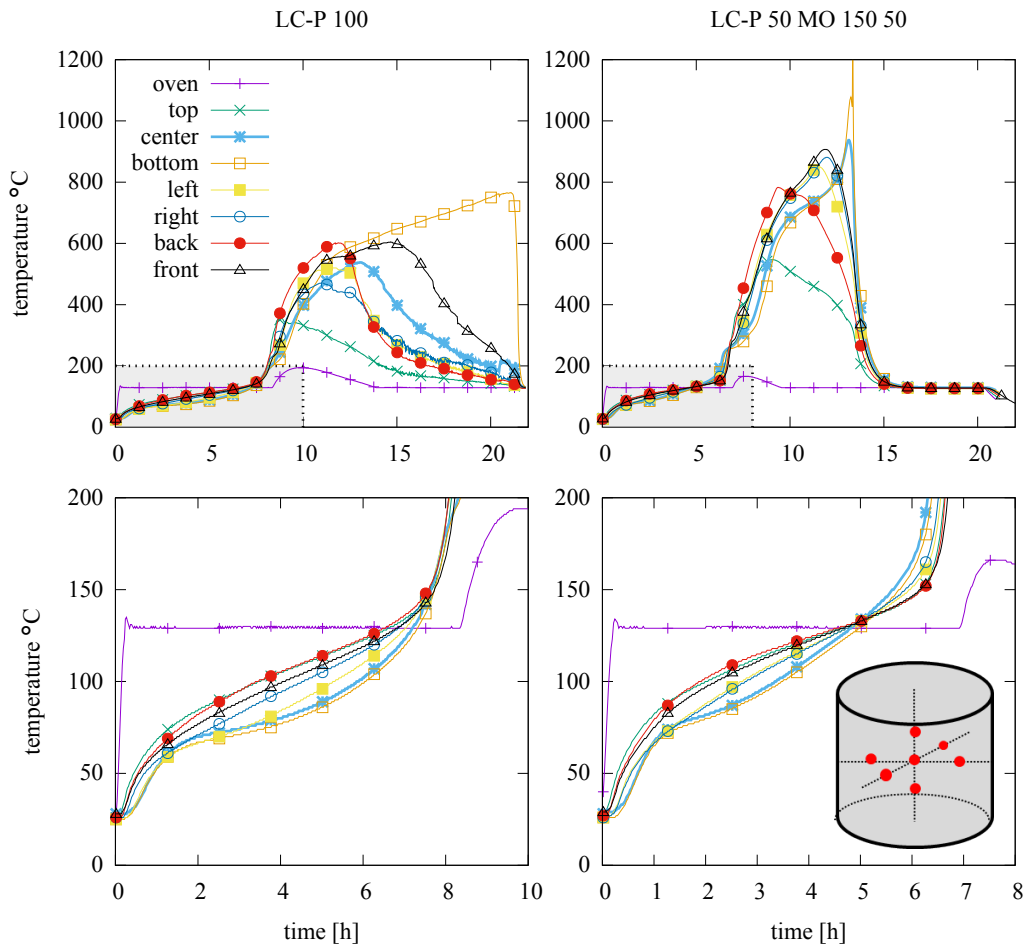


Figure 5.7.: Time-temperature curves of an isoperibolic hot-storage experiment with multiple thermocouples located at  $\frac{r}{2}$  in the xy-plane and at  $\frac{1}{4}$ ,  $\frac{1}{2}$  and  $\frac{3}{4}$  height along the central z-axis (see insert bottom right);  $V = 1600 \text{ cm}^3$  at  $T_{oven} = 130 \text{ }^\circ\text{C}$ . The lower parts show magnifications of the shaded areas in the plots of the upper line. [46]

Since the center thermocouple was not within the embers in the pure lignite experiments, further experiments with additional thermocouples were carried out. To get an idea about temperature evolution in the whole sample, multiple thermocouples were installed. Figure 5.7 shows the temperature evolution with time of pure LC-P and LC-P with 50 % MO150 admixture. The temperature was measured at  $\frac{r}{2}$  in xy-plane and at  $\frac{1}{4}, \frac{1}{2}$  (front, back, left, right) and  $\frac{3}{4}$  height along the central z-axis (bottom, center, top), as shown in the bottom right corner in the figure. A  $1600 \text{ cm}^3$  basket was chosen to obtain a significant distance between the thermocouples. The oven temperature was chosen slightly above the  $T_{SI}$  of the mixture. The experiment was started with a cold oven, since the placement of the multiple thermocouples was very difficult in a preheated oven.

The heating of the mixture was faster, due to the lower  $c_p$  of magnesium oxide. Furthermore, the temperature started increasing first at the top while the bottom heated up later. The difference between top and bottom heating can be explained by spontaneous air flows driven by density differences. Cold air sank down within the sample while warm air was sucked in the top of the sample. Therefore, the top heats up faster while the bottom was cooled due to sinking cold gas. The maximum temperature difference between top and bottom thermocouple for the heating up process was 28 K for LC-P and 25 K for 50 wt% MO150, at 4.5 respectively 2.5 h. The delay in reaching  $90^\circ\text{C}$  respectively  $100^\circ\text{C}$  was approximately 2.7 h for pure lignite and 1.6 h for the mixture.

A second noticeable fact is that the temperature in pure lignite accomplished its maximum at the bottom thermocouple while the other temperatures were decreasing. A reasonable interpretation is that shrinking of the fuel within the sample shifted the reaction zone to the bottom. The other thermocouples were heated due to radiation and convection only. Since the standard measurement method according to DIN EN 15188 is a center thermocouple only, the maximum temperatures of the glowing embers might be underestimated. The 50 wt% MO150 mixture kept its size during the combustion process. All thermocouples remained inside the sample, and were therefore not exposed to ambient conditions. The maximum temperatures were recorded by the center and bottom thermocouple simultaneously. As already shown in figure 5.5, the maximum temperatures are significantly higher for the mixture compared

with the pure material. The peak temperature above  $1200^{\circ}\text{C}$  might be a measurement error, since it is represented by one data point only. The maximum temperature was more likely around  $1050^{\circ}\text{C}$ , the maximum temperature, that was represented by multiple data points.

### Summary

The self-ignition and combustion behavior of pure lignite coal and coal in mixtures with inert materials of different particle size and surface area were investigated in isoperibolic hot-storage experiments. As shown in BAM Research Report 291 [3], the addition of inert material increases  $T_{SI}$  but also the maximum combustion temperature. A maximum occurs for approximately 50 % mixtures by weight. A comparison of particles with different particle-size distributions and specific surface areas has shown that this effect is affected mainly by the particle size. The surface area of the particles had no verifiable impact.

## 5.2. Adiabatic hot storage

This section presents the results of adiabatic hot storage. To get further information about the charrification, the lignite coal was used both as delivered and thermally treated (tt) (see chapter 3.1).

### Untreated material

In total, 27 adiabatic tests were conducted for pure LC-P and 50 wt% mixtures with S063 and MO150. The experiments had at an onset temperature of  $103^{\circ}\text{C}$  in a  $100\text{ cm}^3$  basket.

Figure 5.8 shows the Arrhenius plots of lignite-inert mixtures during adiabatic testing. The algorithm described in 2.3.2 was used. The length of the fitted line was 10 % of the input data tuples. The fitted lines are shown bold. Due to experimental uncertainties, a mean curve from all curves with identical conditions would not be useful. Therefore, all the curves are shown. Each

substance is shown as a line, that is shifted in parallel. This results in a comparable increase and, therefore, activation energy, and a shifted y intercept and, therefore, pre-exponential factor.

The activation energies are  $98.4 \pm 4, 0 \text{ kJ/mol}$  for pure LC-P,  $93.5 \pm 6.2 \text{ kJ/mol}$  for 50 wt% of MO150 and  $90.2 \pm 7.7 \text{ kJ/mol}$  for 50 wt% of S063. The pre-exponential factor was determined as  $1.8 \cdot 10^7 \text{ 1/s}$  for pure LC-P,  $1.9 \cdot 10^6 \text{ 1/s}$  for 50 % wt. of MO150 and  $1.32 \cdot 10^6 \text{ 1/s}$  for 50 % wt. of S063. The average pre-exponential factor is  $3.6 \cdot 10^6 \text{ 1/s}$ . The average length of the fitted lines is 229 data tuples, which corresponds 114.5 min. The lines were fitted over a temperature interval between 381 K and 443 K. The values of the activation energy are approximately 15 % below the values from isoperibolic hot-storage experiments. This difference can be explained from different starting temperatures. Adiabatic experiments start at a temperature below  $T_{SI}$ , therefore the influence of reactions, that start below  $T_{SI}$ , have more influence and were not overridden by a fast temperature rise. [48]

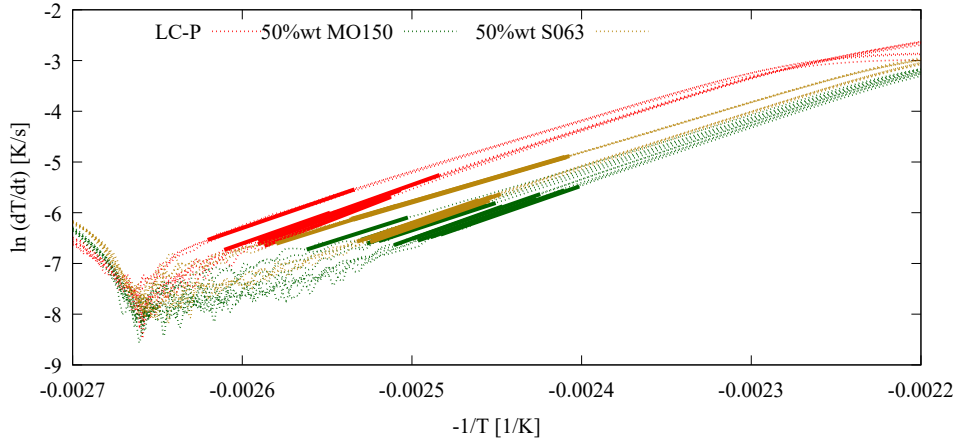


Figure 5.8.: Arrheniusplot of adiabatic hot storage experiments of different lignite-inert mixtures; fitted lines are shown bold.  $T_{onset} = 103 \text{ }^\circ\text{C}$ ,  $V_{basket} = 100 \text{ cm}^3$

## Thermally treated material

The thermally treated (tt) LC-P (see chapter 3.1) was filled in a basket with volume  $100 \text{ cm}^3$ . Since no self-ignition temperature or onset temperature was known, on beforehand an onset temperature of  $120 \text{ }^\circ\text{C}$  was chosen, and step-wise increased. This is similar to a heat-wait-search-algorithm for shortening



the experiment, but the temperature increase was done manually. An exothermic reaction started at  $190^{\circ}\text{C}$  and was followed adiabatically. The initial mass was  $m_{start} = 82.83\text{ g}$ . The temperature curve is shown in figure 5.9. An activation energy of  $165\text{ kJ/mol}$  and a pre-exponential factor of  $5 \cdot 10^7\text{ 1/s}$  could be determined.

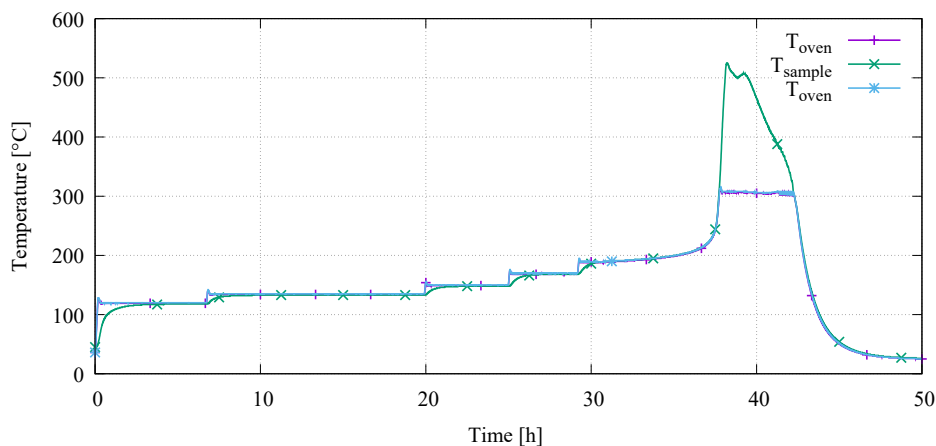


Figure 5.9.: Adiabatic temperature-time curve of thermally treated  $LC - P_{tt}$ , onset temperature  $190^{\circ}\text{C}$

### 5.3. Hot storage and FTIR

In this section the results of the FTIR-coupled hot-storage experiments are shown. The experiments took place in the Sedex oven (see section 4.1). The FTIR is shown and explained in section 4.4.

In total, eight experiments with pure LC-P and six experiments with 50 wt% S063 admixtures were conducted, (see figure 5.10). From these 14 experiments, ten could be evaluated, due to partial data loss or an failure in the oven control. A  $100\text{ cm}^3$  wired mesh basket was used. The oven temperature was set to  $150^{\circ}\text{C}$ . The bulk density was  $710 \pm 3\text{ kg/m}^3$  for LC-P and  $943 \pm 4\text{ kg/m}^3$  for the 50 %wt S063 mixture. The residues of the pure lignite were  $13.1 \pm 0.2\text{ kg/m}^3$  and  $18.6 \pm 2.7\text{ kg/m}^3$  for the 50 %wt S063 mixture. The pure lignite leaves less ash and, therefore, burns more completely than the lignite-silica mixture, but especially the silica mixtures tend to fall out of the sample basket during the test as well as during the transfer between oven and scale. This is also reflected

in the higher standard derivation. Taking into account the loss on ignition of the silica, the value of  $18.6 \text{ kg/m}^3$  decreases to  $15,6 \text{ kg/m}^3$ .

In figure 5.10, the concentrations of all gas species as functions of time are shown. Note the significant increase after ignition at 2.5 h. The high concentration of water was due to the drying process and the ambient humidity. The significant concentration of the  $CO_2$  is partly due to oxidation but also due to the dilution unit and the following multiplication. As stated in section 4.4, the flue gas is diluted by factor 100 to reduce contamination of the FTIR cell. Since the FTIR is calibrated for  $CO_2$  in vol%, the noise in the measured signal is multiplied by 100 and then smoothed as a result of the averaging over experiments. The  $CO/CO_2$  ratio shows a trough at 4.9 h, which can be found in the CO signal as well, but not for  $H_2O$  and  $CO_2$  concentrations. A similar trough is observable in the DSC signal (see figure 5.12) at  $300^\circ C$  and low heating rates. It is assumed that this point (4.9 h) marks the transition from predominantly volatile reactions to char reaction. This is supported by the fact that the methane concentration drops to nearly zero after 4.9 h. Furthermore, it is observable that the  $CO/CO_2$  ratio of the mixture with 50 wt% inert material is much lower, which indicates a more complete reaction.

To compare the different reactions and to derive chemical equations, the area under the curves were numerically integrated using the *trapz* command in Matlab. Since especially the  $CO_2$  signal tends to develop a trend, a baseline between concentration at the start and at the end was calculated. The area beneath this line was subtracted (see figure A.2).

The corrected signal was integrated in total, and before and after 4.9 h. The values derived from the integration were normalized to the smallest value (almost always Methane) to increase comparability in between the experiments. The results are shown in table A.1 and used to establish the reaction equations in section 6.5.

### 5.4. Pipe experiments

Figure 5.11 shows the results of the pipe experiments and reflect the propagation of the reaction front. A peak in the temperature signal indicates that the reaction front is passing a thermocouple. Since times and distances are known,

## 5. Experimental results

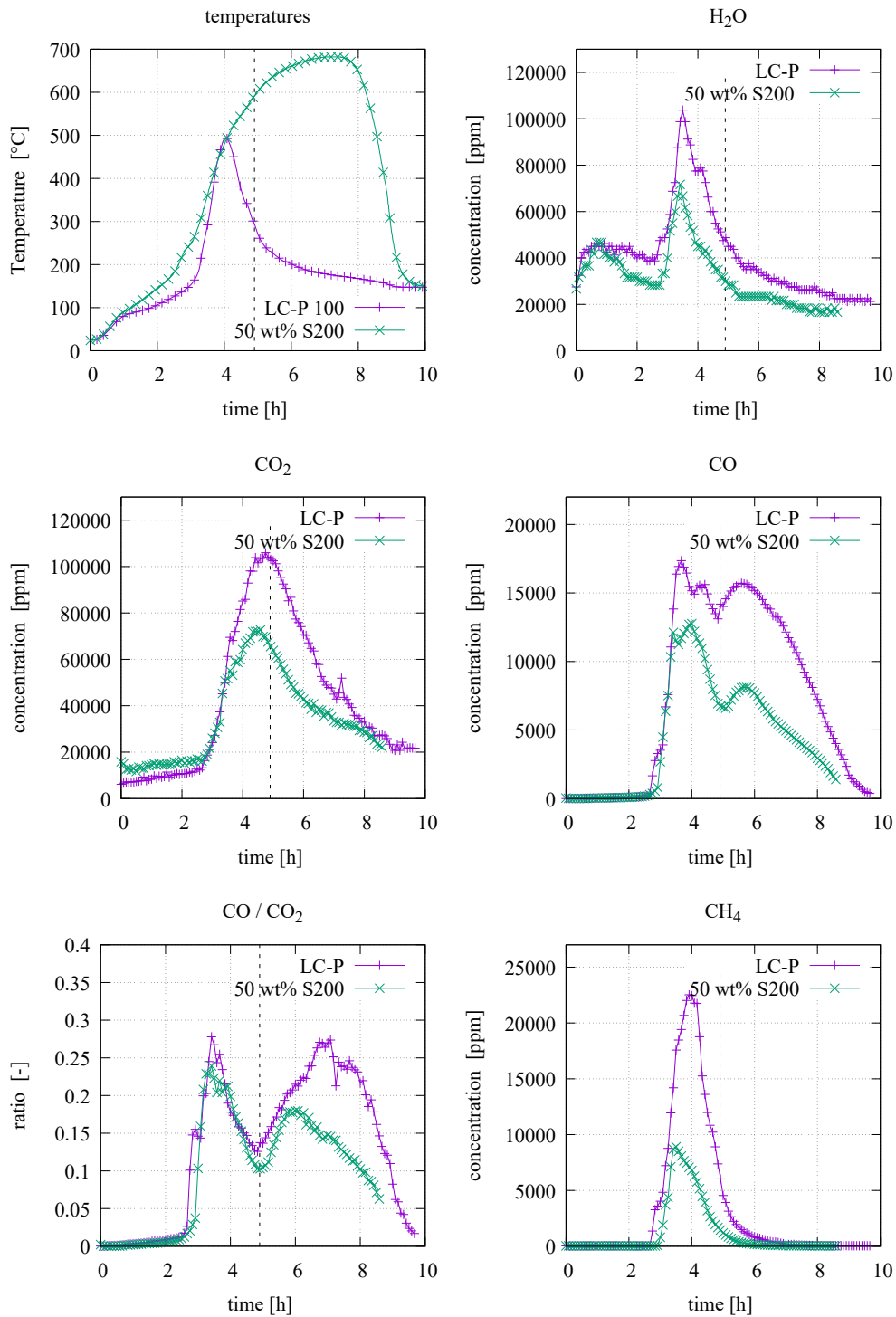


Figure 5.10.: Averaged temperature and concentration profiles of 5 isoperibolic hot-storage experiments for each substance in the Sedex oven coupled with FTIR,  $T_{oven} = 150\text{ }^{\circ}\text{C}$ ,  $V_{sample} = 100\text{ cm}^3$ , dashed line shows local minimum in  $CO/CO_2$  ratio at 4.9 h

the speed of the reaction front can be calculated. The smoldering front spreads within the pure lignite with an average velocity of  $2\text{ mm/h}$ , while the smoldering front inside of the LC-P with a 50 wt% S063 admixture spreads twice as fast. Furthermore, the maximum temperatures of the mixture containing inert material are more than 100 K lower in pure lignite.

In these experiments, the oxygen supply is limited by the flush rate. During the whole experiment, the same amount of air is supplied to the reaction zone whether inert material is added or not. Therefore, the energy release is limited by the oxygen flow rate, which remains constant. [46]

The reaction front spreads twice as fast for the mixture since only 50 % of the oxygen is consumed per volume due to the inert material. In case of a pure combustible, the reaction front will move from one fuel particle to the other. Since downstream of the reaction front oxygen concentration drops to a very low level, no combustion is possible there (see figure ??). The second particle undergoes combustion only after the first one finished and, therefore, oxygen is available. If 50 wt% of the particles are non-combustible the reaction front will pass these particles and therefore propagate faster.

Furthermore, the inert material reduces the calorific value per volume of the bulk material, while the heat dissipation through the outer surface (wall of the cylinder) and heat loss due to the convection of hot gasses remains constant. This results in the lower reaction temperature.

### 5.5. Simultaneous-thermal analysis (STA)

To verify the results of the hot-storage experiments, the samples were also investigated by STA. Figure 5.12 shows the results of the analysis. The data show a mass loss between ambient and  $130\text{ }^\circ\text{C}$  that can be ascribed to water evaporation. Negative heat flow (endothermic reaction) and no emission of  $\text{CO}_2$  and  $\text{CO}$  are also indications that no combustion occurs. After that, the combustion reaction starts at temperatures of approximately  $180\text{ }^\circ\text{C}$ . Gas emissions increase and the DSC signal shows a significant exothermic peak. Depending on the heating rate, and therefore the duration of the experiment, the reaction will stop in between  $400\text{ }^\circ\text{C}$  and  $625\text{ }^\circ\text{C}$ . Since the FTIR was not

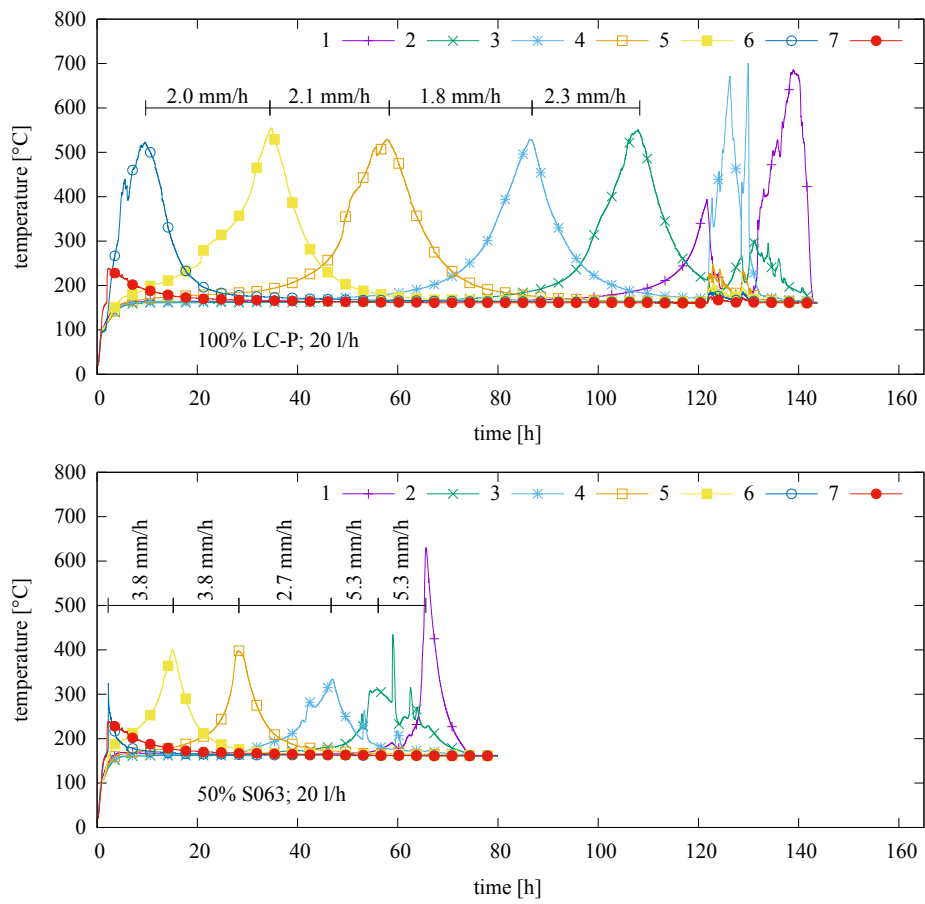


Figure 5.11.: Propagation of reaction front in the pipe experiments for pure lignite (top) and lignite with 50 wt% S63 (bottom), at an oven temperature of 150 °C

available for all STA experiments, only one could be conducted for each heating rate.

The  $1\text{ K}/\text{min}$  and  $2\text{ K}/\text{min}$  experiments showed two peaks at the DSC signal around  $300\text{ }^\circ\text{C}$ , while these two peaks are not visible in the faster experiments. These two peaks are too small to be evaluated. Therefore an experiment with  $0.25\text{ K}/\text{min}$  was conducted between  $150\text{ }^\circ\text{C}$  and  $500\text{ }^\circ\text{C}$ , only. But even this very slow experiment deliver no useful data. Since coal is a composition of different substances, this is not surprising.

The heat released in the main peak was for all experiments in between  $1.21\text{ kJ/g}$  and  $1.39\text{ kJ/g}$ , with a mean of  $1.32\text{ kJ/g}$ . Since this value is calculated from the heat flow as a function of time signal, the heat flow as a function of temperature curves shown in figure 5.12 are misleading. The pre-exponential factor and apparent activation energy calculated according to equation 4.2 in section 4.3 are shown in table 5.2. On average, a pre-exponential factor of  $3.2 \cdot 10^{13}\text{ 1/s}$  and an apparent activation energy of  $118.3\text{ kJ/mol}$  could be determined.

Table 5.2.: Pre-exponential factor  $k_0$  and apparent activation energy  $E_a$  obtained from DSC experiments using the TG signal.

heat rate [ $\text{K}/\text{min}$ ]	1	2	2	5	5	10
$k_0 \cdot 1 \cdot 10^{13} [\frac{1}{\text{s}}]$	1.99	6.35	7.67	0.003	3.56	0.004
$E_a [\text{kJ/mol}]$	118.2	121.8	122.6	105.5	136.4	105.01

As already mentioned in chapter 4.3, the method of Ozawa could not be used, since it would then be necessary to determine exact peak temperatures in the DSC signal. This was not possible because even at low heating rates, no clear peak could be seen. With plateaus covering several hundred Kelvin, the application of this method would be similar to guessing. The peak in the DSC signal is an indication of the maximum rate of reaction. Instead the CO signal can be used, which has clear peaks without plateaus and thus allows further analysis. Here, peak temperatures of  $291\text{ }^\circ\text{C}$ ,  $311\text{ }^\circ\text{C}$ ,  $325\text{ }^\circ\text{C}$  and  $348\text{ }^\circ\text{C}$  can be extracted from the data. With formula 4.1, an apparent activation energy of  $115.7\text{ kJ/mol}$  is obtained.

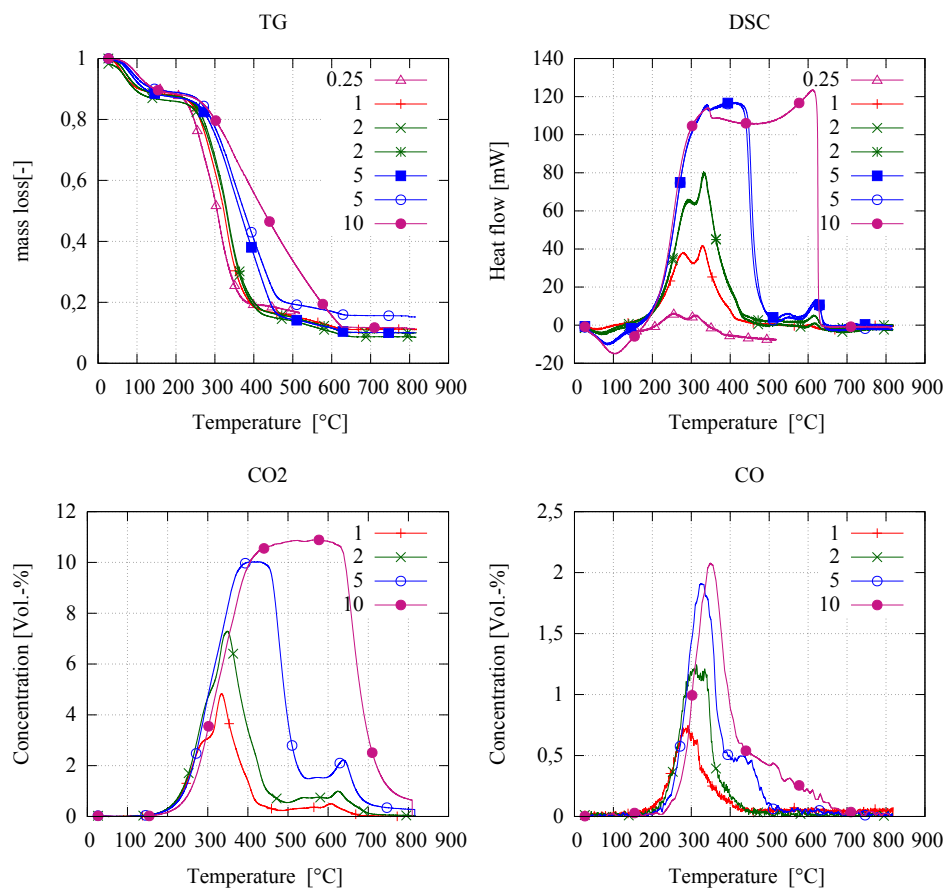


Figure 5.12.: FTIR coupled STA measurements of Lignite (LC-P) with different heating rates as given in the legend in  $K/min$ . The sample mass was from 19.88 mg to 21.35 mg.

## 5.6. Summary and discussion of calculated formal kinetic data

Considering the values obtained for the apparent activation energy, the isoperibolic method ( $110 \text{ kJ/mol}$ ), the TG method ( $118.3 \text{ kJ/mol}$ ) and the Ozawa-Flynn-Wall method based on the CO signal ( $115.7 \text{ kJ/mol}$ ) give comparable results. The adiabatic method leads to an average of  $90.4 \text{ kJ/mol}$ , a value approximately 15 % below the results from the other methods.

The value of the pre-exponential factor from the adiabatic tests ( $7.0 \cdot 10^6 \text{ 1/s}$ ) is orders of magnitude lower than the isoperibolic ( $1.1 \cdot 10^9 \text{ 1/s}$ ) and the TG ( $3.2 \cdot 10^{13} \text{ 1/s}$ ) experiments.

Calculating  $k_{arr}$  according to equation 6.12, the rate of reaction based on these data is calculated. This is shown in figure A.7. It can be seen that these data lead to large differences especially for the data derived from the TG signal, that is due to the high difference of the pre-exponential factor. Comparing the values at  $800 \text{ }^\circ\text{C}$  for the data calculated from isoperibolic experiments, a rate of reaction of ( $2.78 \cdot 10^2 \text{ 1/s}$ ) could be calculated. For the adiabatic data, ( $4.68 \cdot 10^3 \text{ 1/s}$ ) and for the TG experiments ( $5.7 \cdot 10^7 \text{ 1/s}$ ).

The TG results are outliers due to the high pre-exponential factor of ( $3.2 \cdot 10^{13} \text{ 1/s}$ ). However, considering at the pre-exponential factors of the experimental series, the  $5 \text{ K/min}$  and  $10 \text{ K/min}$  experiments (table 5.2), show a pre-exponential factor that is lower by a factor of 1000. Taking the lower value into account the reaction rate at  $800 \text{ }^\circ\text{C}$  drops to  $5.45 \cdot 10^4 \text{ 1/s}$ .

It can be concluded that several experimental procedures should be used when calculating formal kinetic parameters in order to obtain reliable results.

The adiabatic results were based on 27 experiments in total. Therefore, strong influence from outliers can be excluded. Half of the experiments for each sample took place in different ovens with different thermocouples. There is no influence of the oven and the thermocouples, and they can be excluded as sources of error. There might be errors in the algorithm used to evaluate the data. As stated in section 2.3.2, the code filters the fitted lines after their coefficient of determination. Lines with a coefficient below 99.9% of the best line were not taken into account. Reducing this factor to 99 % or 90 % increases the averaged



activation energy to  $99.5 \text{ kJ/mol}$  respectively  $149 \text{ kJ/mol}$ . In figure 5.8, the line is shifted to the left, into the steeper but more noisy part.

A value of 95% for the coefficient of determination gives for the apparent activation energy  $184 \pm 63 \text{ kJ/mol}$  for pure LC-P,  $113 \pm 36 \text{ kJ/mol}$  for 50 wt% of MO150 and  $113 \pm 25 \text{ kJ/mol}$  for 50 wt% of S063. Due to the noisy regions, these values show a standard deviation that is 10 times higher than the lines in the smooth regions. Anyhow, if the purpose is to obtain values that are comparable to the results from other methods, the more noisy part have to be chosen. If the purpose is to search for a smooth line, that is statistically more reliable, a higher factor has to be chosen.

The higher reaction temperatures of the mixtures can be ascribed to the increased porosity and, therefore, permeability. As suggested in figure 5.6, fine, inert particles may build a supporting structure. This structure keeps the sample in position and prevents movement of the coal particles during combustion. On the one hand, the surface of the bulk remains unchanged. Decreasing mass during combustion, combined with a constant volume due to the stabilization of the inert material, increases porosity and therefore permeability. The increased permeability causes a better gas exchange and oxygen supply and therefore reaction velocity. Furthermore, the heat conductivity is reduced due to the increased amount of air. On the other hand, more heat is discharged due to convection.

Within the forced flow experiments, lower reaction temperatures for bulk material with inert components occur. There is no visual evidence for a supporting structure as seen in the basket experiments. The pipe containing the sample was full metal, and removing it from the oven inevitably led to shaking, as a result the structure of the bulk was destroyed. However, there is no obvious reason that no supporting structure would have been formed. Taking this into account, it can be concluded that the type of convection has direct influence on the maximum reaction temperatures.

The effects described above will be investigated by numerical simulation in the following chapter.

## 6. Simulation

Numerical simulations may extend experiments, which can usually be carried out on a laboratory scale, only, due to limitations in laboratory resources. Simulations may allow an extrapolation to the technical scale. Complex geometries and boundary conditions can be considered. Smoldering and self-ignition experiments at the technical scale are very time consuming due to large induction times and are therefore not practicable. A numerical approach provides a solution fast. The possibility for obtaining more detailed information about the process, such as temperature and gas concentration distributions, constitute further advantages of numerical simulations. The numerical simulation program COMSOL Multiphysics® (hereafter COMSOL), was used within this thesis. COMSOL is a software platform offering numerical solvers and models for a variety of problems in continuum physics. A model in this context is based on the principles of fluid mechanics, utilizing numerical methods and algorithms [49]. Coupling different models (Multiphysics) and solving them simultaneously is a main advantage of COMSOL. Models are usually solved with FEM (finite element method). FVM (finite-volume method) and particle-tracing methods are only available in a few sub-models and are not considered within this thesis. Different direct and iterative solvers are offered.

Within the following sections a short overview over FEM is given, the used model is explained and the results of the simulation are shown. Furthermore, this sections presents a detailed model description.

### 6.1. Finite Element Method (FEM)

Within this section, a brief overview over FEM is given. Detailed explanations can be found in [50], [51] and [52].

Finite Element Method is a general numerical method that can be used to make calculations for problems in continuum physics, and is mainly used in structural analysis, heat transfer and fluid flow. These boundary-value problems are solved using partial differential equations. FEM divides larger problems into smaller parts that are called finite elements. These finite elements are usually cuboids or tetrahedrons. The behavior of these finite elements is calculated using a hat (triangular) equation. [53] The function value of these equations is one at exactly one point, whereas it is zero for all other points. This function is multiplied by weighted residues for calculating the desired function that incorporates the partial differential equations and the boundary conditions. [54]

In FEM, the unknown functional relationship of the investigated physical quantity, like temperature or concentration, is approximated by an approach function (linear, higher order) between the neighboring nodes.

## 6.2. The developed COMSOL Model

This section gives a brief overview over previous models as well as the model developed within this work. The COMSOL report comprising the exact equations and boundary conditions is depicted [55]. For the simulation within this thesis, COMSOL was used in Version 5.3a Build: 229. The simulation was carried out on a computer with two Intel Xeon E5649 CPU's at 2.56 GHz with 6 physical cores each. The motherboard was a Supermicro X8DA3 with 48 GB DDR3 RAM. Windows 7 Professional 64 bit was used as operating system. A simulation needed between 20 and 100 hours. When time step size remained below  $10^{-4}s/timestep$ , it seems that the result contains invalid solutions and the calculation was aborted.

### 6.2.1. Objectives and strategy of the numerical investigation

The experiments indicate that the high reaction temperatures in mixtures of combustible and inert particles reflect convection and conduction processes within combustible porous media. This should be investigated deeper with numerical simulations. The aim is the examination of fluid flow and heat transfer

through the porous media. Thereby it is mainly focused on the adaption of the permeability.

Since COMSOL can deal with fixed solid structures only, the collapse of the bulk cannot be part of the model. Therefore, mixtures with 50 wt.% inert material are a perfect for modeling. As the experiments showed, remain in shape throughout the smoldering process (see figure 5.6).

The combustible material is consumed due to the reaction. In the case of pure lignite the sample collapses. Since shrinking material cannot be simulated, it is assumed that the permeability remains unchanged when the pure coal particles shrink uniformly. The permeability is not changed with fuel concentration. In case of 50 wt.% inert material, on the one hand, the sample volume is unchanged, and pores are formed. In this case permeability is modeled as dependent on the fuel concentration.

Basically, three simulations were conducted. Within one of them, the permeability was not changed during the combustion process. This simulation represents the combustion of a pure combustible without of inert material. Within the other two simulations, permeability was increased with decreasing combustible concentration. These simulations were supposed to represent inert combustible mixtures. In one of these two simulations, permeability was increased to a value that represents the 50 % mixture with inert material (100 % permeability adaption), the second simulation was done with half of that value (50 % permeability adaption) to have an intermediate case. This behavior is mapped by the variable *factor\_permeab* which is used to switch between the three cases, whereby 0 means no permeability adaption and 1 means permeability adaption. The permeability adaption is described in chapter 6.3.2

The experiments took place in two different ovens. While the hot storage experiments took place in an oven purged by natural convection, the FTIR measurements took place in the SEDEX, which was mechanically ventilated. This oven had well-defined boundary conditions for the inlet because air was supplied via flow meter.

To limit the necessary number of simulations the following compromise was made: The flow in the modeled oven was driven by natural convection but the inlet mass flow was controlled. No mechanical ventilation took place. The size of the oven was like the SEDEX as the influence of the reaction products

and, therefore, the dilution of oxygen should be taken into account. For the experiments in both ovens  $100\text{ cm}^3$  samples were used, among others. This sample size was used as initial value for the simulation.

Depending on the measured  $CO/CO_2$  ratios, there are two reaction equations formulated. These take into account that, when the oxygen concentration is higher, combustion is more complete and, therefore, heat release is larger.

### 6.2.2. Previous work and developed model

The model used in this work is based on the work Krause, Schmidt, Lohrer and Ferrero carried out between 2005 and 2010 at BAM in Berlin [56], [57], [41], [6], [3]. All models were implemented in COMSOL (formerly FEMLAB) and solve heat, mass and species transfer within a given 2D or 3D geometry. The reaction rate is modeled with an Arrhenius equation whereupon source terms for heat and species are calculated. While earlier models consider diffusive heat and mass transfer only, the models published in [41] and [3] consider a gas flow within the porous media only, calculated using Darcy's equation. All models solve only a porous matrix, so to say the sample. Boundary conditions could be dependent on time or temperature, but have to be defined beforehand. Interactions with the surroundings, e.g. the inertisation due to combustion products or the heating up within a hot storage oven could not be included. The used models kept material properties like heat conductivity, diffusion coefficients, permeability constant. Within these models the porous medium is treated as fixed, as the porous medium does not move. When fuel is consumed voids will emerge. These cavities can be found in experiments, too, but usually they will collapse later during the burn away.

The model within this work, calculates with fixed solid structures for all three cases. As shown in figure 5.6, mixtures with high amounts of magnesium oxide did not collapse. In this case, one would assume, that the model fits the experiments well. In the other hand, for pure lignite larger differences between model and experiments are to be expected, due to the non-modeled shrinkage of the sample.

The two main improvements of the model presented here compared to previous work are, on the one hand, the surroundings that are now part of the model.

The boundary conditions are defined at the oven inlet and outlet, instead at the outside of the sample. Furthermore, material properties like permeability and porosity change with time respectively temperature or fuel concentration.

Putting a boundary condition on the sample surface keeps it's conditions constant. Several conditions cannot be taken into account. The temperature of the sample surface depends on time and position since the combustion changes the oven temperature. Furthermore, the concentration of exhaust gas and ambient changes over time and space. At last, there are different functionalities of the sample boundaries. For example, the top surface of the sample will be an inlet during heating up while it becomes an outlet during combustion. The side walls will be inlet and outlet at the same time. These effects cannot be calculated exactly when boundary conditions were constant.

For the simulation within this thesis, version 5.3a of COMSOL was used. This version is fundamentally revised since the simulations in the publications mentioned in section 6.2.2 were conducted. Therefore, new toolboxes were available and a new model had to be 'constructed'. COMSOL is a modular software in which the user can pick from a variety of modules that can be combined. Depending on the task, the appropriate tools have to be chosen. The model, used for the current simulations, consists of the following model options, that will be briefly described within this section.

- Brinkmann equations interface (br)
- Transport of Concentrated Species interface (tcs)
- Reactive Flow coupling (rf)
- Heat Transfer in Porous Medium (ht)
- domain ODE's (ode)

Considering different flow regimes, COMSOL has options as shown in figure 6.1. It shows the governing equations in a riverbank. Since Navier-Stokes and, therefore, Brinkmann, Darcy and Richards equation are valid for all fluids, this can be transferred into the problem described within this thesis. The water in the figure represents the air. Regions with fluid only are simulated with the help of Navier-Stokes equation. Saturated flow regions can be simulated by Darcy or Brinkmann equations, while unsaturated flow is described by Richards equations.

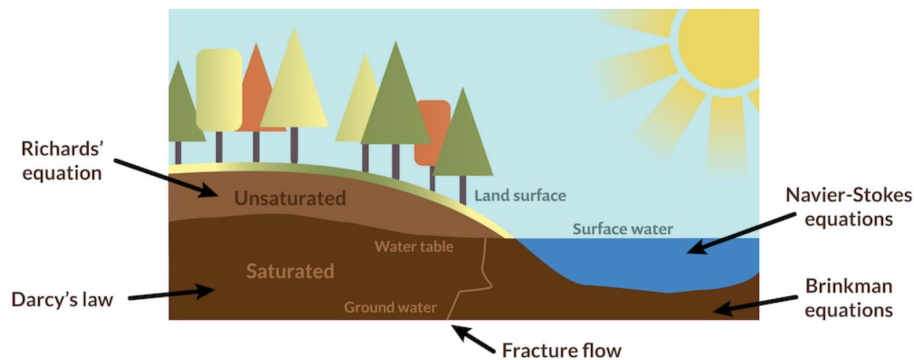


Figure 6.1.: Cross-sectional view of a riverbank and the governing equations applied to each flow regime. [58]

Peter Lyu gives in an official COMSOL MULTIPHYSICS BLOG a summary of the COMSOL Handbook: The subsurface flow [...] is typically described by the Brinkman equations. The Brinkman equations account for fast-moving fluids in porous media with the kinetic potential from fluid velocity, pressure, and gravity driving the flow. These equations extend Darcy's law to describe the dissipation of the kinetic energy by viscous shear, similar to the Navier-Stokes equations. Therefore, the Brinkman equations interface is well suited for modeling fast flow in porous media, including transitions between slow flow in porous media governed by Darcy's law and fast flow in channels described by the Navier-Stokes equations. The Brinkman equations interface computes both the velocity and pressure. [58] [55]

Baer [32] states that Darcy's law is valid for Reynolds number smaller than 1, in some cases smaller than 10. For our case, velocities of maximum  $0.04\text{m/s}$  could be determined from simulation. Depending on temperature, and therefore, dynamic viscosity and chosen particle diameter, Reynolds numbers between 850 and 8000 were obtained for the cases considered in the thesis.

Consequently, the Brinkmann equations Toolbox ( abbreviated *br*) with activated fluid region was used.

To model the species transport the Transport of Concentrated Species ( abbreviated *tcs*) toolbox is used. According to the COMSOL Users's guide, this toolbox is suitable for studying gaseous and liquid mixtures where the species concentrations are of the same order of magnitude and none of the species can be identified as a solvent. In this case, properties of the mixture depend on the composition, and the molecular and ionic interactions between all species need

to be considered. The physics interface includes models for multicomponent diffusion, whose diffusive driving force of each species depends on the mixture composition, temperature, and pressure. This interface can be used to model the evolution of distributions of chemical species transported by convection and diffusion. [55]

In order to ensure that Brinkman and the Transport of concentrated species toolbox are coupled, the reacting flow coupling feature was enabled. The Reacting Flow coupling synchronizes the features from a [...] Brinkman equations interface and a Transport of Concentrated Species interface. When added, the density in the [Brinkmann] interface is automatically synchronized to the one defined by the Transport of Concentrated Species interface. Conversely, the velocity field used by the latter interface is synchronized to the one computed in the former interface [55].

For modeling the heat transfer, the Heat Transfer in Porous Media interface (ht) was chosen. It is used to model heat transfer by conduction and convection in porous media. All functionalities for including other domain types, such as a solid or fluid domains, are also available. The temperature equation, defined in porous media domains, corresponds to the convection-diffusion equation with thermodynamic properties averaging values to account for both solid matrix and fluid properties. This equation is valid when the temperatures within the porous matrix and the fluid are in equilibrium [55]. To simplify the model and to reduce calculation time, radiation is only considered between the oven walls and the sample surface, not within the porous medium.

### 6.2.3. Mathematical description

At each point of the model geometry, the temperature field, and the concentration fields of seven species,  $O_2$ ,  $N_2$ ,  $CO_2$ ,  $CO$ ,  $CH_4$ , fuel, and char, were solved. While the gaseous products were treated as a fluid, the solid reactands are kept immobile. Solid-to-solid reactions are not considered

The following assumptions were made:

- gasses are ideal
- there are no forces applied to the solid bulk material
- diffusion coefficients depend on temperature and porosity only



- the bulk material is homogeneous and isotropic at  $t=0$ , properties change with fuel concentration.
- no influence of moisture
- no influence of the particle size distribution
- radiation between oven and porous surface only

Equation 6.1 gives the heat transfer equation that has to be solved. This equation is solved using properties of the solid and species-averaged fluid properties. The first term represents the heat accumulation in the system, the second term the heat transfer due to convection, and the third the heat transfer due to conduction. These three term have to equal the output from the heat source (right-hand side term). Variables with the subscript *eff* are effective variables which means values are valid for the porous medium, not for the solid or the fluid phase, only. The effective variables  $(\rho c_p)_{eff}$  and  $\lambda_{eff}$  are calculated according to equation 6.2 and 6.3 using a porosity weighted average of solid and fluid properties.

$$(\rho c_p)_{eff} \frac{\partial T}{\partial t} + \rho c_p u \cdot \nabla T + \nabla \cdot (-\lambda_{eff} \nabla T) = Q_{sc} \quad (6.1)$$

$$(\rho c_p)_{eff} = (1 - \phi) \rho_p c_{p,p} + \phi \rho_{fl} c_{p,fl} \quad (6.2)$$

$$\lambda_{eff} = (1 - \phi) \lambda_p + \phi \lambda_{fl} \quad (6.3)$$

with

$\rho$	$\left[\frac{kg}{m^3}\right]$	density
$c_p$	$\left[\frac{J}{kg \cdot K}\right]$	heat capacity
$T$	$[K]$	temperature
$t$	$[s]$	time
$u$	$\left[\frac{m}{s}\right]$	velocity / velocity field
$\lambda$	$\left[\frac{W}{m \cdot K}\right]$	heat conductivity
$Q_{sc}$	$[W]$	heat source
$\phi$	$[-]$	porosity
$fl, fluid$	$-$	fluid
$p$	$-$	solid particle

Equation 6.4 is the Navier-Stokes-Brinkman (NSB) equation used to solve momentum both in the porous medium and in the free-flow region. This equation is solved using species-averaged fluid properties.

The term in the square brackets is the Navier Stokes equation (with  $\phi = 1$ ) that is used in the free-flow region.  $I$ , the unit vector, is used to exclude the nabla operator  $\nabla$ . The free-flow region is without a source of mass in the fluid domain ( $\frac{\partial \rho}{\partial t} + \nabla \cdot (\rho u) = 0$ ).

The term in the round brackets is the Brinkmann part of the NSB equation, that is additionally solved in the porous media to take permeability and a mass source into account. The term  $\rho g$  is the gravitational volume force to consider buoyancy. Equation 6.5 gives the source term describing the generation of gaseous species during the reaction of the solid component, and is defined in the porous medium only.

$$\rho \frac{\partial u}{\partial t} = \nabla \cdot \left[ -pI + \mu \frac{1}{\phi} (\nabla u + (\nabla u)^T) - \frac{2}{3} \mu \frac{1}{\phi} (\nabla \cdot u) I \right] - \left( \mu \kappa^{-1} + \frac{Q_{br}}{\phi_p^2} \right) u + \rho g \quad (6.4)$$

$$\frac{\partial \phi \rho}{\partial t} + \nabla \cdot (\rho u) = Q_{br} \quad (6.5)$$

with

$\rho$	$\left[ \frac{kg}{m^3} \right]$	density
$u$	$\left[ \frac{m}{s} \right]$	velocity / velocity field
$t$	$[s]$	time
$p$	$[Pa]$	pressure
$I$	$[-]$	unit vector
$\mu$	$[Pas]$	dynamic viscosity
$\phi$	$[-]$	porosity
$\kappa$	$[m^2]$	permeability
$Q_{br}$	$\left[ \frac{kg}{m^3 \cdot s} \right]$	mass source

Equation 6.6 gives the transport of each species, due to diffusion. For each species one set of equations is solved. The first term gives the species change over time, the second the species transport due to diffusion, and the last due to convection.  $R_{species-i}$  is the source term. The sum of all  $R_{species-i}$  results in  $Q_{br}$  in equation 6.5.  $j_i$  is the diffusional flux magnitude that is calculated using

Fick's law and an additional term to take the molar mass into account, since heavy molecules diffuse slower.

$$\begin{aligned} \phi \rho \frac{\partial \omega_i}{\partial t} + \nabla \cdot j_i + \rho(u \cdot \nabla)\omega_i &= R_{species-i} \\ j_i &= - \left( \rho D_i^m \nabla \omega_i + \rho \omega_i D_i^m \frac{\nabla M_n}{M_n} \right) \\ D_i^m &= \frac{1 - \omega_i}{\sum_{k \neq i} \frac{x_k}{D_{jk}}} \quad ; \quad M_n = \left( \sum_i \frac{\omega_i}{M_i} \right)^{-1} \end{aligned} \quad (6.6)$$

with

$\rho$	$\left[ \frac{kg}{m^3} \right]$	density
$\omega_i$	$[-]$	mass fraction of species i
$t$	$[s]$	time
$j_i$	$\left[ \frac{kg}{m^2 \cdot s} \right]$	diffusion flux density of species i
$u$	$\left[ \frac{m}{s} \right]$	velocity / velocity field
$R_{species_i}$	$\left[ \frac{kg}{m^3 \cdot s} \right]$	source term of species i
$D_i^m$	$\left[ \frac{m^2}{s} \right]$	diffusion coefficient after Maxwell Stefan of species i
$M_n$	$\left[ \frac{mol}{m^3} \right]$	mass-fraction-averaged molar mass
$x_k$	$[-]$	mole fraction of species i
$D_{jk}$	$\left[ \frac{m^2}{s} \right]$	diffusion coefficient of species j in species k
$M_i$	$\left[ \frac{mol}{m^3} \right]$	molar mass of species i

#### 6.2.4. Geometry and Mesh

The following chapter explains the geometry used for simulation including the mesh used to solve the equations, the mesh quality and the results of the mesh convergence calculation.

#### Geometry

To reduce computational time, a 2D model was used (figure 6.2 (a)). The disadvantage of the 2D modeling is the lower agreement with the experiment. All information that is connected to variations with depth are lost. The geometry was 40.3 cm in x and 38.0 cm in y direction. 36 mm x 10 mm long squares were removed to model in and outlet. The sample was 50 mm x 50 mm and placed in

the center of the oven. A sample container was not modeled. It can be assumed that the container do not influence on the effects that are simulated. Additionally, due to the small dimensions of the metal wire, the sample container would have made meshing much more complex.

### Mesh

An unstructured triangular mesh was chosen. It was refined at the in- and outlet, the walls and the porous sample. Within the bulk material, the maximum element size was set to 2.55 mm and the element growth rate to 1.05. The element growth rate is defined as the fraction of the volume of neighboring cells. Within the free-flow region, the maximum element size was set to 12 mm at a growth rate of 1.13. The inlet was refined with 10 mesh elements (3.6 mm per element) and the walls where refined with 60 elements each (ca. 6.6 mm per element). The mesh used in the simulations is shown in figure 6.2 (b). Figure 6.2 (c) displays a mesh that was coarser within the sample than the one shown in figure 6.2 (b). This is for better visualization since the actually used mesh could not be visualized without further zooming.

Figure 6.2 (d) shows the most important quality parameters for the mesh. The definitions according to the Comsol Users Guide [55] are given below. The mesh element quality is a dimensionless value between 0 and 1, where 1 represents a perfectly regular element, in the chosen quality measure, and 0 represents a degenerated element.

It should be mentioned that bad meshing will result in convergence problems that might lead to the solver running out of it's limits, which leads to a reduced accuracy of the simulation results up to the termination of the simulation.

The number of cells directly influences the required computation time for the problem. The user has to decide which cell size leads to a reasonable accuracy. In order to minimize the calculation time, the cells are enlarged in peripheral areas. The transition between the different cell sizes and properties must be smooth in order to maintain the quality parameters.

The quality of the majority of cells is above 0.6 for skewness and growth rate and above 0.9 for volume vs. circumradius and length (see figure 6.2 (d) ). It

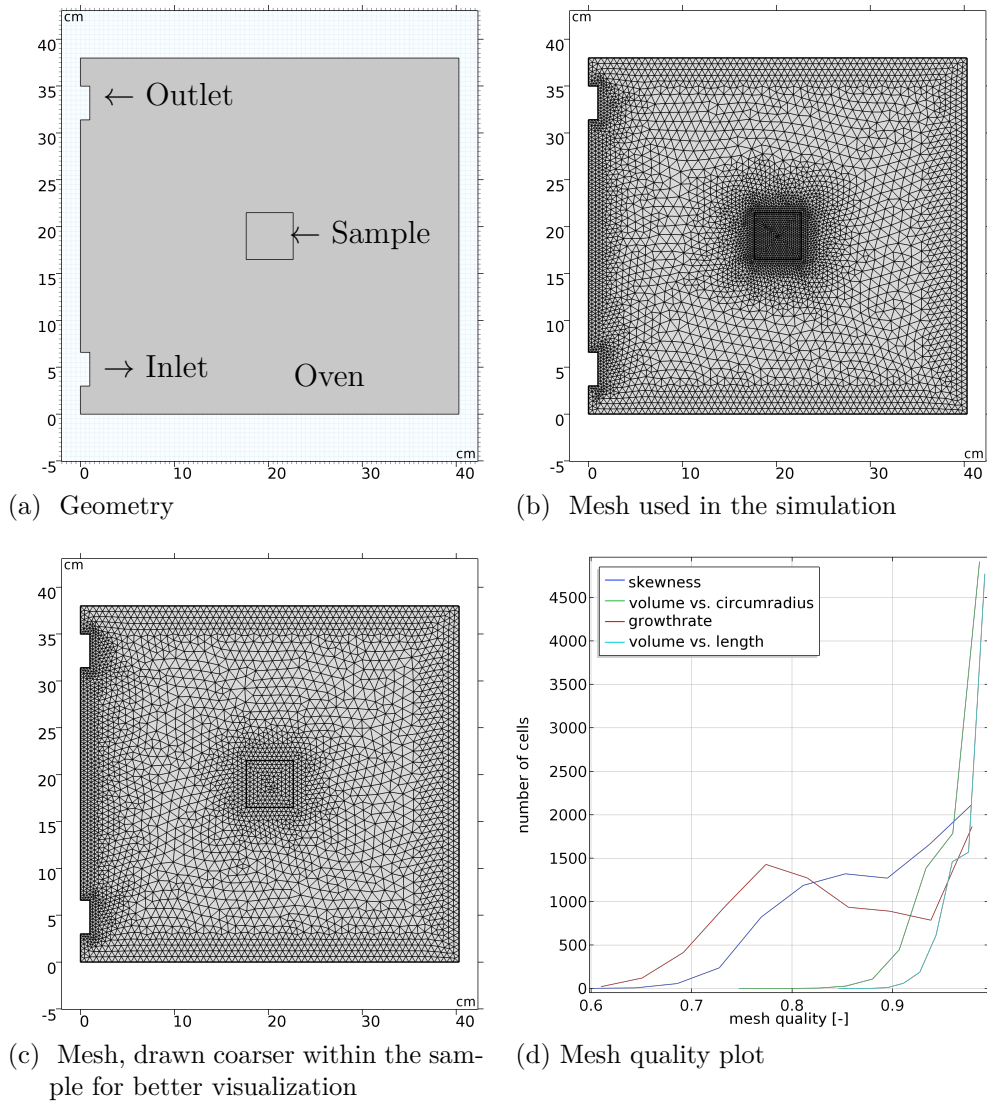


Figure 6.2.: Geometry used for simulation with the generated and mesh quality

can be concluded that the computational grid generated here is suitable for the calculation and will lead to reliable results.

**skewness** The skewness, which is based on the mesh elements' equiangular skew.

**volume versus circumradius** The volume versus circumradius, which is the default quality measure, is based on the ratios of the inscribed and circumscribed circles' or spheres' radii for the simplex corresponding to each corner of the element. If the simplex cannot be clearly determined (an apex of the pyramid, for example), the corresponding corner is excluded from the consideration.

**volume versus length** The volume versus length, which is based on the ratio of element edge lengths and element volume. This quality measure is primarily sensitive to anisotropy.

**growth rate** The growth rate, which is based on the mesh elements' local (anisotropic) growth rate.

Figure 6.3 examples of perfect cell arrangement and a degenerated sketch for the quality criteria skewness and growth rate. A zero volume variation and skewness will result in an accurate solution, while a steep volume variation or an increased skewness will decrease accuracy.

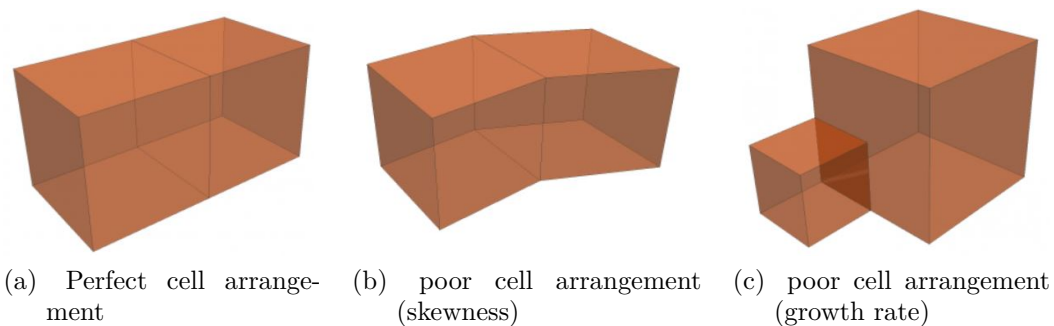


Figure 6.3.: Examples of good good cell arrangement and poor examples for skewness and growth rate [59]

## Mesh convergence

Ideally, a mesh convergence analysis should be performed in order to estimate the accuracy of a simulation. This means that the mesh should be made twice as fine in each spatial direction and the simulation carried out once again on the refined mesh. If the change in critical solution parameters for the original mesh and the finer mesh is within the required tolerance, the solution can be regarded as being mesh-converged. For practical reasons, it is seldom possible to make the mesh twice as fine in each direction. Instead, some critical regions can be identified and the mesh is refined only there [55]. Since the used model geometry is quite small it was possible to refine the whole mesh. The temperature and oxygen concentration of the sample center, as obtained with a coarse and with a fine mesh, are shown in figure 6.4 left part. These two values and the position were chosen since they are essential for comparing simulations and experiments. It is obvious that the curves are close as demonstrated in the right part of the figure, which shows the difference in results with the two meshes. Therefore, the coarser mesh was used for the simulation.

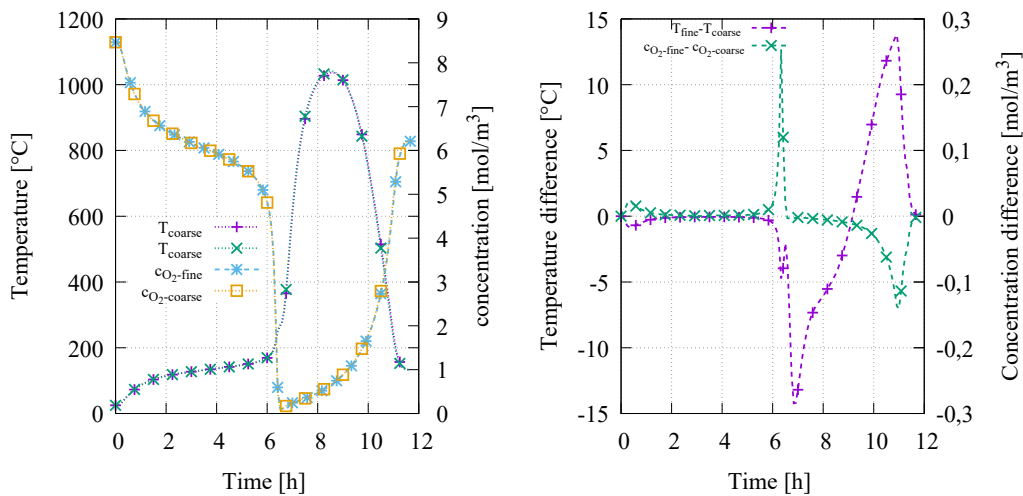


Figure 6.4.: Temperature and oxygen concentration for the used mesh (coarse) and a mesh twice as fine.

## 6.3. Definitions and initial values

### 6.3.1. Boundary conditions and initial values

This subsection gives an overview over the initial conditions and the boundary conditions of the model.

Concerning the fluid movement, the velocity at the walls was set to 0 ( $u=0$ ). The boundary condition was 'no slip'. The inlet mass flow was set to  $1.2\text{ g}/\text{min}$ . This flow rate was set at the mass-flow meter used to control the inlet flow at the SEDEX oven. The initial and outflow pressure was set to  $101325\text{ Pa}$ , the pressure under standard conditions. Backflow was suppressed. Initial values for the velocity was  $u=0$ , as the fluid in the oven is supposed to be nearly at rest in the initial time step.

The initial species concentration was set to 23 wt.% oxygen, which was also the value for the inlet concentration. This value is the average of oxygen. The initial nitrogen concentration was calculated by the system as 77 wt.%. Minor components like argon were neglected, since it can be assumed that they behave inert like nitrogen.

The temperature of the oven atmosphere was initially set to  $130^\circ\text{C}$ . The boundary condition at the walls, as well as the inlet temperature was set to  $130^\circ\text{C}$ . Within the experiments, an oven temperature of  $130^\circ\text{C}$  ensured an ignition in all cases, while not being too far from self-ignition temperature. The initial sample temperature was set to  $25^\circ\text{C}$ , the average laboratory temperature.

The initial coal mass was assumed to be  $60.5\text{ g}$  in the  $100\text{ cm}^3$  basket, the initial average coal mass in an experiment. Concentration was calculated according to equation 6.7. In the simulation runs with inert material this value was reduced accordingly.

$$c_{\text{coal\_start}} = \frac{60.5\text{g}}{M_{\text{fuel}} \cdot V_{\text{basket}}} \quad (6.7)$$

To account for variations in concentration coal concentration and mass during combustion, a normalized ramp is calculated. The name of this COMSOL



functionality is *int* (interpolation). This function is defined for maximum mass as 0, and for a mass of 0 (sample completely burned) as 1.

The maximum mass is defined by the starting concentration and the molar mass of the fuel molecule. ( $c_{coal\_start} * 163[g/mol]$ ). Since the modeling of the reaction is in two steps, the char concentration has to be taken into account as well. Therefore, the values in between are calculated, considering the concentration and molar mass of the char, using the equation  $c_{coal} * 163[g/mol] + c_{carbon} * 48[g/mol]$ . The molar masses result from the apparent fuel molecules.

### 6.3.2. Material definitions

This section provides relevant definitions, used in the present thesis, of material properties and their dependencies.

#### General definitions

The material defined in the oven is named air, the sample material is named bulk. The material settings for the air are taken from the COMSOL library and remain unchanged except the density value. Since in an very early model an pressure error occurred, the density calculation was changed from the pre-defined one to:  $\rho_{air} = \frac{p}{R_{air} \cdot T}$  with  $R_{air}$  of  $287 J/kg \cdot K$ , which was used in all later models.

The mass and the volume before and after every experiment were measured, therefore, the porosity and density could be calculated. As an average of all experiments the porosity was calculated as 0.58 and 0.85 while the density could be estimated with  $700 kg/m^3$  to  $370 kg/m^3$ . These values where calculated in the simuations according to the actual coal concentration in each cell.

The heat capacity of coal was measured to  $1200 J/kg \cdot K$ . The values for magnesium oxide ( $932 J/kg \cdot K$ ) and silica ( $1051 J/kg \cdot K$ ) were taken from the data sheets of the manufacturer. Since these substances have comparable  $c_p$  values, the heat capacity was ramped to  $932 J/kg \cdot K$ . The adaption of heat capacity described above was switched off for the simulation with pure lignite.

## Permeability

The permeability was measured at ambient temperature in virgin fuel as described in chapter 3.2.3. For LC-P, a value of  $2.4 \cdot 10^{-8} m^2$  was determined. The permeability value at lower flow rates was chosen, since it is more representative for the flow in a porous medium.

$$\kappa = C \frac{\phi^{2+\tau}}{(1-\phi)^2} \quad (6.8)$$

Costa [60] published equation 6.8 for dependency of the permeability on porosity  $\phi$  and tortuosity  $\tau$ . The tortuosity is a property of a porous medium and reflects the twists of the flow. According to Costa, the parameter is between 1 and 4. In the simulations, the median value  $\tau = 2.5$  was used.

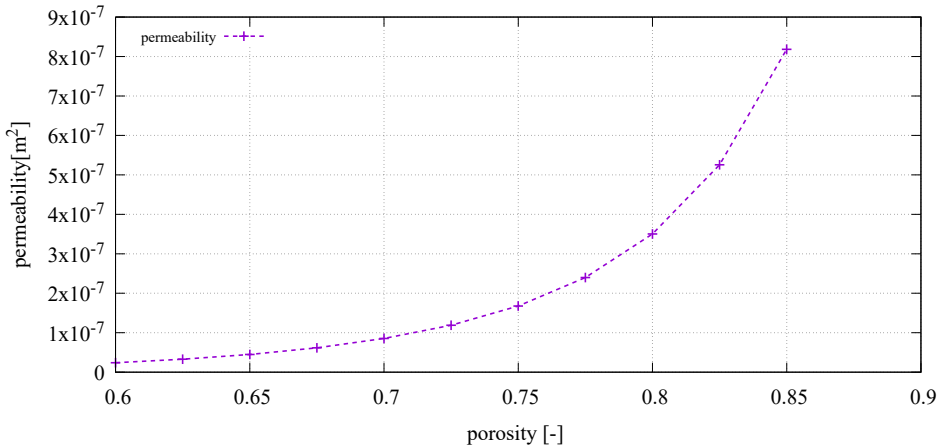


Figure 6.5.: Calculated permeability-positivity relationship according to equation 6.8

From the experiments, a permeability of  $2.4 \cdot 10^{-8} m^2$  at a porosity of 0.6 was determined at ambient conditions. From these values the constant  $C$  in equation 6.8 could be determined as  $8.23 \cdot 10^{-8} m^2$ . Using this equation, permeability as function of porosity could be computed as shown in figure 6.5.

The factor  $factor\_permeab$  is a value between 0 and 1 that leads to a change in permeability during the simulation. For a factor of  $factor\_permeab=0$  the permeability stays constant at the value of  $permeab\_start$ . For a factor of  $factor\_permeab=1$  the value is changed according to equation 6.8. For simulations, values of  $factor\_permeab$  between 0 and 1 are possible, as well.

## Diffusion coefficients

Müller [61] published diffusion coefficients for several gasses in 1968. The binary diffusion coefficients for nitrogen ( $0.178 \text{ cm}^2/\text{s}$ ), oxygen ( $0.180 \text{ cm}^2/\text{s}$ ) and carbon monoxide ( $0.178 \text{ cm}^2/\text{s}$ ) in air were published for 273.2 K. Note that the parameter is almost the same for all three species. A overall diffusion coefficient  $D_0$  of  $0.18 \text{ cm}^2/\text{s}$  is therefore assumed. The temperature dependence can be calculated according to equation 6.9 using the parameter  $Z$  that for all three species is 1.67.

$$D_{temp} = D_0 \left( \frac{T}{T_0} \right)^Z \quad (6.9)$$

Marshall [62] (see equation 6.10) improved the model of Penman [63] to calculate porosity-dependent diffusion coefficients.

$$D_{poros} = D_0 \cdot \phi^{3/2} \quad (6.10)$$

Substituting for  $D_0$  in equation 6.9 with  $D_{poros}$  from 6.10 leads to equation 6.11 which expresses the temperature and porosity dependence in one equation.

$$D_{jk} = D_0 \phi^{3/2} \left( \frac{T}{T_0} \right)^Z \quad (6.11)$$

## 6.4. Combustion modeling

### 6.4.1. Reaction rate

To calculate the reaction rate, two different mechanisms have to be taken into account. Firstly, the reaction rate depends directly on temperature, as calculated using an Arrhenius approach. Secondly, the reaction rate depends on the mass transfer rate of the oxygen molecules to the reactive sites at the coal particle surfaces. Here diffusion is the limiting mechanism. At low temperatures, the reaction is mainly dominated by the Arrhenius law, while at high temperatures the limitation due to diffusion has to be taken into account when modeling reaction kinetics. Diffusion limits the mass flow of gasses close

to the particle, in particular the mass flow of oxygen and the gaseous reaction products. Modeling this, microscopic data, like the partial pressure of oxygen at the particle surface and the diffusion coefficient along the particle surface, are needed [64].

Main problem is that the diffusion coefficients within pores and at the surface are hard to measure, and literature data is quite vague and valid only for specific substance. The pore diffusion coefficient of different ores, that are comparable to lignite, published by Specht [64], is in between  $10^{-2} m^2/s$  and  $10^{-5} m^2/s$ . The range of these values reflects the imprecision of the data that can be obtained from literature.

Bal and Rein stated in their work about complexity in pyrolysis, that for high level of complexity, the prediction accuracy is controlled by the input parameter uncertainty [65], [66]. Therefore, the effects described above are not part of this thesis. First, building a more complex model, based on less reliable data, will not lead to better results. Second, it is challenging to obtain precise and reliable material properties for these parameters.

The rate of reaction was calculated using the Arrhenius equation (Eq. 6.12). Input values for the pre-exponential factor  $k_0$  and the activation energy  $E_A$  based on the isoperibolic values, that can be found in section 5.1.1. The diffusion-limited rate is referred to as  $k_D$ . The two rates are combined in equation 6.14, which is widely used for cases like parallel connected resistors.

In order to get an approximation of the limiting factor  $k_D$ , the model was run without a diffusion limitation factor at all. The reaction rate coefficient was solely calculated from equation 6.12. As a result, the reaction front became unrealistically hot (thousands of Kelvin within a few square mm) and, therefore, time steps became very small (below  $10^{-4} s/timestep$ ). For the last time step with plausible temperature results,  $k_{arrh}$  was evaluated.

Simulations have shown that the maximum value of  $k_{arrh}$  with realistic temperature results is between  $1^{1/s}$  to  $10^{1/s}$ . This was used as an input for the determination of  $k_D$ . In order to show the dependency of this value, a parametric sweep between 0.1 and 100 was conducted. The results are shown in figure 6.6. In this figure, the center temperature of the sample is shown as the diffusion limitation factor  $k_D$  was varied. As a upper boundary, a simulation

with  $k_D = 100$  was conducted but could not be finished due to convergence problems. It can be concluded, that such large limiting factors could not stabilize the problem. For the further simulations  $k_D = 1$  was chosen.

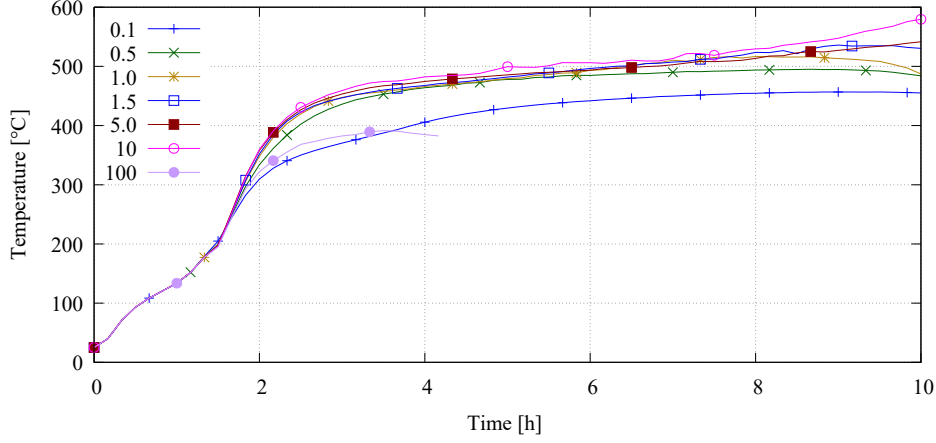


Figure 6.6.: Temperatures in the sample center for different diffusion-limiting factors  $k_D$  without permeability adaption

$$k_{arrh} = k_0 \cdot \exp\left(\frac{-E_A}{R \cdot T}\right) \quad (6.12)$$

$$k_D = 1\left[\frac{1}{s}\right] \quad (6.13)$$

$$k = \left(\frac{k_{arrh} \cdot k_D}{k_{arrh} + k_D}\right) \quad (6.14)$$

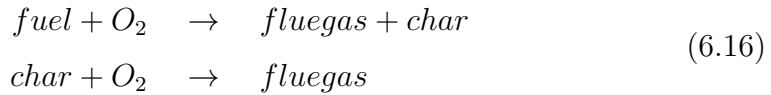
The reaction rate  $r$  was calculated using equation 6.15. The factor  $(c_{fuel} > 10)$  respectively  $(c_{O_2} > 0.1)$  is COMSOL notation for a boolean operation. If the requirement is fulfilled, the output is 1, if not, it is 0. This is used to prevent the solver from calculating negative values. Due to sharp concentration profiles, a cell with a value of nearly zero might become negative within the next time step. Setting the reaction rate to zero, if the fuel concentration is below  $10 \text{ mol}/\text{m}^3$  or the oxygen concentration is below  $1 \text{ mol}/\text{m}^3$ , prevents the solver from running into singularities.

$$r = k \cdot c_{O_2} \cdot (c_{fuel} > 10) \cdot (c_{O_2} > 0.1) \quad (6.15)$$

## 6.5. Combustion reactions and heat of combustion

Since the coal molecule is hard to picture, within this section an apparent fuel molecule is constructed, the reaction equations are formulated and the heat of combustion for each reaction is calculated.

The STA experiments showed two peaks in the DSC signal at low heating rates (see figure 5.12). Considering, furthermore, the sharp peak at the end of the hot storage experiments (figure 5.2), it is hard to explain the behavior with a one-step model, only. As a result, a two step model was chosen, as summarized in equation 6.16. For the fuel, the composition of LC-P was used, whereas the thermally treated version  $LC - P_{tt}$  was used for the char. From the proximate analysis (table 3.4), carbon, hydrogen and oxygen were identified as the main components. Nitrogen and sulfur were neglected due to low values determined in the elemental analysis. Nitrogen and sulfur-containing reaction products are had low concentrations in the FTIR measurements, as well. To keep the model more simple and to save computation time, the apparent fuel components were reduced to C, H and O.



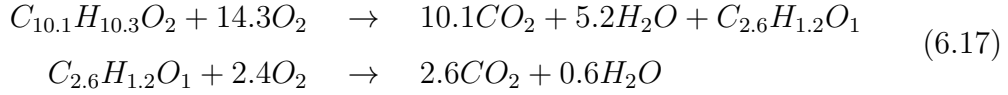
Dividing the mass percentages from the elemental analysis by the molar masses, the molar composition of the fuel was calculated, and normalized to an integer for oxygen. The formula of the fuel then became  $C_{10.1}H_{10.3}O_2$ , the one of the char  $C_{2.6}H_{1.2}O_1$  (see table 6.1). Using integer values for C and H is not recommended, since it will decrease accuracy. These compositions result in molar masses of  $M_{fuel} = 163.8 \text{ g/mol}$  and  $M_{char} = 48.1 \text{ g/mol}$ .

The heat of combustion from the bomb calorimeter measurements cannot be directly used for simulation, since in those measurements combustion took place in a pure oxygen atmosphere and, therefore, the combustion was very complete. To get a realistic calorific value that is valid for smoldering combustion, the heat of reaction for the smoldering case has to be calculated. With this as an aim, the heat of formation of the reactants, fuel and char, has to be

Table 6.1.: Composition of apparent fuel molecule  $n_{ap}$  for  $LC - P$  (fuel) and  $LC - P_{tt}$  (char) based on the water and ash free results of the proximate analysis (see table 3.4)

	$LC - P$ - fuel			$LC - P_{tt}$ - char		
	ratio [%wt.]	n [mol]	$n_{ap}$ [mol]	ratio [%wt.]	n [mol]	$n_{ap}$ [mol]
C	70,6	5,9	10,1	59,8	5,0	2,6
H	6,0	6,0	10,3	2,2	2,2	1,2
O	18,4	1,2	2,0	30,9	1,9	1,0

calculated first. This can be done using the results from the bomb calorimeter and a complete reaction approach (equation 6.17).



The general equation for calculating the standard enthalpy of reaction  $\Delta H_r^\ominus$  is given by formula 6.18.

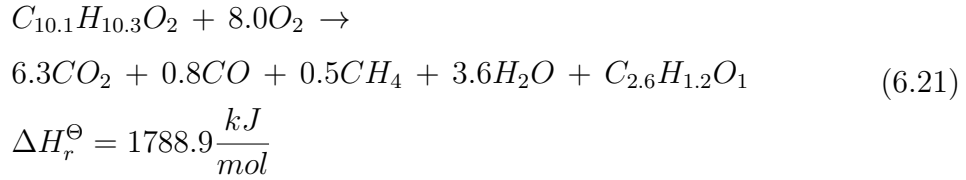
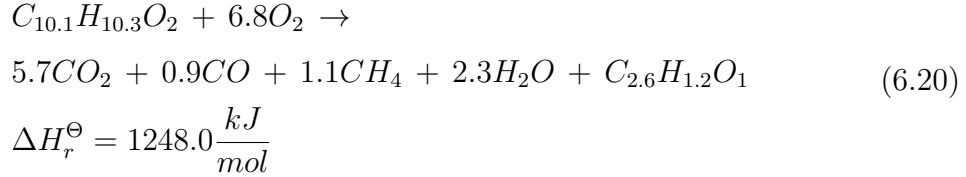
$$\Delta H_r^\ominus = \sum(n \cdot \Delta H_{f\_product}^\ominus) - \sum(n \cdot \Delta H_{f\_reactand}^\ominus) \tag{6.18}$$

The heat of formation for char and fuel can be calculated from equation 6.19. Here, the heat of reaction  $\Delta H_r^\ominus$  equals the lower calorific value (LCV). The calculated enthalpies of formation are given in table A.2. For the fuel, a heat of formation  $H_{f\_fuel} = 2207.5 \text{ kJ/mol}$ , and for the char, a heat of formation  $H_{f\_char} = 507.0 \text{ kJ/mol}$  were calculated.

$$\Delta H_{f\_reactand}^\ominus = - \sum(n \cdot \Delta H_{f\_products\_complete\_reaction}^\ominus) - \Delta H_r^\ominus \tag{6.19}$$

To set up reaction equations for the incomplete combustion reaction of fuel and char, the conducted FTIR measurements were used (figure 5.10). The ratio  $CO_2 : CO : CH_4$  is shown in table A.2. From the values of peak one, before 4.9 h the ratios for the fuel reaction (equation 6.20, 6.21) were determined. From peak two, after 4.9 h (see section 5.3), the ratios for the char reaction (equation 6.22, 6.23) were determined. The origin of the peaks before

and after 4.5 h is explained in section 5.3, see especially figure 5.10. For each substance, a well-oxidated (equation 6.21, 6.23) and a less-oxidated (equation 6.20, 6.22) incomplete combustion equation was formulated. The data for the well-oxidated versions are taken from the 50% inert mixture, the versions for the less-oxidated versions are determined from the pure lignite reactions.



## 6.6. Used COMSOL solver

COMSOL offers two categories of algorithms to solve systems of linear equations. On the one hand, iterative solvers, on the other, direct ones. COMSOL chooses the solver automatically without any input from the user, still it should be checked. For the given problem, two direct solvers were chosen. Pardiso (Parallel Sparse Direct And Multi-Recursive Iterative Linear Solvers) for the velocity and pressure field, respectively, and Mumps (Multifrontal Massively Parallel sparse direct Solver) for the temperature field. Pardiso is a thread-safe, high-performance, robust, memory efficient and easy-to-use software for



solving large sparse symmetric and unsymmetric linear systems of equations on shared-memory and distributed-memory multiprocessors. MUMPS is programmed to solve large linear systems with symmetric positive definite matrices, general symmetric matrices, and general unsymmetric matrices, among other applications. A detailed description can be found in the latest version of the Users Guide of the Pardiso [67] and MUMPS [68] Project published on the corresponding homepages .

The following list from COMSOL Users Guide [55] instructs the user how to find the most suitable solver. Pardiso and Mumps differ in their memory usage and efficiency of parallel computing in clusters, but not in the precision of the solution. The Users Guide gives the guideline below. Since Pardiso and MUMPS work well and give stable results within an acceptable time, the automatically selected solvers were used.

1. Try the PARDISO direct solver.
2. Try the MUMPS direct solver.
3. If the solver still runs out of memory or is too slow, use one of the iterative solvers GMRES, FGMRES, or BiCGStab. Select a preconditioner according to the guidelines in the section about the iterative solver.
4. If the system is positive definite and real symmetric or Hermitian, try the conjugate gradients iterative solver, which is more memory-efficient and sometimes faster than GMRES, FGMRES, and BiCGStab. Select a symmetric preconditioner. Alternatively, try the SPOOLES direct solver. It often uses less memory but is less numerically stable. SPOOLES is also slower.

## 6.7. Results

Basically three simulations were conducted. The initial conditions of the simulation were discussed in chapter 6.3.1. The permeability adaption was explained in chapter 6.3.2. These three simulations were computed, using values of 0, 0.5 and 1 as values for *factor\_permeab*. These values reflect the difference between pure lignite (no permeability adaption), a 50% admixture of inert

material (100 % permeability adaption) and to have a intermediate case, with 50 % permeability adaption.

Figure 6.9 shows the temperature curves for the simulations conducted within this work. The 2D plots with the temperature, oxygen and carbon dioxide profiles are shown in figure 6.8 and in the Appendix (see figure A.3 A.4 and A.5). As described in 6.3.2, the permeability was adapted according to equation 6.8.

Comparing results from temperature measurements with the simulations, the absolute values do not agree very well (see figure 6.7). It can be suggested that this is due to an inadequate combustion model. This is supported by the difference in the simulated gas concentrations compared with the FTIR measurements. A suggestion for improvement is given in the section 8. Nevertheless, behavior observed in the simulations, are comparable with those of the experiments. The higher the inert fraction, which is represented by an increased adjustment of the permeability in the simulation, the larger the temperatures reached and the sooner this temperature peak occurs. Hereinafter, these effects will be discussed.

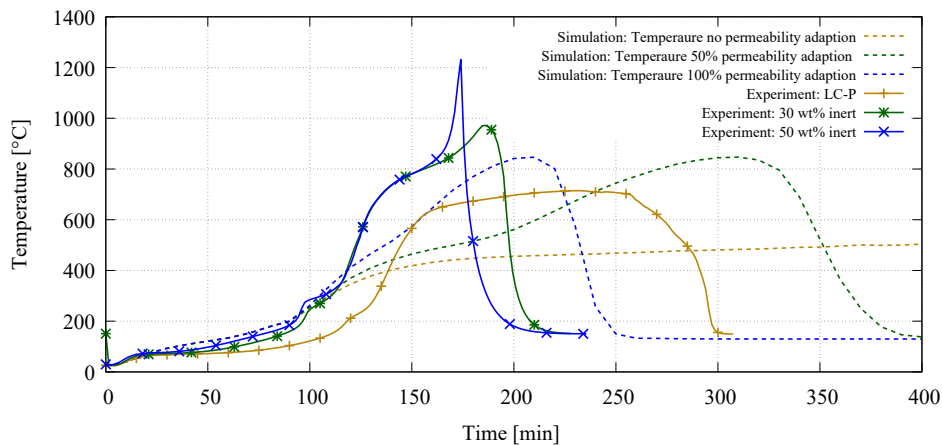


Figure 6.7.: Evolution of temperature in experiments (see figure 5.3) compared to simulated temperature evolution.

The maximum temperature in the simulation without permeability adaption shows a long plateau at approximately  $520^{\circ}\text{C}$ . Since the coal particles are not moving, the reaction moves quite symmetrically inwards in the sample, as shown in the following 2D temperature and gas concentrations plots. The permeability in the burned areas is not adapted, gas and especially oxygen transport is obstructed. Therefore, the reaction rate is limited by oxygen transport

and the heat generation is low. The low temperature in the simulation with no permeability adaption, compared to the experiments, suggests, that the no permeability adaption leads to an unrealistically strong obstruction. Increasing the permeability during combustion allows better gas transport through the bulk. More oxygen is transported into the reaction zone, the reaction rate is increased, temperatures become higher and the peak temperature is reached earlier.

The heat-release rates are similar the first 120 minutes for all three cases. Within this phase heating and ignition take place. The run-away-reaction occurs. After the maximum value, which characterizes the point where oxygen limitation starts, the heat release-rate decreases but to different levels for the three cases. This can be explained by the oxygen supply to the reaction zone. It is the most obstructed with no permeability adaption, therefore, the heat release rate is low in this case. With increased permeability, the oxygen supply increases, and, therefore, so does the heat-release rate.

Figure 6.8 shows the calculated temperature profiles of the three permeability adaption cases at important time steps. Figures of more time steps are shown in appendix figure A.3. At the center, within the black rectangle, the sample is located and combustion occurs. The color code shows the temperature distribution from blue (cold) to red (hot). The sample was heated from ambient to oven temperature with subsequent combustion. The first row, visualizes the last time step where this heating process was not yet fully finished.

Due to the different combustion velocity and combustion time, not all of the plots are shown at comparable time steps. Furthermore, the color code varies in order to ensure better visibility of the effects. The minimum and maximum value of the color code can be seen above and below the key next to the black triangles.

Comparing the temperature profiles, no differences can be seen after heat up and ignition (50 min, 70 min). All simulations show the same temperature profile at the same time. The reaction is limited by temperature (kinetically limited). Permeability adaption has no influence.

The first difference occurs at approximately 100 minutes. While the shape of the temperature profile is similar, the maximum reaction temperatures are different, from  $393\text{ }^{\circ}\text{C}$  (no permeability adaption) to  $470\text{ }^{\circ}\text{C}$  (100% permeability

adaption). As shown in figure 6.9 as well, this is the point at which the reaction becomes limited by oxygen supply in the case of no permeability adaption, while the increased ventilation due to increased permeability leads to a higher rate of combustion and, therefore, energy release and temperature in the other two cases.

The next row shows the temperature profiles at 280 min and 180 min. The case with 100 % permeability adaption at 180 min shows a similar shape and similar values of the temperature profile as 50 % adaption at 280 min. Considering the pure lignite, a rounded reaction zone is visible at rather low temperatures. This is a result of low gas velocities due to low permeability. The temperature profiles are comparable for 50 % and 100 % permeability adaption. They occur at different times, which indicates that the burn off happens faster for 100 % adaption, since the same combustion stage is reached earlier. Regions in which the coal is already burned are shown in blue as they have cooled down to oven temperature.

The temperature profiles in the last row show the final stage of the reaction. All of them are at different time steps, which indicates the overall speed of the combustion. Furthermore, the maximum temperature reaches  $504^{\circ}\text{C}$  for the no-permeability-adaption case,  $812^{\circ}\text{C}$  for the case of 50 % adaption, and  $851^{\circ}\text{C}$  for the 100 % adaption case. The most interesting fact is that the position of the reaction's center is much more shifted upwards due to buoyancy in the cases with permeability adaption.

Another indicator of the increased heat release is the temperature of the oven. Due to the heat release within a shorter time scale, the oven heats up much more at the top in the cases with permeability adaption.

As a final point to extract from the temperature profiles, the differences between the simulations occur after a kinetically-controlled reaction. Due to the lack of oxygen, resulting limited airflow at low permeability, the reaction is transformed into a stoichiometric-limited one.

The oxygen concentration (see figure A.4) is lowered from the beginning of the process. While there is still oxygen available during the self-heating (second row, 70 min), the concentration in the sample drops to nearly zero after ignition occurs at 100 min. From this point on, the combustion in the sample

## 6. Simulation

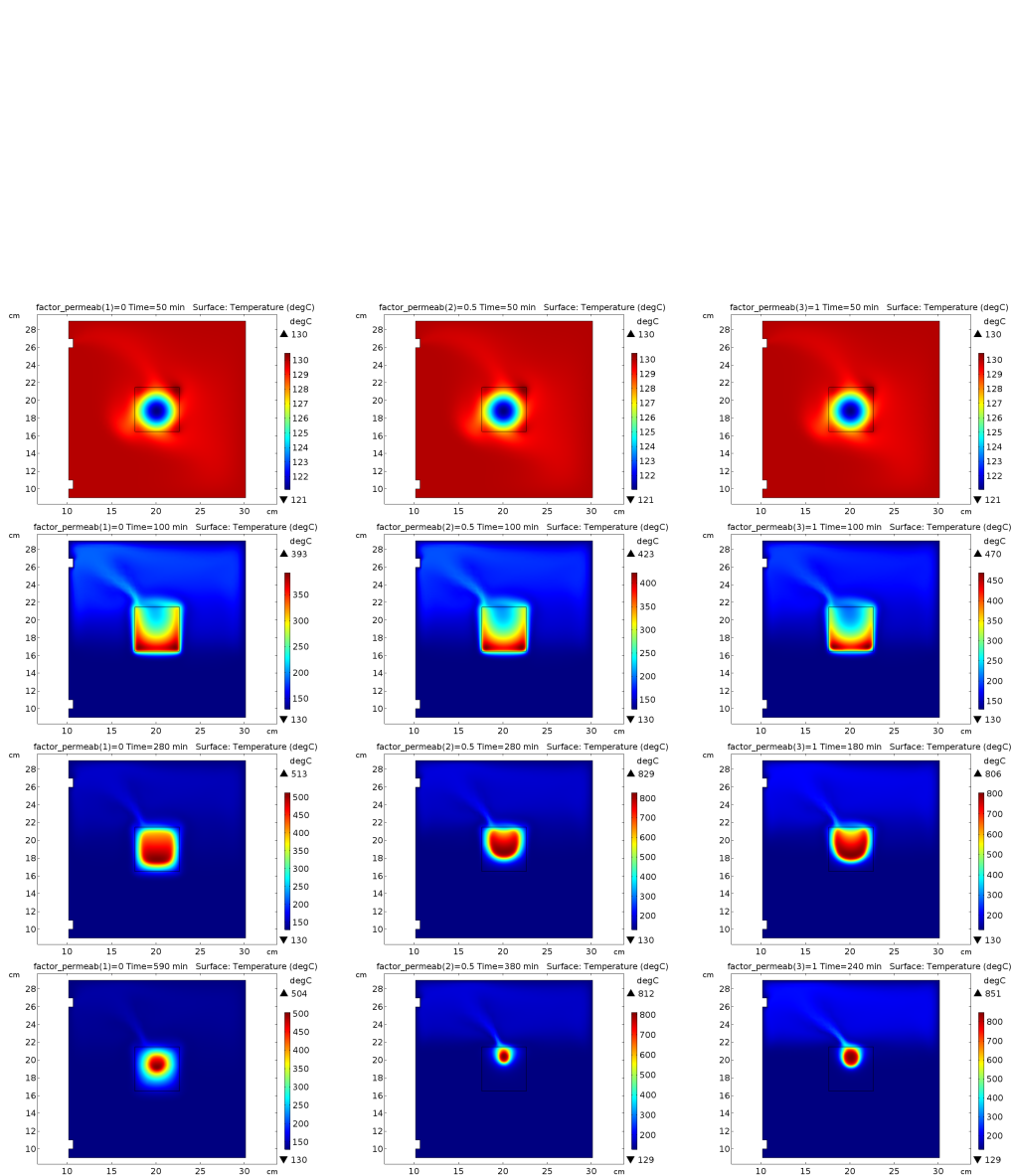


Figure 6.8.: Temperature profiles for no (left column), 50 % (center column) and 100 % (right column) permeability adaption according to equation 6.8 with no reaction adjustment. Attention: different color codes (see bar at the left). Rows: Temperature profiles at different time steps, Figures of more time steps are given in Appendix A.3

is impeded. Reaction is possible at its lower boundary, only, where oxygen is driven in by buoyancy. This can be seen in the temperature profiles, as well.

Furthermore, an inertisation of the oven can be observed. The hot gas layer has oxygen concentrations as low as 10 wt.%, but the sample is not entirely inerted, as the bottom layer, is still in the oxygen rich layer. The burn off of the coal is reflected in the oxygen concentration as well. In the regions, in which no combustion happens, the oxygen concentration is at the initial level of 23 wt.%. The concentration of carbon dioxide, a reaction product, is zero in these regions. After the ignition, the sample is inerted by  $CO_2$ .

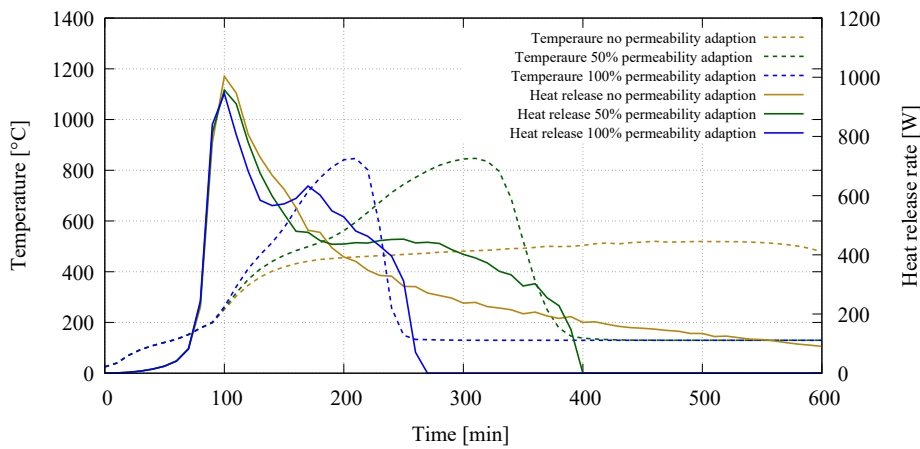


Figure 6.9.: Temperature profiles for different permeability adaptations at  $0.5 \cdot h_{sample}$  in central axis

This can be seen in figure 6.10. The flux of oxygen is plotted as a function of time. Since COMSOL interprets 2D models as 3D models with 1 m depth the value is per  $m^2$ . As oxygen is responsible for the reaction and therefore the heat release, it was chosen for evaluation. For the 50 % and 100 % permeability adaption, the center point was used for the evaluation. In the diagram with no adaption, the point at  $1/4$  sample height was used, because the reaction front did not pass the center until the end the calculated time. The dashed lines at 280 min, 310 min and 210 min, show the time when the reaction front passes the probing point (maximum reaction temperature). To the left of the dashed line, the reaction front is below the probing point, to the right it is above. The time axes are shifted, that these times of maximum temperature are corresponding. For better visibility the y-axis is scaled to  $8E-4 \text{ kg}/m^2 \cdot s$ , but the maximum convective flux is given, at the time it occurs, by an arrow.

For all cases, diffusive transport dominates when the reaction front passes. Coal concentration and, therefore, porosity and permeability are still quite low. As a consequence, convection is limited. Diffusive oxygen transport is the main transport mechanism near the reaction front. Due to the increased permeability, convection becomes significant after the reaction front has passed. This applies from the lower surface of the sample to the reaction front. Therefore, the period in which diffusion limits the mass transport, is in the cases with adaption (middle and lower plot in figure 6.10) much smaller than without adaption (upper plot).

Figure A.6 shows the flux of all species as well as a summed-up signal. Different convective fluxes are in the same direction. During combustion, the fresh air enters from the bottom, while products are transported upwards. Therefore, in- and outflow are not obstructing each other. On the other hand, a diffusive flux usually occurs in all directions, thus in- and outflow are obstructing each other. It can be seen that before the reaction front had passed, diffusive and convective mass transfer show comparable curves. After the reaction front had passed and the burn off took place, convective transport starts to dominate. The maximum flux is approximately 8 times (50% adaption), respectively 10 times (100% adaption), higher compared to the non-adaption case.

Figure 6.12 shows the heat flux in x and y direction for the point at the central axis and at height  $0.25 \cdot h_{sample}$  (first diagram) and  $0.5 \cdot h_{sample}$  (second and third diagram). For the first case of no permeability adaption, a lower height was used, since the reaction front did not move this far up during the simulation. Positive values are for upward respectively right-oriented heat transfer, while negative values are a downwards respectively left-oriented heat transfer. The x-direction (left, right) heat flux due to convection is neglectable, since it is not buoyancy driven. All in all, conduction is neglectable in comparison to heat transfer due to convection.

Within the first minutes, convection is dominant due to the cold air leaving the sample because of to buoyancy. Heat flux is nearly zero as the sample heats up to oven temperature. This process continued until ignition occurred and conduction became dominant since the low permeability did not allow convection. When the material around the probing point had reached the oven temperature, no temperature gradient existed and conduction was reduced to zero.

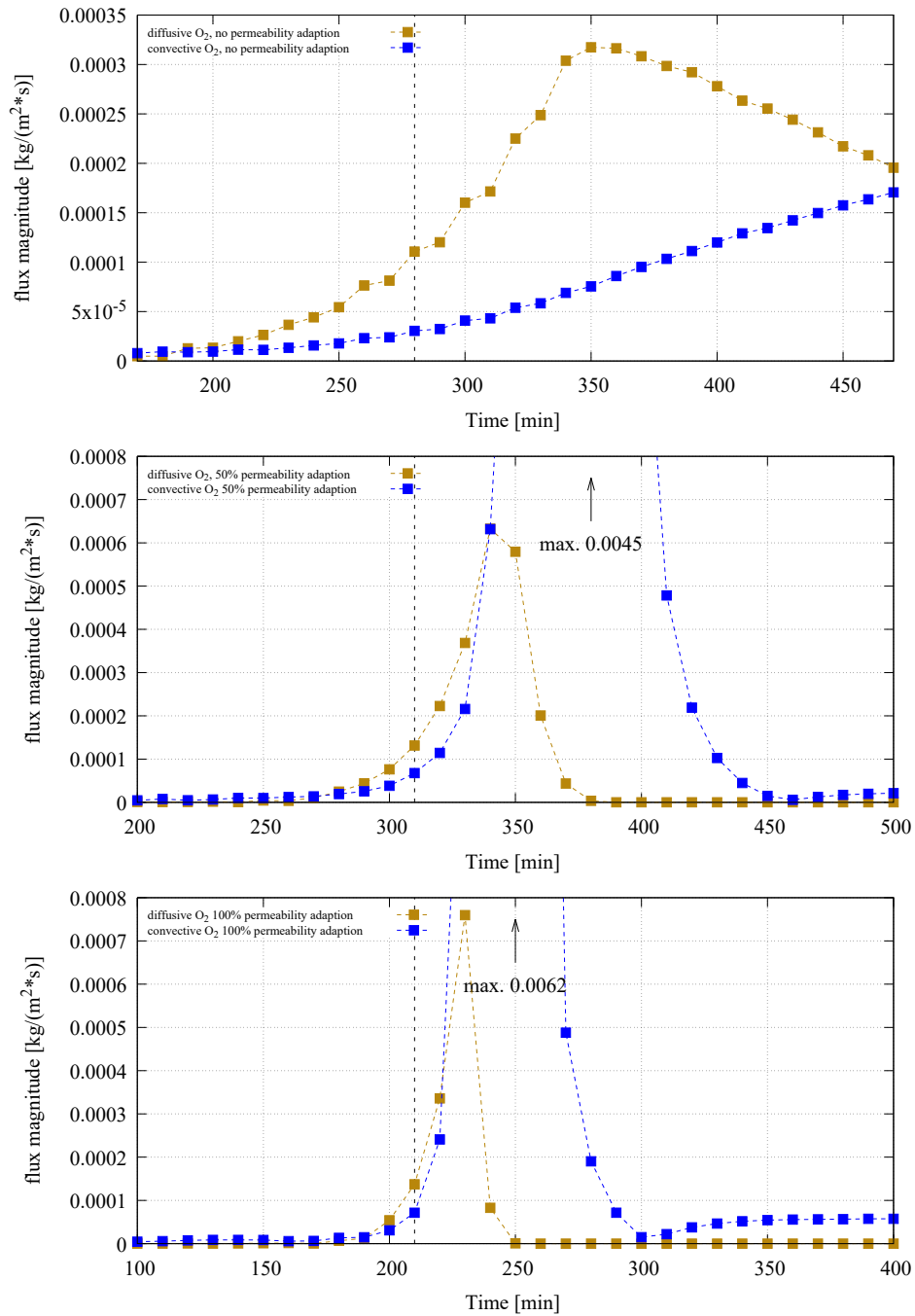


Figure 6.10.: Flux of oxygen for the three permeability-adaption cases at  $0.25 \cdot h_{sample}$  (first diagram) and  $0.5 \cdot h_{sample}$  (second and third diagram) along central axis. The diagrams are made to correspond at 280 min, 310 min and 210 min, the times of  $T_{max}$ .



The maximum temperature for each simulation is marked with a dashed line. At this point, it is assumed that the reaction front passes the probing point. After the reaction front passes the probing point, the heat source is above the point. Now, air at oven temperature is transported from the bottom upwards due to buoyancy. Therefore, the material, still hot from reaction, is cooled. A temperature gradient occurs, and downward conduction gains importance.

The air that enters the sample at the bottom, is heated up and transported upwards by convection. Thus heat is being prevented from leaving the sample through its lower surface. Instead of being transported to the lower surface, where it could leave the sample, it is looped back to the reaction front by convection.

All these effects are discernible, independently of the permeability adaption, but with increasing distinctness. For the no-permeability-adaption case, the convective heat flux is 16% of the total heat flux at the peak at 360 min, while the heat transferred back by convection is 38% of the total heat flux (350 min respectively 230 min) for both permeability adaption cases. These values are calculated from the data, shown in figure 6.12 and A.6. This amount of heat, looped back into the sample, is essentially responsible for the higher temperatures in the center, since heat loss decreases and more heat is accumulated in the system.

The heat flux over time through the bottom of the sample is shown in figure 6.11. All three cases were similar until ignition occurred. The maximum heat loss at approximately 100 min occurs when the reaction front is located at the bottom. At this point, the heat loss in all three cases is fairly high and of similar magnitude since temperatures are comparable. After that, the heat loss through the bottom decreased for all cases as the reaction front moved upwards; fastest for 100 % permeability adaption. Therefore, with increased permeability heat losses through the bottom are reduced. Considering the values when the maximum temperatures occur (dashed lines), heat loss through the bottom is very high in the case of no permeability adaption and quite low and of comparable magnitude for the two adaption cases.

Figure 6.13 shows the concentration of the product species at the outlet. It can be seen, that the produced species are maximum after ignition at approximately 100 min. Without permeability adaption, the product concentrations

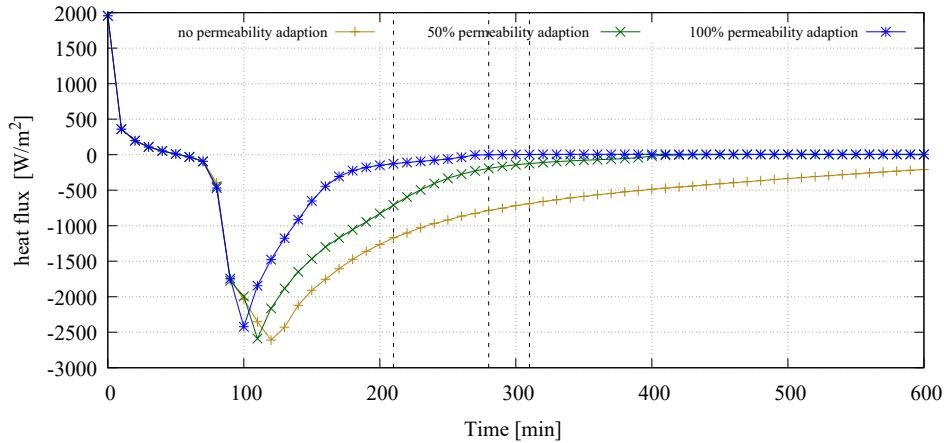


Figure 6.11.: Sum of convective and conductive heat flux through bottom over time for different permeability cases. Reaction front passed at 280 min (no adaption), 310 min (50% adaption) and 210 min (100% adaption) (dashed lines).

decrease. With increased permeability, the gas production is slightly reduced (50% permeability adaption) respectively stays constant (100% permeability adaption) due to the increasing rate of reaction. With increased convection, a small peak emerged at the end of the combustion process at 270 min respectively 180 min. This is induced by the oxygen-dependent reactions. Since all reaction equations have a similar  $CO/CO_2$  ratio, the ratio in the product composition remain constant as well. Between the different simulations, nearly no concentration difference was observed. Mass flow rate and outlet velocity increased, therefore the concentration stays almost constant, while absolute mass loss increased.

Comparing the simulation results with the measurements (Figure 5.10), it can be seen, that the curves display comparable curve shapes, while the absolute values from the simulation are smaller. Comparing the  $H_2O$  concentrations, it is evident, that the evaporation of humidity is not reproduced in the simulation. This is obvious consequence of the fact that water evaporation was not part of the model. The peak in the simulation is much wider, but at a much lower concentration than in the experiments. These wider and lower peaks are present for all species. Another difference is the second peak in the CO signal in measurements. As distinct from the experiments, this peak can be found for all species in the simulations. Therefore the  $CO/CO_2$  ratio is constant. The systematically lower values for all concentrations can be explained by the fact, that the sampling point of the FTIR was closer to the sample in the

experiments compared to the simulation and that the SEDEX oven, where the experiments with gas measurement took place, was mechanically ventilated, that might have circulated the product gas and lead to an increased concentration.

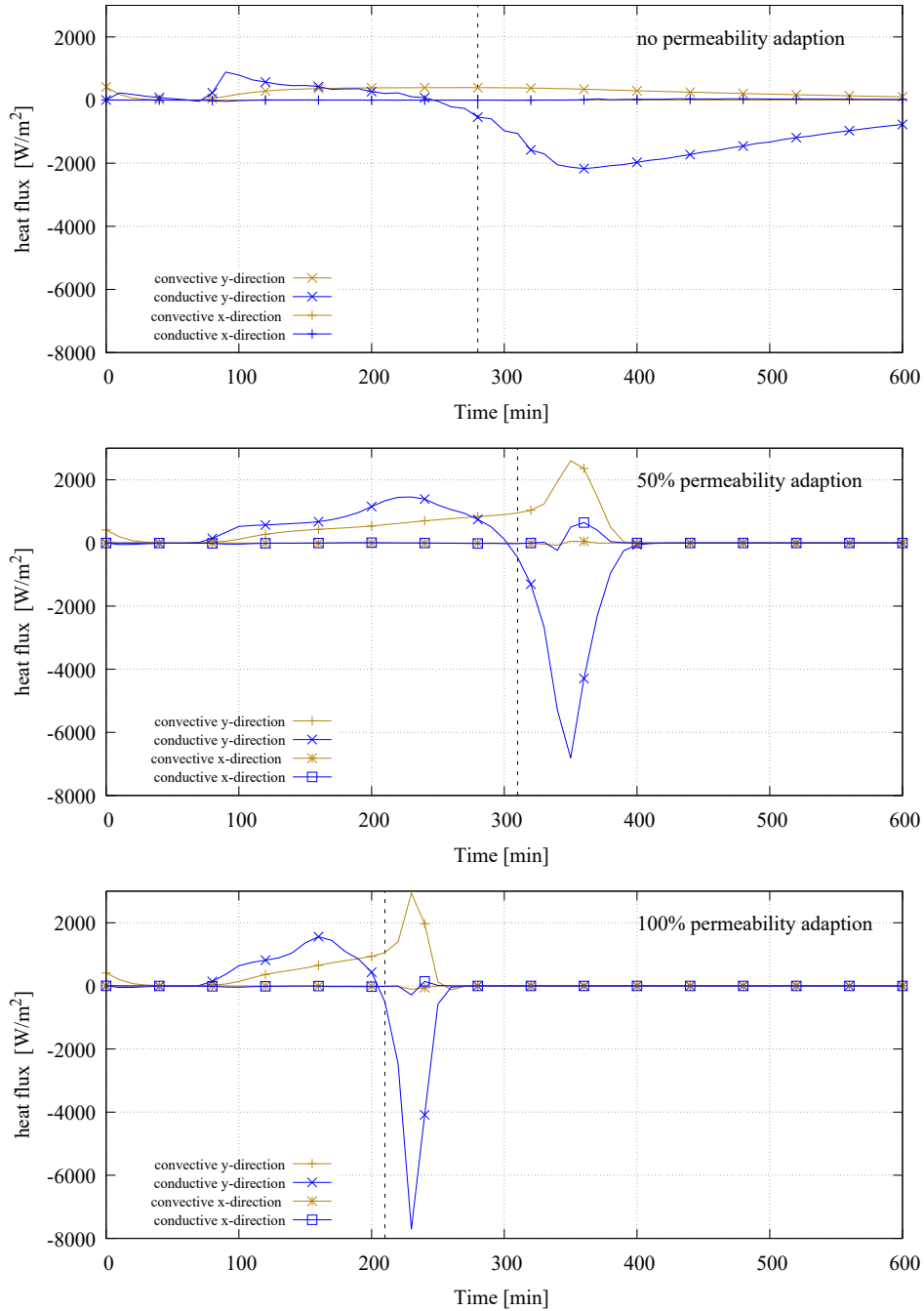


Figure 6.12.: Heat flux in x and y direction (upwards positive) at heights  $0.25 \cdot h_{sample}$  (first diagram) and  $0.5 \cdot h_{sample}$  (second and third diagram) along the central axis. The dashes lines indicate the times when the reaction front passes the sampling point.

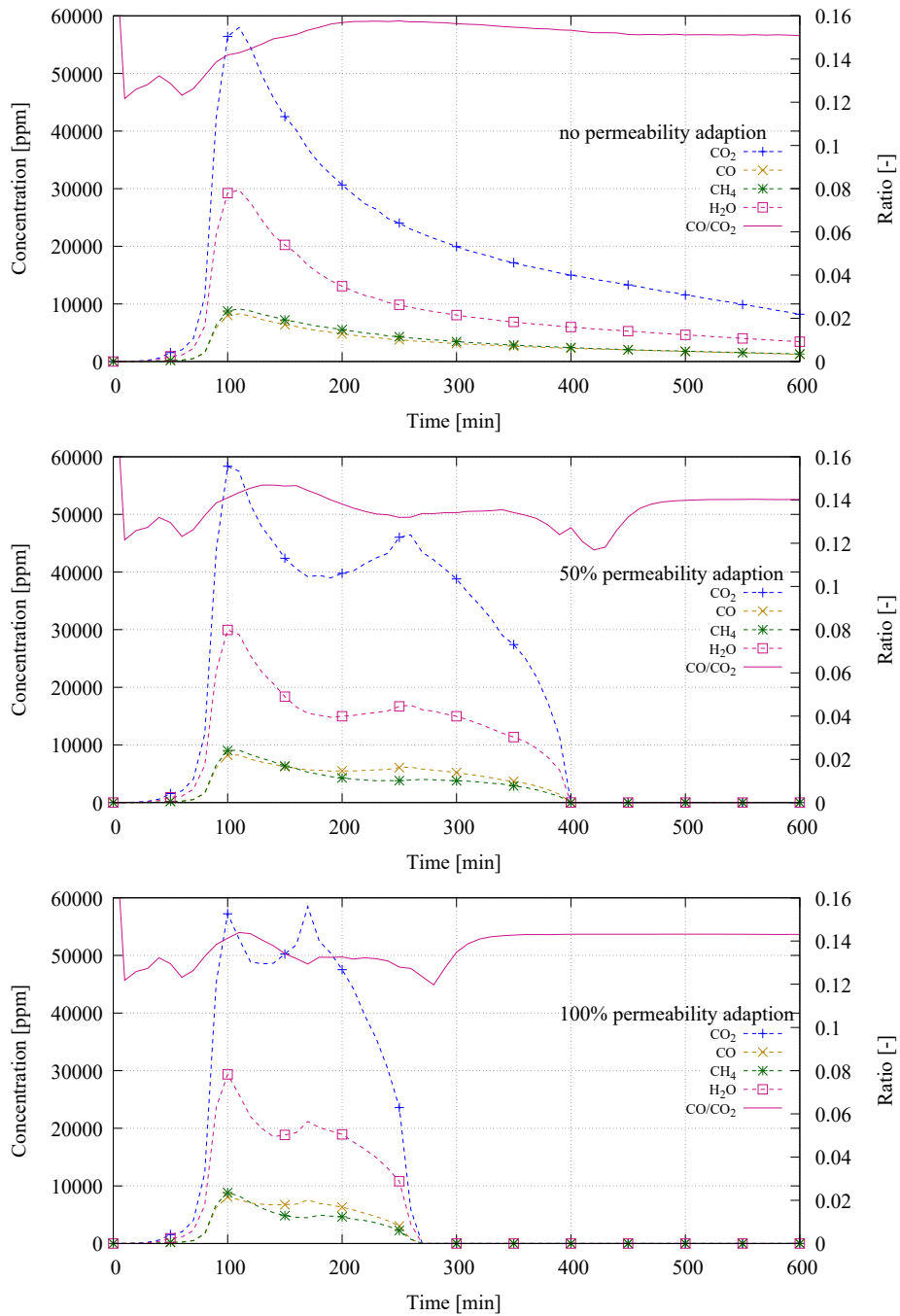


Figure 6.13.: Simulated concentration of combustion products at outlet.

## 7. Calculation of uncertainties in isoperibolic hot storage experiments

Any quantity that is measured or numerically calculated is subjected to uncertainties. Within this chapter, these uncertainties will be discussed. One of the main effects measured within this thesis is the increase in the maximum reaction temperature. The typical increase of several hundred K is small compared with the accuracy of the thermocouple of 1.5 K and the effect of the increased maximum reaction temperature is remarkable compared to the potential failure due to thermocouple accuracy. The significant difference was measured several times with different experimental setups and therefore thermocouples (see figure 5.5).

The estimation of uncertainties in the numerical simulation is not supposed to be part of this thesis. The reader is referred to the thesis of Melcher [69], who discussed uncertainties in numerical simulation of combustion processes.

Uncertainties will be discussed for isoperibolic hot storage experiments, as the derived formal kinetic data were the basis for the numerical investigation.

In order to determine the influence of uncertainties, a Monte Carlo (MC) simulation with  $10^4$  repetitions was conducted. MC-simulations rely on repeated random sampling. Parameters with uncertainties are varied using random numbers. The problem is calculated repeatedly using a new set random variables each time. As a result, the influence of uncertainties in the input parameters can be estimated, usually as probability density functions. Further information about MC-Simulation can be found, amongst others in [70].

The Matlab code that was used is shown in Appendix C. The code consist of two parts, within the first the uncertainties in activation energy and y intercept are estimated. This part is computationally quite slow, since the fit of the line is performed in a loop.

The second part calculates new random numbers using a normal distribution fitted to the data from the first part. This can be done using matrices only and can be executed pretty fast.

Considering isoperibolic hot-storage experiments, two main sources of errors could be identified in the experimental setup: the oven temperature measurement and the volume of the sample basket. Further errors like inhomogeneous sample material or bulk density can be neglected due to proper sampling in the experiments and ensuring a comparable bulk density before every experiment.

The volume of each basket was measured after it was manufactured. The stress during testing leads to deformation of the basket. Before a basket was scrapped, the volume was measured again. The difference in volume between the new and the used state of the basket was  $\pm 10\%$ .

The accuracy in the measurements of self-ignition temperature, was set to  $\pm 2\text{ K}$ . This is a rather high error since the precision of a thermocouple as such is least  $1.5\text{ K}$ . Furthermore, two thermocouples were used to measure the temperature of the oven to reduce total error. Anyhow, with the high value of  $2\text{ K}$ , deviations due to possible displacement of the thermocouples were taken into account.

Input parameters of the MC-simulation were the  $T_{SI}$  of LC-P shown in table 5.1 with their corresponding basket volumes. As described above, these two values were randomly distributed for each MC-repetition. Using equation 2.4 the slope and y intercept were determined  $10^4$  times using linear fitting. From these activation energy and pre-exponential factor were calculated.

The results of the MC-Simulation of the activation energy are shown in figure 7.1. A normal distribution could be fitted with a mean value of  $\mu = 109.94\text{ kJ/mol}$  and a standard derivation of  $\sigma = 3.31\text{ J/mol}$ . The minimum and maximum values were  $100.29\text{ kJ/mol}$  and  $122.73\text{ kJ/mol}$ . This demonstrates that the activation energy can be determined accurately from isoperibolic hot storage experiments.

The values for the y-intercept n gained from MC-Simulation (figure 7.2) are comparable in their accuracy. The mean value was  $\mu = 53.30\text{ K}^2/m^2$  and the

standard deviation  $\sigma = 1.07 \text{ K}^2/\text{m}^2$ . The minimal value was  $50.18 \text{ K}^2/\text{m}^2$  and the maximum  $57.41 \text{ K}^2/\text{m}^2$ .

For the calculation of the pre-exponential factor, four variations according to equation 5.1 were explored. For E and n, the variations calculated above were used, for the other values uncertainties were uniformly distributed with 20 % and 40 %

- **Case 1** Variation in E and n, as calculated
- **Case 2** Variation in E and n, as calculated; Q,  $\lambda$  and  $\rho$  even distributed with  $\pm 20 \%$
- **Case 3** Variation in E and n, as calculated; Q,  $\lambda$  and  $\rho$  even distributed with  $\pm 40 \%$
- **Case 4** Q,  $\lambda$  and  $\rho$  even distributed with  $\pm 20 \%$ , no variation in E and n

The results for case 1 to 3 are shown in figure 7.3 and for case 4 in figure 7.4. Due to the exponential function in equation 5.1, the results are obviously exponential distributed. Mean values of  $\mu = 1.64 \cdot 10^9 \text{ 1/s}$  for case 1,  $\mu = 1.67 \cdot 10^9 \text{ 1/s}$  for case 2 and  $\mu = 1.74 \cdot 10^9 \text{ 1/s}$  for case 3 were obtained. The standard deviation for the three cases equals the median.

This allows the conclusion, that the variation of the parameters Q,  $\lambda$  and  $\rho$  has nearly no influence on the accuracy of the pre-exponential factor. Otherwise, these three cases would differ and would not differ from case 4. The uncertainties in the pre-exponential factor are mainly caused by the uncertainties in the y intercept. Without the uncertainties in the y-intercept, the distribution of the pre-exponential factor would be as shown in figure 7.4. A much narrower distribution is visible. Due to the asymmetry, no distribution was fitted but a mean value around  $1 \cdot 10^9$  could be estimated from the data.

The formal kinetic data gained from the experiments were  $E = 110 \text{ kJ/mol}$  and  $k_0 = 1.1 \cdot 10^9 \text{ 1/s}$ . Taking the standard deviation  $\sigma = 3.31 \text{ J/mol}$  determined by MC-Simulation into account, it can be concluded that this value can be reliably measured. The mean value for the pre-exponential factor is also compliant, but the standard deviation is large. Even small errors in the determined y-intercept lead to quite large errors in  $k_0$ . These results of the MC-simulation corroborate the experimental results summarized in section 5.6



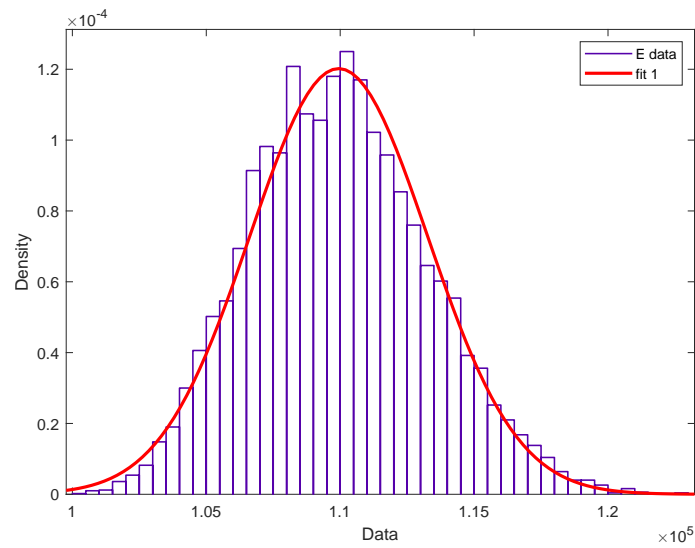


Figure 7.1.: Probability-density function from the MC-Simulation of apparent activation energy  $E$  [ $J/mol$ ], with fitted normal distribution ( $\mu = 109.94 J/mol$ ;  $\sigma = 3.31 J/mol$ )

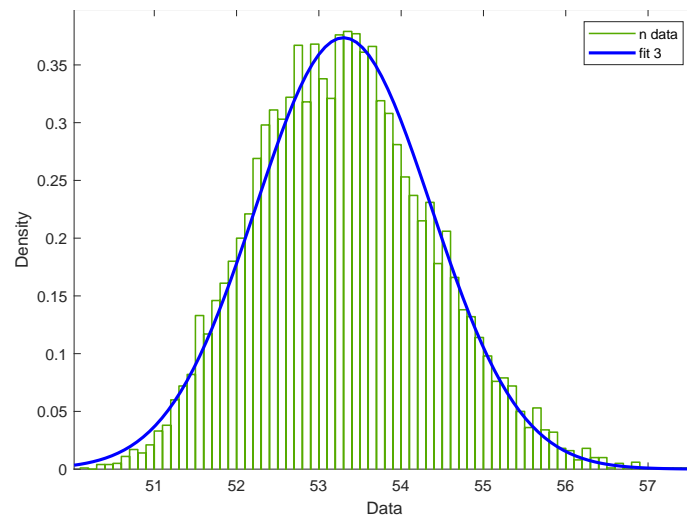


Figure 7.2.: Probability-density function of y intercept [ $K^2/m^2$ ], with fitted normal distribution ( $\mu = 53.30 K^2/m^2$   $\sigma = 1.07 K^2/m^2$ ).

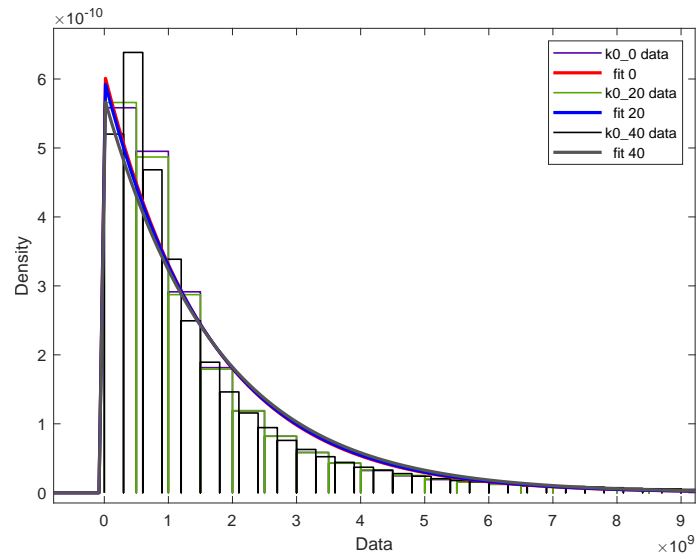


Figure 7.3.: Probability-density function of pre-exponential  $[1/s]$  factor for case 1 to 3, with fitted exponential distributions ( $\mu = 1.64 \cdot 10^9$ ;  $1.67 \cdot 10^9$ ;  $1.74 \cdot 10^9 1/s$  with a standard deviation that is equal).

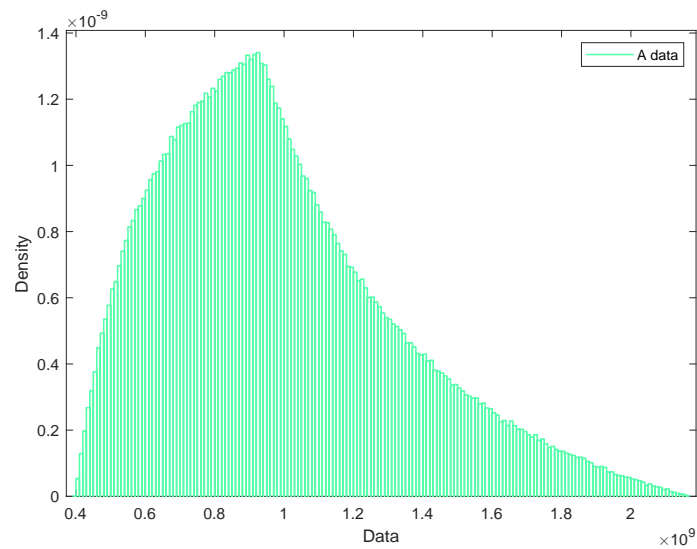


Figure 7.4.: Probability-density function of pre-exponential factor  $[1/s]$  for case 4

## 8. Summary and Outlook

The aim of this work was to examine the influence of inert material in mixtures with combustibles on the self-ignition and reaction behavior of combustible bulk material. This was done by conducting isoperibolic and adiabatic hot-storage experiments, with spontaneous convection, and experiments with forced convection in a pipe placed in an oven. Furthermore, STA experiments were conducted and gasses were measured via FTIR. Additionally, some experiments were conducted to determine material properties needed as input for simulation. Simulation was used to examine the effect of changes in permeability.

### **Influence on self-ignition temperature and kinetic parameters**

Inert materials do not influence kinetic parameters independent of material, particle size, specific surface, and the testing method. This is not a surprising result, since an inert material does not change the reaction. Nevertheless, an extra surface is added, especially for the mixtures with magnesia oxides, that's specific surface is very high compared to the lignite. An catalytic surface effect cannot be excluded in general, but the experimental data shows no measurable evidence.

The influence on the self-ignition temperature is evident. An inert material, independently of material, particle size and specific surface, increased the self-ignition temperature. The proposed mechanism is that non-reactive particles act as a heat sink. On the one hand, the inert material did not participate in the reaction, on the other hand it had to be heated up. The effect shown in this work consolidates the effects published in [3] and [5].

## **Influence on maximum reaction temperature**

The influence on the maximum reaction temperature was investigated experimentally and was corroborated by numerical calculations.

During the experiments, it was observed that the remaining material of the combustion process (ash, semi-burnt and unburnt material) and did not assemble in the bottom of the basket, when inert material of a certain particle size was added. This indicated, that the inert material built a supporting structure that kept the combustible particles in place during combustion. This kept the pores open during the shrinking process. Therefore, porosity and permeability were increased, which led to a different flow regime. On the one hand, convective mass transfer became more important. On the other, heat transfer also became dominated by convection after a certain amount of combustible had been burnt off. At this stage, pores had formed.

As stated in section 6.2.1, three simulations were conducted. Within one of them the permeability was not changed during the combustion process to represent the combustion of pure combustible. Within two simulations, permeability was increased with decreasing combustible concentration. These simulations were supposed to represent the inert cases. In one of these two simulations, permeability was increased to a value that should represent the 50 % mixture with inert material (100 % permeability adaption), the second simulation was done with half of that value (50 % permeability adaption) to have a step in between.

The main outcome of the simulations is that diffusive transport dominates the model with no permeability adaption. On the other hand, convective transport dominates in cases with permeability adaption. For that reason, the supply of oxygen and the removal of exhaust gasses is faster. The heat, that is conducted towards the bottom of the basket, preheates the upwards flowing air. This effect increases with increasing fluid flow and, therefore, with a increasing permeability. The gasses entering the combustion zone are, thus, preheated. Both effects, increased oxygen supply and preheating of gasses, are overlapping and enable higher reaction temperatures.

## **Outlook for further investigations**

It has been shown that inert material can increase the maximum reaction temperature in bulk material by changing the flow regime. Further work could investigate applications of these effects. Higher temperatures can increase the conversion of a substance, or might be used to burn and, as a consequence, destroy unwanted substances, like exhaust gasses. Furthermore, the added inert material could act as a filter. Another field of application is smoldering combustion in liquid or melting material. The best-known example is oil-soaked clothes for cleaning that will ignite if stored improperly. Melting solids will not undergo smoldering combustion, since the porous structure melts together above the melting point. If these are mixed with an inert solid, that supports a large surface on the one hand, and on the other acts as a supporting structure that prevents agglomeration during melting. Therefore, a smoldering combustion may be possible [71].

The numerical investigation has demonstrated the mechanisms at work, but the increase in temperatures is lower than measured in the experiments. This might be caused by an insufficient reaction scheme. It is also indicated by the fact that gas concentrations were systematically smaller by approximately the factor of 0.3 in the simulation. This be improved in further numerical work.

It could be useful to conduct STA investigation using different heating rates with a coupled FTIR under a variation in the oxygen concentration. From these experiments, oxygen-depended reaction equations could be formulated and the heat of combustion could be measured. If the experiment is done at different heating rates, formal kinetic data could be calculated.

Furthermore, the simulation should be validated for larger basket volumes and also in 3D.

## Bibliography

- [1] Hoischen, U. ; Kayser, J. *Fires In Silos, Chapter 7*. WILEY-VCH Verlag GmbH, 2009. 1.1
- [2] Mikaelsen, R. M. *Fighting flameless fires*. PhD thesis, Otto-von-Guericke-Universität Magdeburg, 2018. 1.1
- [3] Schossig, J.; Berger, A.; Malow, M.; Krause, U. Beurteilung und Verhinderung von Selbstentzündung und Brandgasemission bei der Lagerung von Massenschüttgütern und Deponiestoffen. *BAM Forschungsbericht 291*, 2010. 1.1, 1.1, 1.2, 5.1.1, 5.1.2, 6.2.2, 8
- [4] Schäfer, M. *Auswertung von LANDSAT-7 ETM+ und ASTER-Daten zur Erfassung von Temperaturanomalien der Landoberfläche*. Technische Universität Clausthal, Diplomarbeit, 2003. 1.1
- [5] Restuccia, F.; Huang, X; Rein, G. Self-ignition of natural fuels: Can wildfires of carbon-rich soil start by self-heating? *Fire Safety Journal*, 2017. 1.1, 1.1, 3, 8
- [6] Lohrer, C. Einflussgrößen auf die Selbstentzündung von Schüttgütern und Stäuben - experimentelle Untersuchungen und numerische Simulationen. *PhD Thesis, Technischen Universität Berlin*, 2005. 1.1, 2.1, 3, 6.2.2
- [7] Person, H. Silo Fires - Fire extinguishing and preventive and preparatory measures. *Swedish Civil Contingencies Agency*, 2013. 1.1
- [8] Babrauskas, V. *Ignition Handbook*. Fire Science Publishers, Issaquah, 2003. 1.1, 2.1, 2.2
- [9] Trimis, D.; Durst, F. Combustion in a Porous Medium-Advances and Applications. *Combustion Science and Technology*, 1996. 1.2
- [10] Hensel, W.; Krause, U.; Löffler, U. *Selbstentzündung fester Stoffe (einschließlich Stäube) in Handbuch des Explosionsschutzes*. WILEY-VHC, 2000. 2.1, 2.3.1, 2.3, 2.3.2

- [11] Hagen, B. C. Onset of smoldering and transition to flaming fire. *Dissertation*, 2013. [2.1](#)
- [12] Krause, U. *Fires in Silos: hazards, prevention and fire fighting*. Wiley & Sons, 2009. [2.1](#)
- [13] Drysdale, D. D. *Smoldering Combustion in: An introduction to Fire Dynamics, Third Edition*. Wiley & Sons, 2011. [2.1](#)
- [14] Rein, G. *Smoldering Combustion*, volume SFPE Handbook of Fire Protection Engineering 5th Edition, Chapter 19. Springer, 2016. [2.1](#)
- [15] Beuth Verlag, Berlin. *DIN EN 15188 Bestimmung des Selbstentzündungsverhaltens von Staubschüttungen*. Normenausschuss Sicherheitstechnische Grundsätze, 2007. [2.1](#), [2.3.1](#), [2.2](#), [4.1](#)
- [16] Ohlemiller, T. J. Modeling of Smoldering Combustion Propagation. *U.S. DEPARTMENT OF COMMERCE National Bureau of Standards National Engineering Laboratory Center for Fire Research*, 1984. [2.1](#)
- [17] Semenov, N.N. . Chemical kinetics and chain reactions. *The Clarendon Press*, 1953. [2.2](#)
- [18] Semenov, N.N. . Zur Theorie des Verbrennungsprozesses. *Zeitschrift für Physik, Deutsche Physikgesellschaft*, Band 48:571ff, 1928. [2.2](#)
- [19] Fank-Kamenetzki, D. A. *Stoff und Wärmeübertragung in der chemischen Kinetik*. Springer Verlag Berlin Göttingen Heidelberg, 1959. [2.2](#)
- [20] Frank-Kamenetzki, D. A. . *Diffusion and heat transfer in chemical kinetics*. Plenum Press, London, 1969. [2.2](#)
- [21] Thomas, P.H. Some approximations in the theory of self-heating and thermal explosion. *Transactions of the Faraday Society*, 56:833ff, 1960. [2.2](#)
- [22] Thomas, P.H. On the thermal conduction equation for self-heating materials with surface cooling. *Transactions of the Faraday Society*, 54:60ff, 1958. [2.2](#)
- [23] Hensel, W.; *Die Schichtdickenabhängigkeit der Glimmtemperaturen Theorie und Praxis der Selbstentzündungs- und Glimmvorgänge von Stäuben. Fortschrittsbericht VDI Reihe 3 Nr. 244*. VDI-Verlag Düsseldorf, 1991. [2.2](#), [2.1](#), [2.2](#), [2.1](#)

- [24] Malow, M.; Krause, U. The overall activation energy of the exothermic reactions of thermally unstable materials. *The Journal of Loss Prevention in the process industries*, 17:51ff, 2004. [2.2](#), [3](#)
- [25] Binkau, B.; Wanke, C.; Krause, U. Examination of the influence of inert materials on the spontaneous ignition and burnout of porous solid materials. *Proceedings of the Seventh International Seminar Fire and Explosion Hazards*, 7:., 2013. [2.3.1](#), [4.3](#)
- [26] Wanke, C.; Binkau, B.; Krause, U. Influences of inert and inhibitory materials on the burning behavior of flammable dusts. *Proceedings of X-ISHPMIE*, 10, 2014. [2.3.1](#), [4.2](#), [4.3](#), [5.1](#), [5.1.2](#), [5.2](#)
- [27] Schossig, J.; Schmidt, M.; Krause, U. Abschlussbericht Forschungsvorhaben "Validierung von formalkinetischen Größen aus der adiabatischen Warmlagerung". *Bundesanstalt für Materialforschung und prüfung (BAM)*, 2012. [2.3.2](#)
- [28] Steen, H.; editor. *Handbuch des Explosionsschutzes*. WILEY-VCH, 2000. [3](#)
- [29] Dullien, F. A. L. . *Porous Media, Fluid Transport and Pore Structure*. Academic Press Inc., 1992. [3](#), [3.2.2](#), [3.2.3](#), [3.2.3](#)
- [30] Cray, D. *Deep Underground, Miles of Hidden Wildfires Rage*. Time Magazine, 2010. [3.1](#)
- [31] Koensler, W. *Sand und Kiese - Mineralogie, Vorkommen, Eigenschaften, Einsatzmöglichkeiten*. Ferdinand Enke Verlag, 1989. [3.1](#)
- [32] Bear, J. *Dynamics of Fluids in Porous Media*. Dover Publications Inc. New York, 1988. [3.2](#), [3.2.3](#), [6.2.2](#)
- [33] Krause, U.; John, W.; Machnow, K.; Hammerschmidt, U. Messverfahren zur Bestimmung der Wärmetransportfähigkeit. *Patent DE 102 58 817 B4*, 2006. [3.2.4](#)
- [34] Seeger, S. Bestimmung der Wärmeleitfähigkeit von abgelagerten Schuttgütern mittels des stationären Plattenverfahrens (Bachelorthesis). *Otto-von-Guericke-Universität Magdeburg*, 2016. [3.2.4](#)



- [35] Tan, B; Cheng, G. et. al. *Experimental Study on the Physisorption Characteristics of O<sub>2</sub> in Coal Powder are Effected by Coal Nanopore Structure*. Nature, Scientific Reports, 2020. [3.2.6](#)
- [36] *VDI-Wärmeatlas (VDI-Buch) (German Edition)*. Springer, 2005. [3.2.8](#)
- [37] Honza, T. Bestimmung der Wärmekapazität von abgelagerten Schuttgütern mittels instationärer Wärmeleitung. *Bachelorthesis*, 2016. [3.2.8](#), [3.5](#)
- [38] Chase, M. W. Thermochemical Tables, Fourth Edition. *NIST-JANAF*, 1998. [3.2.8](#)
- [39] Bauszus, A. Untersuchung der formalkinetischen Parameter der Selbstentzündung im Sedex-Ofen. (*Masterthesis*), 2013. [4.1](#)
- [40] Inayat, M. Thermogravimetric kinetic analysis of Malaysian poultry processing waste material under inert and oxidative atmospheres. *Journal of Mechanical Engineering and Sciences*, 2016. [4.4](#)
- [41] Krause, U.; Schmidt, M.; Ferrero, F. Investigation of the development of conflagration of solid material via analysis of coupled heat, mass and momentum transport. *Chemical Engineering and Technology*, 32:291–305, 2009. [4.3](#), [6.2.2](#)
- [42] Hollas, J. M. Modern Spectroscopy, Third Edition. *John Wiley and Sons, England*, 1996. [4.4](#)
- [43] Atkins, P.; Paula, J. Physical chemistry. *Oxford University Press*, 2002. [4.4](#)
- [44] Leng, Y. *Materials Charakterisation*. Wiley-VCH, 2013. [4.5](#)
- [45] Schwartz, O. Einfluss der Probengröße auf die formalkinetischen Parameter der Selbstentzündung brennbarer Stäube bei Warmlagerungsversuchen mit Braunkohle (Bachelorthesis). *Otto-von-Guericke-Universität Magdeburg*, 2014. [5.1](#)
- [46] Wanke, C.; Binkau, B.; Zinke, R.; Krause, U. The influence of inert materials on the self-ignition temperature and maximum reaction temperature of bulk materials. *Proceedings of X-ISHPMIE*, 11, 2016. [5.1.2](#), [5.3](#), [5.1.2](#), [5.5](#), [5.7](#), [5.4](#), [A.5](#)

- [47] Arsand, U. Einfluss von Inerten Stoffen auf die formalkinetischen Parameter der Selbstentzündung brennbarer Stäube (Bachelorthesis). *Otto-von-Guericke-Universität Magdeburg*, 2013. 5.1.2, 5.2
- [48] Wanke, C.; Binkau, B.; Krause, U. Einfluss von inert und inhibitorisch wirkenden Stoffen auf die Selbstentzündungstemperatur. *11. Fachtagung Anlagen-, Arbeits- und Umweltsicherheit Köthen*, ISBN-978-3-86011-058-4, 2013. 5.2
- [49] Tillmann, D.; Harding, N. S. Modeling and Fuel Blending. *Solid Fuel Blending, Chapter 7*, 2012. 6
- [50] Westermann, T. *Modellbildung und Simulation: Mit einer Einführung in ANSYS*. Springer-Verlag, Berlin, Heidelberg, 2010. 6.1
- [51] Schwarz, H. R.; Köckler, N. *Numerische Mathematik. 8. Auflage*. Vieweg+Teubner Verlag, 2011. 6.1
- [52] Roos, H.-G.; Tobiska, L., editor. *Die Finite-Elemente-Methode für Anfänger. 4. Auflage*. Wiley-VCH Verlag GmbH & Co. KGaA, 2010. 6.1
- [53] Logan, D.-L. *A first course in the finite element method*. Cengage Learning, 2011. 6.1
- [54] Beinstingel, A. *Implementierung der Methode der Finiten Elemente zur Lösung eindimensionaler Randwertprobleme in C++*. Projektarbeit Hochschule für angewandte Wissenschaften München, 2015. 6.1
- [55] COMSOL 5.3 User's Guide. . 2017. 6.2, 6.2.2, 6.2.4, 6.2.4, 6.6
- [56] Krause, U.; Lohrer, C.; Schmidt, M. Prediction of real-scale coal fire scenarios based on linking lab-scale experiments with a numerical heat and mass transfer model. *ERSEC Spontaneous Coal Seam Fires: Mitigating a Global Disaster*, 2005. 6.2.2
- [57] Krause, U.; Schmidt, M.; Lohrer, C. A numerical model to simulate smouldering fires in bulk materials and dust deposits. *Journal of Loss Prevention in the Process Industries*, 19:218226, 2006. 6.2.2
- [58] Lyu, P. Which Porous Media and Subsurface Flow Interface Should I Use? *COMSOL BLOG*, pages <https://www.comsol.com/blogs/which-porous-media-and-subsurface-flow-interface-should-i-use/>, 2017. 6.1, 6.2.2

- [59] Conself blog; Mesh issues causing poor CFD simulation accuracy. <https://conself.com/blog/4-mesh-issues-poor-accuracy/>. visited 20.04.21, 2021. 6.3
- [60] Costa, A. Permeability-porosity relationship: A reexamination of the Kozeny-Carman equation based on a fractal pore-space geometry assumption. *Article in Geophysical Research Letters*, 2006. 6.3.2
- [61] Müller, R. Die Annäherung der Temperaturabhängigkeit der Transportkoeffizienten von Gasen durch einen Potenzansatz. *Chemie Ingenieur Technik*, 40:344–349, 1968. 6.3.2
- [62] Marshall, T. J. The diffusion of gases through porous media. *Journal of Soil Science*, 10, 1959. 6.3.2
- [63] Penman, H.L. Gas and vapour movements in the soil. *The Journal of Agricultural Science*, 30 Issue 3:437 – 462, 1940. 6.3.2
- [64] Specht, E. *Kinetik der Abbaureaktion*. CUETEC-Schriftenreihe, 1993. 6.4.1
- [65] Bal, N.; Rein, G. Relevant model complexity for non-charring polymer pyrolysis. *Fire Safety Journal*, 2013. 6.4.1
- [66] Bal, N.; Rein, G. On the effect of inverse modelling and compensation-effects in computational pyrolysis for fire scenarios. *Fire Safety Journal*, 2015. 6.4.1
- [67] <https://www.pardiso-project.org/>. 6.6
- [68] <http://mumps.enseiht.fr/>. 6.6
- [69] Melcher, T. Reproduzierbarkeit von Brandversuchen - experimentelle und numerische Betrachtungen. *Dissertation*, 2017. 7
- [70] Wanke, C. Einfluss von Unsicherheiten auf kritische Infrastrukturen am Beispiel der Stromversorgung - Softwaretechnischer Umsetzung. *Masterthesis*, 2011. 7
- [71] Henze, S. Bestimmung von Selbstentzündungs- und Reaktionsparametern in Feststoff-Feststoff Gemischen mit schmelzenden Bestandteilen. *Otto-von-Guericke-Universität Magdeburg Masterthesis*, 2017. 8

## **A. Appendix**

# Gasmeter™ DX4000 FTIR gas analyzer



## Multicomponent FTIR Gas Analyzer

Gasmeter On-site Series includes portable multicomponent gas analyzers for demanding applications. The Gasmeter DX4000 incorporates a Fourier transform infrared, FTIR spectrometer, a temperature controlled sample cell, and signal processing electronics. The analyzer offers versatility and high performance for all users.

The Gasmeter DX4000 is designed for short term on site measurements with wide dynamic ranges. It is an ideal tool to measure trace concentrations of pollutants in wet, corrosive gas streams. The sample cell can be heated up to 180 °C. Sample cell absorption path length is selected according to the application.

The Gasmeter DX4000 allows simple calibration using only single component calibration gases. The user can easily configure the analyzer for a new set of compounds.

### General parameters

<b>Measuring principle:</b>	Fourier transform infrared, FTIR
<b>Performance:</b>	Simultaneous analysis of up to 50 gas compounds
<b>Response time, T<sub>90</sub>:</b>	Typically < 120 s, depending on the gas flow and measurement time
<b>Operating temperature:</b>	Short term 0 - 40°C long term 5 - 30°C non-condensing

Gasmeter Technologies Oy | Pulttitie 8 A  
FI-00880 Helsinki  
Finland

<b>Storage temperature:</b>	-20 - 60°C, non-condensing
<b>Power supply:</b>	100-115 or 230 V / 50 -60 Hz
<b>Power consumption:</b>	Average 150 W, maximum 300 W

### Spectrometer

<b>Resolution:</b>	8 cm <sup>-1</sup> or 4 cm <sup>-1</sup>
<b>Scan frequency:</b>	10 scans / s
<b>Detector:</b>	Peltier cooled MCT
<b>Source:</b>	SiC, 1550 K
<b>Beamsplitter:</b>	ZnSe
<b>Window material:</b>	ZnSe
<b>Wave number range:</b>	900 - 4 200 cm <sup>-1</sup>

### Sample cell

<b>Structure:</b>	Multi-pass, fixed path length 5.0 m
<b>Material:</b>	100 % rhodium coated aluminium
<b>Mirrors:</b>	Fixed, protected gold coating
<b>Volume:</b>	0.4 liters
<b>Connectors:</b>	Inlet Swagelok 6 mm Outlet Swagelok 8 mm
<b>Gaskets:</b>	Viton® O-rings
<b>Temperature:</b>	180 °C, maximum

TEL: +358 9 759 00 400  
FAX: +358 9 759 00 450  
EMAIL: [contact@gasmeter.fi](mailto:contact@gasmeter.fi)

WEB: [www.gasmeter.fi](http://www.gasmeter.fi)  
VAT NO: FI19526395

Window material: BaF<sub>2</sub>

### Measuring parameters

**Zero point calibration:** 24 hours, calibration with nitrogen (4.0 or higher N<sub>2</sub> recommended)

**Zero point drift:** < 2 % of measuring range per zero point calibration interval

**Sensitivity drift:** None

**Linearity deviation:** < 2 % of measuring range

**Temperature drifts:** < 2 % of measuring range per 10 K temperature change

**Pressure influence:** 1 % change of measuring value for 1 % sample pressure change. Ambient pressure changes measured and compensated

### Electrical connectors:

**Digital Interface:** 9-pole D-connector for RS-232  
Analyzer is connected to an external computer via RS-232C cable. The external computer controls Gasmeter.  
Remote control connection for Portable sampling unit

**Power connection:** Standard plug CEE-22

**PSS connection:** Remote connection of PSS (Portable Sampling System)

### Gas inlet and outlet conditions

**Gas temperature:** Non-condensing, the sample gas temperature should be the same as the sample cell temperature

**Flow rate:** 120 - 600 liters per hour

**Gas filtration:** Filtration of particulates (2 µm) required

**Sample gas pressure:** Ambient

**Sample pump:** External, not included

### Electronics

**A/D converter:** Dynamic range 95 dB

**Signal processor:** 32-bit floating point DSP  
120 MFLOPS speed

**Computer:** External, not included

### Analysis software (for external PC)

**Operating system:** Windows XP

**Analysis software:** Calcmet for Windows

### Options

**Sample cell:** Multi-pass, fixed path length 2.5 m or 9.8 m

**Pressure measurement:** Inside sample cell

**Analog signals (ext PC):** ADAM 5000/TCP module (for analog inputs, outputs, relays)

**Sample cell gaskets:** Teflon® coated Viton® or Kalrez®

**Trolley:** Wheeled cart for the analyzer and laptop computer

### Enclosure

**Material:** Aluminium

**Dimensions (mm):** 390 \* 445 \* 164

**Weight:** 13.9 kg

**CE label:** According to EMI guideline 89/336/EC

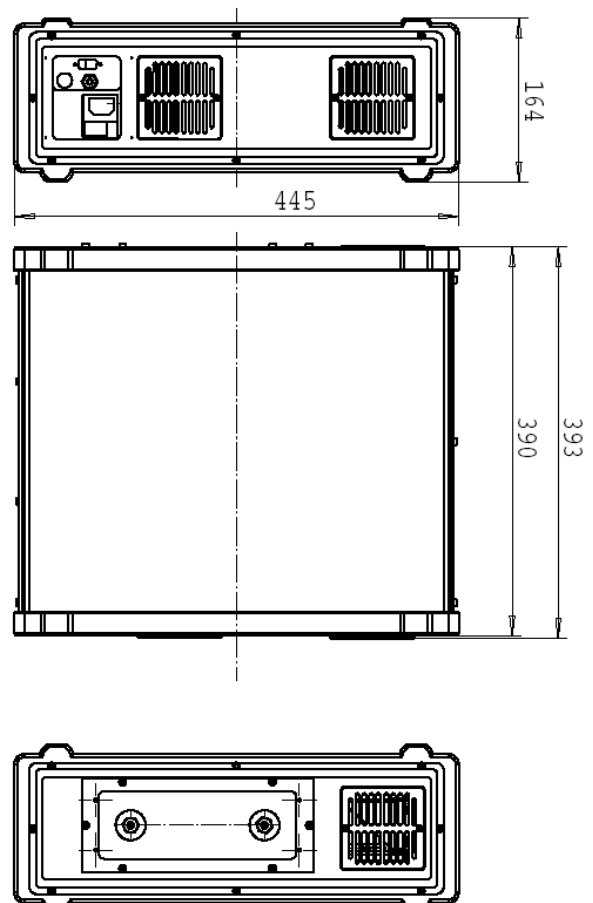




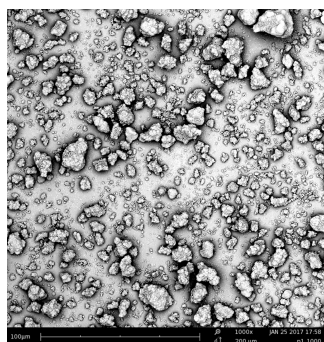
Table A.1.: Ratio of main combustion products from FTIR experiments (see fig. 5.10). Area below curve calculated by numerical integration, normalized to smallest amount.

time	substance	$CO_2$	$CO$	$CH_4$
total	LC-P	11,8	2,1	1,0
total	LC-P 50 S063-50	27,2	3,5	1,0
start-4.9h	LC-P	6,6	1,0	1,1
start-4.9h	LC-P 50 S063-50	15,6	1,9	1,0
4.9h -end	LC-P	72,2	14,9	1,0
4.9h -end	LC-P 50 S063-50	184,4	25,7	1,0

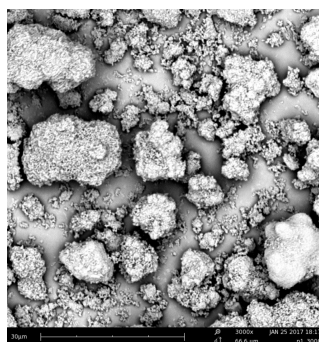
Table A.2.: Heat of formation of the complete reaction products, heat of reaction (LCV) and heat of formation for fuel and char

Product	$LC - P$ - fuel			$LC - P_{tt}$ - char		
	n[mol]	$\Delta H_f [\frac{kJ}{mol}]$	$(n \cdot \Delta H_f) [\frac{kJ}{mol}]$	n[mol]	$\Delta H_f [\frac{kJ}{mol}]$	$(n \cdot \Delta H_f) [\frac{kJ}{mol}]$
$CO_2$	10,1	393,8	3986,0	2,6	393,8	1015,1
$H_2O$	5,2	242,0	1249,0	0,6	242,0	139,8
char	1,0		507,5			
	$\Sigma \Delta H_{f\_products}$		5742,5	$\Sigma \Delta H_{f\_products}$		1154,9
		$\Delta H_{r\_fuel}$	-3534,5		$\Delta H_{r\_char}$	-647,4
		$\Delta H_{f\_fuel}$	=2207,5		$\Delta H_{f\_char}$	=507,5





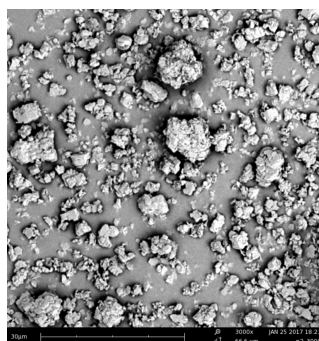
(a) MO 130 1000x



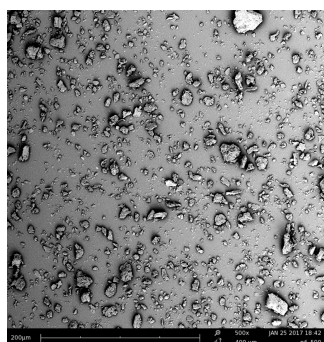
(b) MO 130 3000x



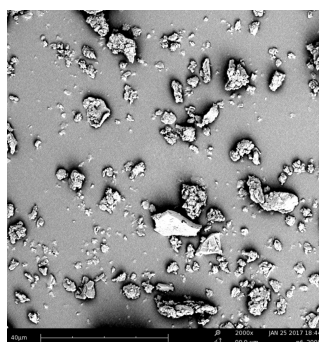
(c) MO 150 1000x



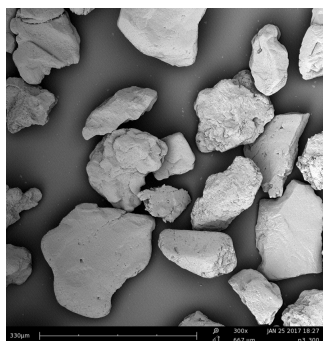
(d) MO 150 3000x



(e) LC-P 500x



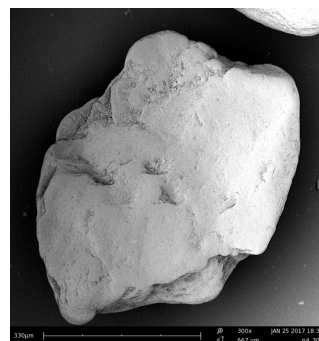
(f) LC-P 2000x



(g) S 200 300x



(h) S 063 300x



(i) S 700 2000x

Figure A.1.: SEM pictures of used substances

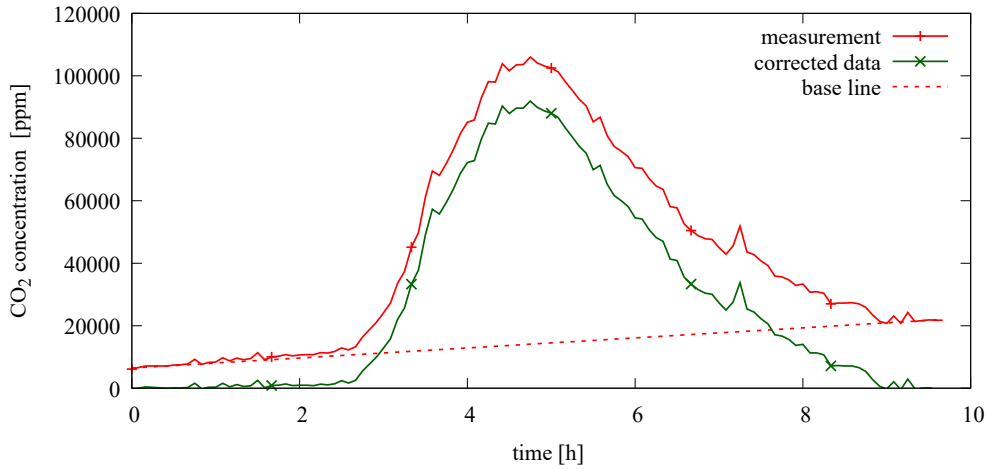


Figure A.2.: Correction of  $CO_2$  concentrations in the FTIR measurements in the Sedex oven, exemplary shown for one curve.

Table A.3.: Heat of formation of the reaction products and heat of reaction for more and less oxidated incomplete fuel reaction

	less oxidated			well oxidated		
Product	n[mol]	$\Delta H_f [\frac{kJ}{mol}]$	$(n \cdot \Delta H_f) [\frac{kJ}{mol}]$	n[mol]	$\Delta H_f [\frac{kJ}{mol}]$	$(n \cdot \Delta H_f) [\frac{kJ}{mol}]$
$CO_2$	5.7	393.8	2245.1	6.3	393.8	2496.5
CO	0.9	110.6	96.2	0.8	110.6	85.8
$CH_4$	1.1	75.0	84.6	0.5	75.0	36.2
$H_2O$	2.3	242.0	558.1	3.6	242.0	870.4
char	1.0	507.5	507.5	1.0	507.5	507.5
		$\sum \Delta H_{f\_products}$	3491.5		$\sum \Delta H_{f\_products}$	3996.4
		$\Delta H_{f\_fuel}$	-2207.5		$\Delta H_{f\_fuel}$	-2207.5
		$\Delta H_r$	=1284.0		$\Delta H_r$	=1788.9

Table A.4.: Heat of formation of the reaction products and heat of reaction for more and less oxidated incomplete char reaction

	less oxidated			well oxidated		
Product	n[mol]	$\Delta H_f [\frac{kJ}{mol}]$	$(n \cdot \Delta H_f) [\frac{kJ}{mol}]$	n[mol]	$\Delta H_f [\frac{kJ}{mol}]$	$(n \cdot \Delta H_f) [\frac{kJ}{mol}]$
$CO_2$	2,1	393,8	823,4	2,3	393,8	886,7
CO	0,4	110,6	47,6	0,1	110,6	15,6
$H_2O$	0,6	242,0	139,8	0,6	242,0	139,8
		$\sum \Delta H_{f\_products}$	1010,8		$\sum \Delta H_{f\_products}$	1042,0
		$\Delta H_{f\_char}$	-507,5		$\Delta H_{f\_char}$	-507,5
		$\Delta H_r$	=503,3		$\Delta H_r$	=534,5

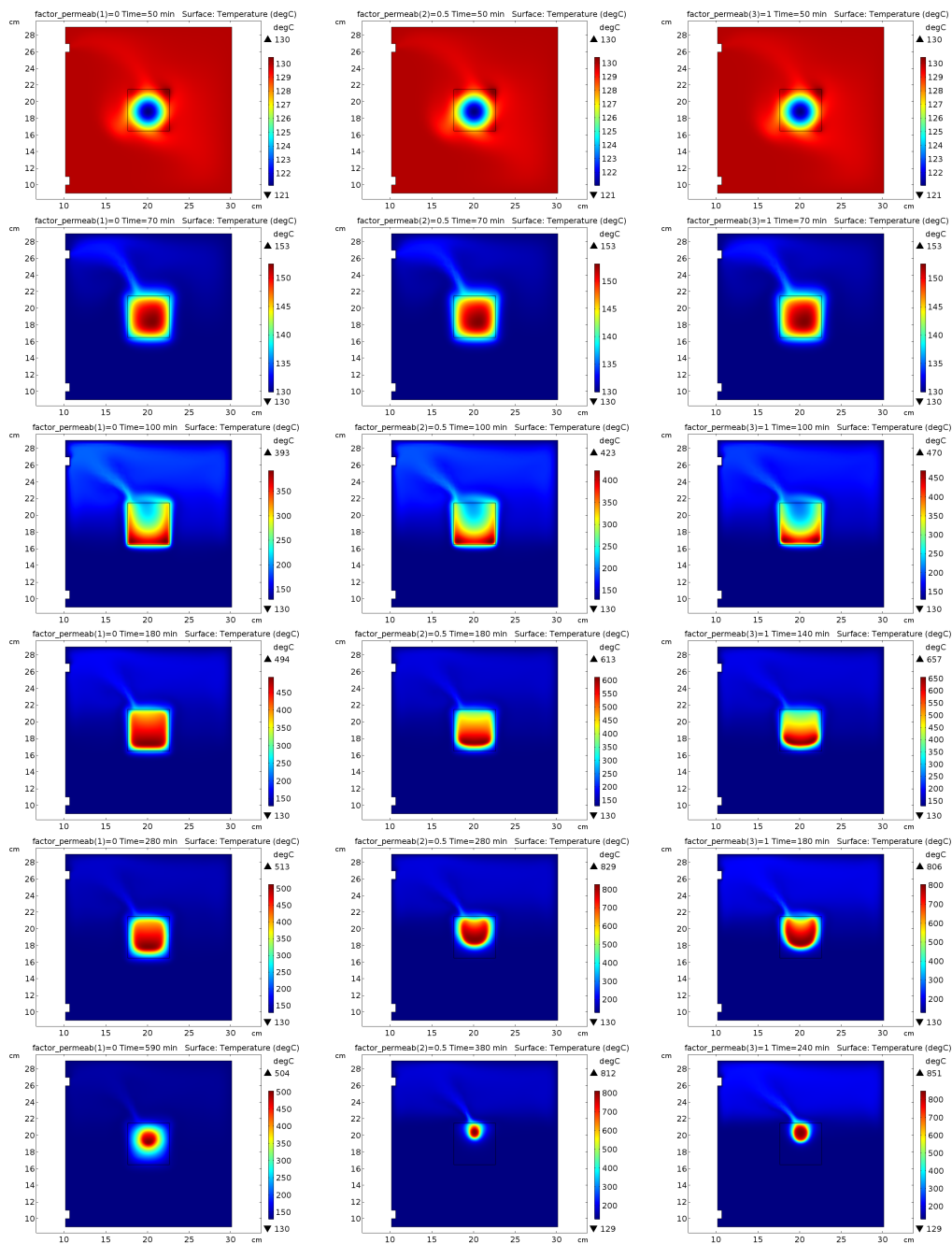


Figure A.3.: Temperature profiles for no (left column), 50 % (center column) and 100 % (right column) permeability adaption according to equation 6.8 with no reaction adjustment. Attention: different color codes (see bar at the left) Pictures per row at different time steps. Link back to page 85.

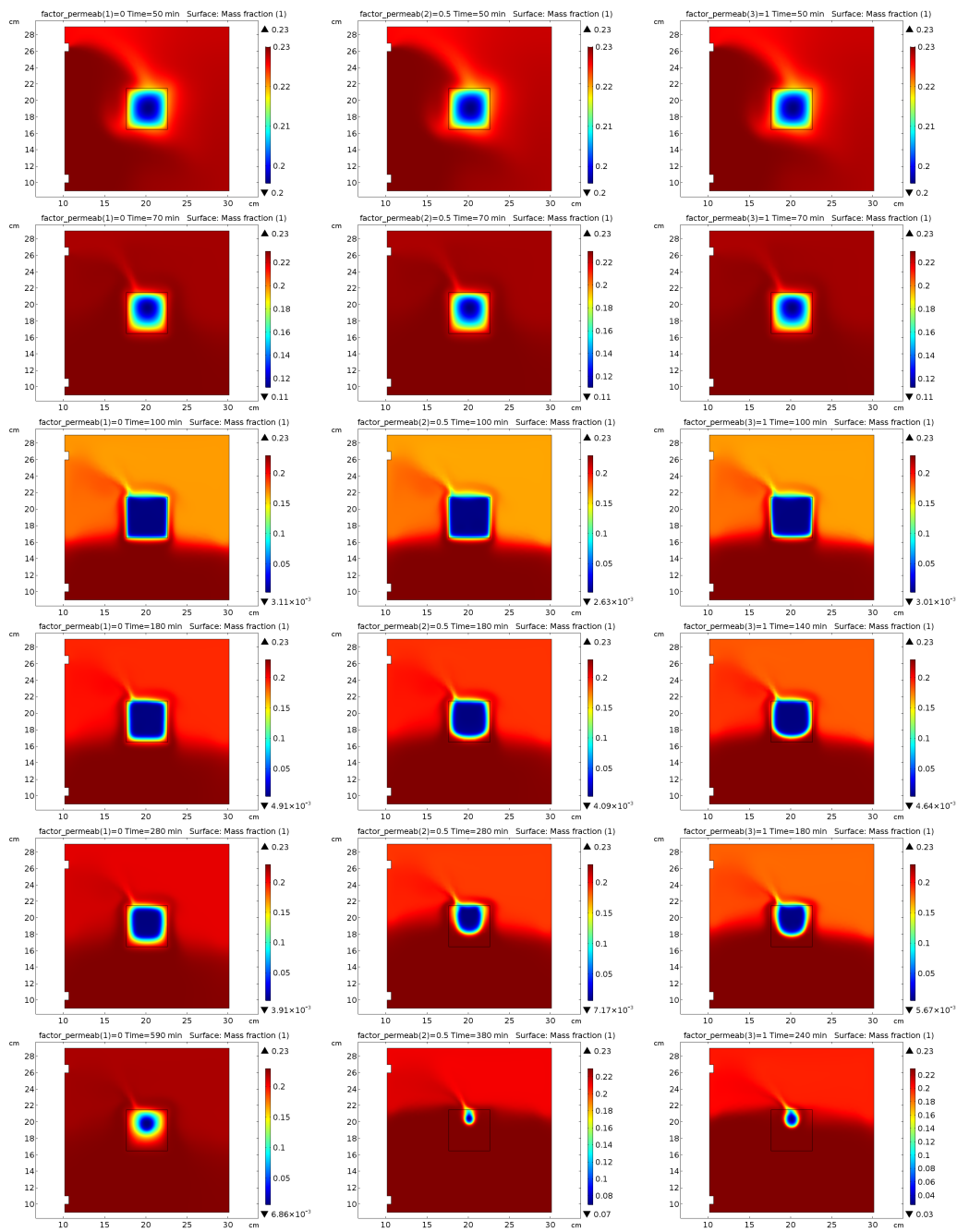


Figure A.4.: Oxygen profiles for no (left column), 50 % (center column) and 100 % (right column) permeability adaption according to equation 6.8 with no reaction adjustment. Attention: different color codes (see bar at the left) Pictures per row at different time steps. Link back to page 85.

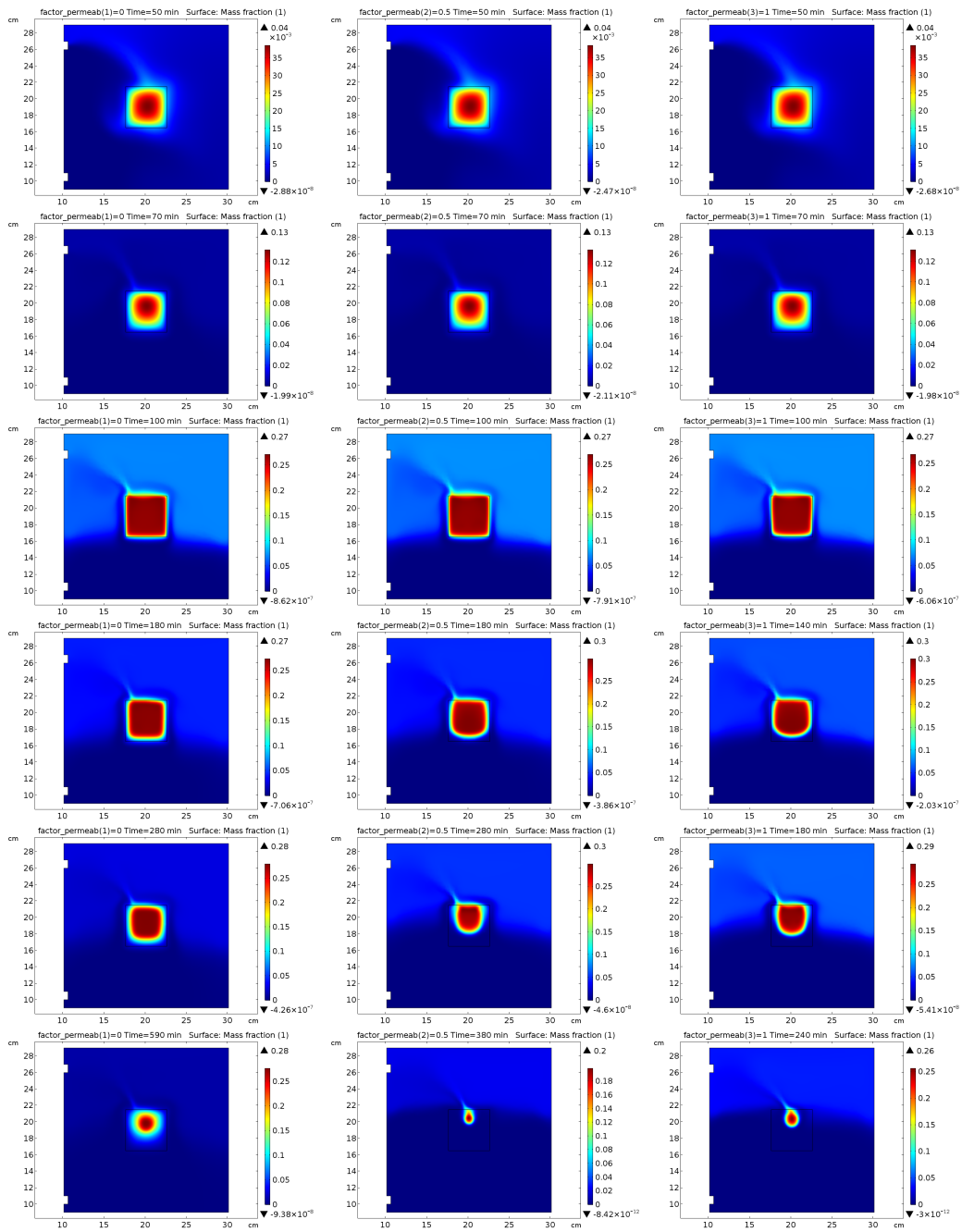


Figure A.5.: Carbon dioxide profiles for no (left column), 50 % (center column) and 100 % (right column) permeability adaption according to equation 6.8 with no reaction adjustment. Attention: different color codes (see bar at the left) Pictures per row at different time steps. Link back to page 85.

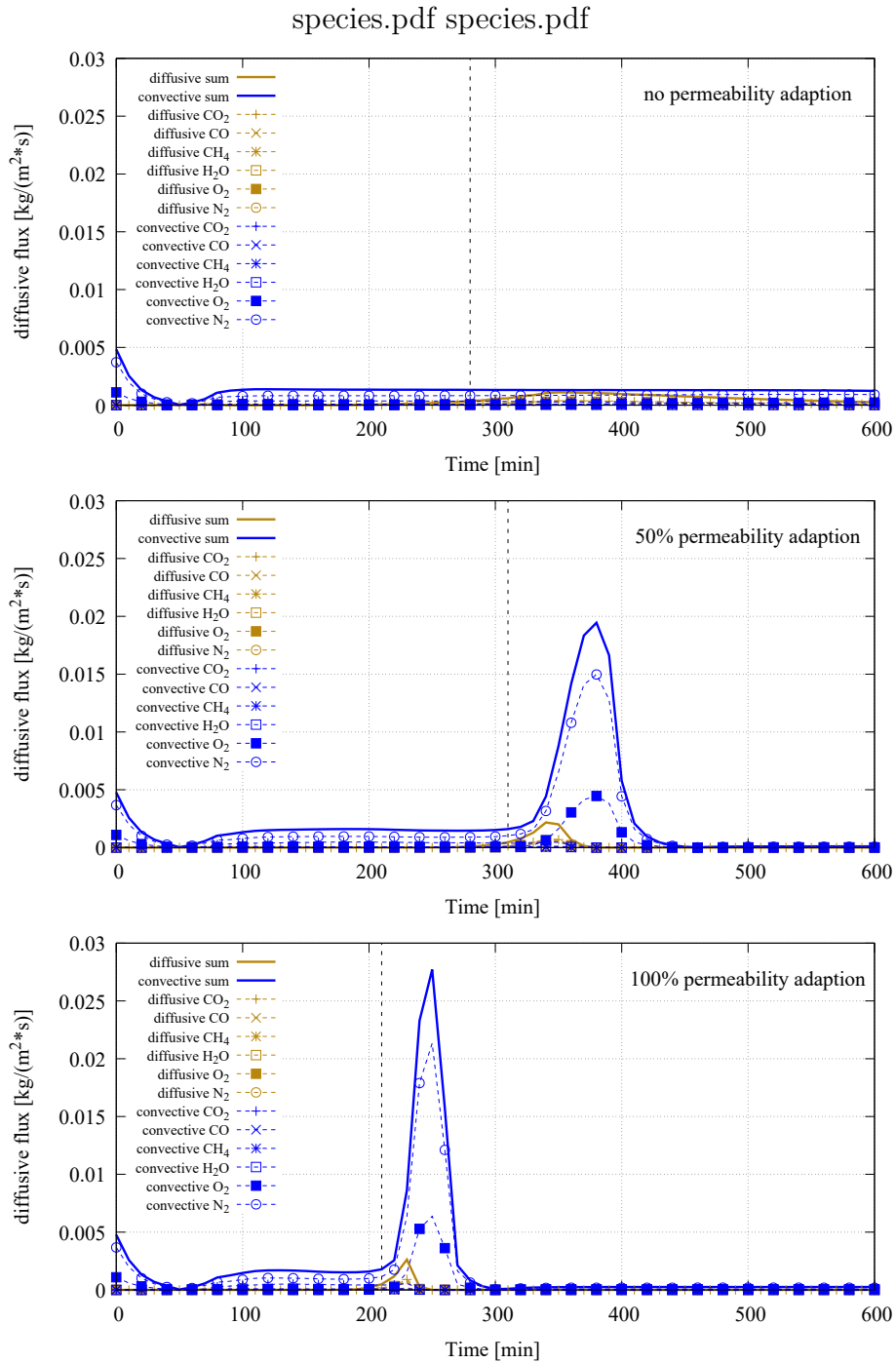


Figure A.6.: Flux of all species and summed overall flux at  $0.25 \cdot h_{sample}$  (first diagram) and  $0.5 \cdot h_{sample}$  (second and third diagram) at central axis. Reaction front passed at 280 min, 310 min and 210 min (dashed lines). Link back to page 90.

Table A.5.: Increase of the self-ignition temperature due to inert admixtures for different sample sizes [46]

Sample			$T_{SI100cm^3}$	$T_{SI200cm^3}$	$T_{SI400cm^3}$
LC-L	20 %	S063	+4	+2	-
LC-L	40 %	S063	+8	+7	+8
LC-L	20 %	S200	+5	+2	-
LC-L	40 %	S200	+10	+8	-
LC-L	20 %	S700	+6	+4	+5
LC-L	40 %	S700	+10	+9	+9
LC-P	20 %	MO130	+3	+6	+2
LC-P	40 %	MO130	+9	+10	+2
LC-P	20 %	MO150	+3	+4	+0
LC-P	40 %	MO150	+3	+10	+4

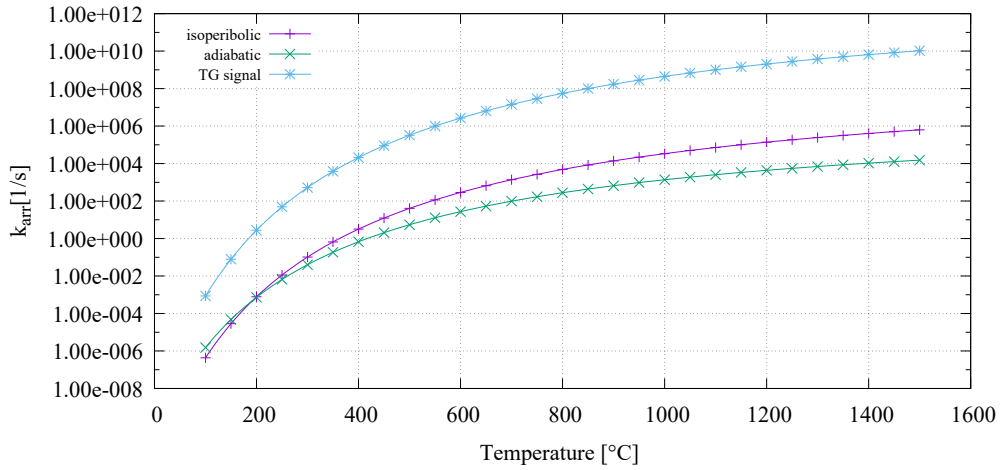


Figure A.7.: Comparison of  $k_{arr}$  for  $E_A$  and  $k_0$  determined for LC-P from experiments according to equation 6.12

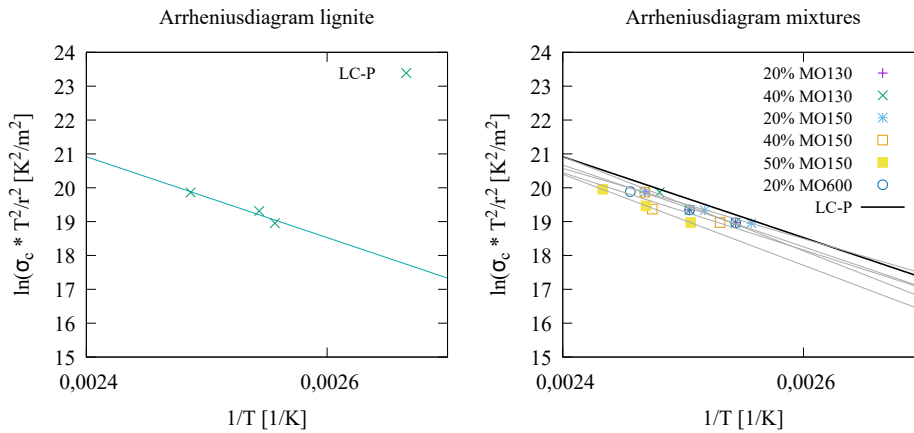


Figure A.8.: Arrhenius diagram of Lignite and Lignite Magnesium Oxide Mixtures

## B. Matlab Code for linear fitting

```
1 %% Preprocess
2 clearvars( '*' , '-except' , 'unnamed' )
3
4
5 % Variablen , nicht alle werden genutzt
6 deltaT_min=1.11; %Werte die sich vom vorgaenger nicht um
    mehr unterscheiden werden geloescht
7 glmw_anteil=0.01; %bei 0 keine Glaetung
8 glmw2_anteil=0.01; %bei 0 keine Glaetung
9 laenge_min_anteil=0.07; %lanege der anzufittenen geraden
    min
10 laenge_max_anteil=0.07; %lanege der anzufittenen geraden
    max
11 rsquare_anteil=0.999; %mindestwert fuer r_square in %
    des maximalwertes
12
13
14
15 T_kehr_min=-3.0;
16 T_kehr_max=-2.2;
17
18 %ggf matlabpool oeffnen
19 %alle worker oeffnen , zahl entsprechend der zur
    Verfuegung stehenden
20 %Rechenkerne anpassen
21 % if (matlabpool('size'))==0
22 % matlabpool open 8
23 % end
24
25
```



```
26
27 %Variablen einlesen
28 %exeltabelle per Hand einlesen und unnamed nennen; 1.
    spalte muss zeit und 2 spalte muss Temperatur
    enthalten
29 t=unnamed(:,1)%.*3600;% evtl in Sekunden umrechnen ".*60"
    einfuegen
30 T=unnamed(:,3);
31 T_O1=unnamed(:,2);
32 T_O2=unnamed(:,4);
33 T_O=mean([T_O1,T_O2],2);
34
35
36 %Experimenteller Teil um adiabaten teil automatisch zu
    finden
37 % % %adiabaten Teil fiinden
38 %
39 % %%1. ab T_max nicht mehr interessant
40 % erase=find(T==max(T));
41 %
42 % T(erase:end) = [];
43 % t(erase:end) = [];
44 % T_O(erase:end) = [];
45 %
46 % T_diff=T-T_O;
47 % loesch1=T_diff<-2;
48 % loesch2=T_diff>2;
49 % loesch=not(loesch1).*not(loesch2);
50 %
51 % erase=max(find(loesch==0));
52 % T(erase:end) = [];
53 % t(erase:end) = [];
54 % T_O(erase:end) = [];
55 %
56 % erase=min(find(loesch==0));
57 % T(1:erase) = [];
```

```
58 % t(1:erase) = [];
59 % T_O(1:erase) = [];
60 %
61 T_adiabat=T;
62 t_adiabat=t;
63
64
65 % T1=untitled(:,2);
66 % T2=untitled(:,3);
67 % %T3=untitled(:,4);
68 % T=[T1,T2];
69 % T=mean(T,2);
70
71
72 % loeschen deltaT<xxx K je zeitschritt
73 % loeschendT=find(diff(T)<deltaT_min);
74 % loeschendT(1) = [];
75 % loeschendT(end) = [];
76 % t(loeschendT) = [];
77 % T(loeschendT) = [];
78
79
80 %Parameter berechnen / imaginaere zahlen loeschen
81 lndTdt=log(diff(T_adiabat)./diff(t_adiabat));
82 Tkehr=-1000./(T_adiabat+273.15);
83 loeschen=find(imag(lndTdt)~=0);
84 lndTdt(loeschen) = [];
85
86 Tkehr(loeschen) = [];
87
88 loeschen=find(isinf(lndTdt)==1);
89 lndTdt(loeschen) = [];
90 Tkehr(loeschen) = [];
91
92 Tkehr(1) = [];
93
```

```
94 original_lndTdt=lndTdt;
95 original_Tkehr=Tkehr;
96
97 % golay_dTdt=sgolayfilt(original_lndTdt,3,41);
98 % golay_Tkehr=sgolayfilt(original_Tkehr,3,41);
99
100
101 %Glaettung ueber Gleitenden Mittelwert
102 glmw=(round((glmw_anteil*length(Tkehr))/1))*1;
103 glmw2=(round((glmw2_anteil*length(Tkehr))/1))*1;
104
105 for n=1:length(lndTdt)-glmw
106     glatt_lndTdt(n) = mean(lndTdt(n:n+glmw));
107     glatt_Tkehr(n) = mean(Tkehr(n:n+glmw));
108 end
109
110 for n=1:length(glatt_lndTdt)-glmw2
111     glatt_lndTdt2(n) = mean(glatt_lndTdt(n:n+glmw2));
112     glatt_Tkehr2(n) = mean(glatt_Tkehr(n:n+glmw2));
113 end
114
115 glatt_lndTdt=glatt_lndTdt2;
116 glatt_Tkehr=glatt_Tkehr2;
117 lndTdt=glatt_lndTdt';
118 Tkehr=glatt_Tkehr';
119
120
121 %Werte innerhalb der oben definierten Grenzen loeschen
122 % untere Grenze
123 loeschen3=find(Tkehr<T_kehr_min);
124 lndTdt(loeschen3) = [];
125 Tkehr(loeschen3) = [];
126 %
127 %obere Grenze
128 loeschen4=find(Tkehr>T_kehr_max);
129 lndTdt(loeschen4) = [];
```

```
130 Tkehr(loeschen4) = [];  
131  
132  
133  
134  
135 %aufstellen der Matritzen  
136 anstiege=zeros(length(Tkehr),length(Tkehr));  
137 rsquare=zeros(length(Tkehr),length(Tkehr));  
138  
139 %größe des min / max ausschnittes  
140 laenge_min=(round((laenge_min_anteil*length(Tkehr))/10))  
    *10;  
141 laenge_max=round(laenge_max_anteil*(length(Tkehr))/10)  
    *10;  
142 plot(Tkehr,lndTdt);  
143  
144  
145 %% Process  
146 close all  
147 %berechnen des ansteiges und von R_square im jeweiligen  
    punkt der jeweiligen  
148 %laenge  
149 tic  
150 %Schleife anfangswert  
151 for i = 1:length(lndTdt)-laenge_max  
152  
153     %Schleife endwert  
154     for j = i+laenge_min:1:i+laenge_max  
155         %zu fittender teil  
156         fit_Tkehr=Tkehr(i:j);  
157         fit_lndTdt=lndTdt(i:j);  
158         %gerade ranfitten  
159         [parameter, godness]=fit(fit_Tkehr, fit_lndTdt, '  
            poly1');  
160         %anstiegswerte/rsquare aus rueckgabe parameter  
161         anstiege_run=coeffvalues(parameter);
```

```
162         rsquare_run=godness(1).rsquare;
163         %in Array eintragen
164         anstiege(i,j)=anstiege_run(1);
165         rsquare(i,j)=rsquare_run;
166     end
167     i/(length(lndTdt)-laenge_max)
168 end
169 toc
170
171
172 %% Postprocess
173 laenge_anstiege=133; %anstiege der geraden mit genau
        dieser laenge, wir nocht verwendet experimentell
174
175 close all
176 %nach bestimmten R_square filtern
177 ungenau=rsquare>=(max(max(rsquare.*rsquare_anteil)));
178 anstiege_filter=anstiege.*ungenau;
179 %maximalen anstieg ausgabe
180 anstieg_max=max(max(anstiege_filter));
181
182 % position des max ansteiges berechnen
183 [x,y]=find(anstiege_filter==anstieg_max);
184 %R_square zu max anstieg ausgeben
185 rsquare_anzeige=rsquare(x,y);
186 %kurvenstueck bestimmen
187 fit_Tkehr=Tkehr(x:y);
188 fit_lndTdt=lndTdt(x:y);
189 %temperaturbereich bestimmen
190 temprange=(-1000./fit_Tkehr)-273.15;
191 %tupellaenge
192 tupellaenge=y-x;
193
194
195 %anstiege mit bestimmter tupellaenge ausgeben
196 anstiege_laenge_ges=diag(anstiege,laenge_anstiege);
```

```
197
198
199 [parameter , godness]= fit ( fit_Tkehr , fit_lndTdt , 'poly1' );
200 parameter_gerade=coeffvalues ( parameter );
201
202 gerade_x=fit_Tkehr ;
203 gerade_y=parameter_gerade ( 1 ) .* gerade_x+parameter_gerade
    ( 2 );
204
205 [parameter , godness]= fit ( fit_Tkehr , fit_lndTdt , 'poly1' );
206 parameter_gerade=coeffvalues ( parameter );
207 n=parameter_gerade ( 2 );
208 ausgabe=[anstieg_max , rsquare_anzeige , min ( temprange ) , max (
    temprange ) , tupellaenge , n]
209 %plotten
210 figure ( 1 )
211 plot ( Tkehr , lndTdt , fit_Tkehr , fit_lndTdt , '-r' )
212 Tkehr_laenge=Tkehr ( 1 : ( length ( Tkehr ) - laenge_anstiege ) );
213
214 % figure ( 2 )
215 % plot ( Tkehr_laenge , anstiege_laenge_ges )
```

## C. Matlab Code for Monte Carlo Simulation

```
1 clear all
2 close all
3
4 for run=1:10000
5     %Einlesen der Messwerte —> Sample Size ; TSE
6     hot_storage_measurement
           =[100,200,800,1600,3423,6400,13184,25780;123,117,105,101,95,91,85,83
7     %Variation
8     hot_storage_random1=-0.1+0.2.*rand(1,8); %Sample Size +-
           10%
9     hot_storage_random2=-2+4.*rand(1,8); %Temperature +-2 K
10
11 %Anwenden der Zufallszahlen
12 hot_storage(1,:)=hot_storage_measurement(1,:)+
           hot_storage_measurement(1,:).*hot_storage_random1;
13 hot_storage(2,:)=hot_storage_measurement(2,:)+
           hot_storage_random2;
14
15 %Berechnen der Variablen zum Fitten
16 Tkehr=1./(hot_storage(2,:)+273)';
17 radius=(hot_storage(1,:)/3.14).^^(1/3)/100;
18 ln_term=log(2.76.*(hot_storage(2,:)+273).^2./radius.^2)
           ';
19
20 %fitten
21 [parameter, godness]=fit(Tkehr, ln_term, 'poly1');
22 parameter=coeffvalues(parameter);
```

```
23 E(run)=parameter(1);
24 n(run)=parameter(2);
25 run/10000
26 end
27
28 E=E.*8.314.*-1;
29
30 %%
31 % Distribution:      Normal
32 % Log likelihood:   -95263.6
33 % Domain:           -Inf < y < Inf
34 % Mean:             109944
35 % Variance:         1.1017e+07
36
37 % Distribution:      Normal
38 % Log likelihood:   -14846.2
39 % Domain:           -Inf < y < Inf
40 % Mean:             53.3001
41 % Variance:         1.1405
42
43 E_mean=109944;
44 E_stabw=1.1e7^0.5;
45 n_mean=53.3001;
46 n_stabw=1.1405^0.5;
47
48
49 %%
50
51 Q_mass=1320; %J/g
52 M=163.8;
53 rho=710;
54 R=8.314;
55 lambda=0.082;
56 MC_run=100000;
57
58 %MC Simulation
```



```
59 %Variation der Zufallswerte von bis
60 lower_bound = -0.20;
61 upper_bound = 0.20;
62 random = lower_bound + (upper_bound - lower_bound) .* rand(5,
    MC_run);
63
64 %random = ones(5, MC_run);
65
66 dist_lam = lambda + random(4, :) .* lambda;
67 dist_rho = rho + random(3, :) .* rho;
68 dist_M = M + random(1, :) .* M;
69 Q = Q_mass * dist_M;
70
71 %E und n sind normalverteilt nach oben ausgerechneter
    normalverteilung
72 E_normal = E_mean + E_stabw .* randn(1, MC_run);
73 n_normal = n_mean + n_stabw * randn(1, MC_run);
74
75 % A berechnen
76 A = exp(n_normal) .* R .* dist_lam ./ E_normal ./ Q ./ dist_rho;
77
78 %min max ausgeben
79 min_max_A = [min(A), max(A)]
```